DIGITAL ACCESS TO SCHOLARSHIP AT HARVARD
DASH.HARVARD.EDU

HARVARD LIBRARY

Simulating Protoplanetary Disk Dynamics and Investigating Their Exoplanet Outcomes

Citation

Price, Ellen Marie. 2021. Simulating Protoplanetary Disk Dynamics and Investigating Their Exoplanet Outcomes. Doctoral dissertation, Harvard University Graduate School of Arts and Sciences.

Link

https://nrs.harvard.edu/URN-3:HUL.INSTREPOS:37368361

Terms of use

This article was downloaded from Harvard University's DASH repository, and is made available under the terms and conditions applicable to Other Posted Material (LAA), as set forth at
https://harvardwiki.atlassian.net/wiki/external/NGY5NDE4ZjgzNTc5NDQzMGIzZWZhMGFlOWI2M2EwYTg

Accessibility

https://accessibility.huit.harvard.edu/digital-accessibility-policy

Share Your Story

The Harvard community has made this article openly available.
Please share how this access benefits you. Submit a story

HARVARD UNIVERSITY
Graduate School of Arts and Sciences

DISSERTATION ACCEPTANCE CERTIFICATE

The undersigned, appointed by the

Department of Astronomy

have examined a dissertation entitled

Simulating Protoplanetary Disk Dynamics and Investigating their Exoplanet Outcomes

presented by

Ellen M. Price

candidate for the degree of Doctor of Philosophy, and hereby

certify that it is worthy of acceptance.

Signature _____ _____

Typed name: Prof. Dimitar Sasselov. Chair

Signature _____

Typed name: Prof. Karin Öberg, Advisor

Signature _____

Typed name: Dr. Sean Andrews

Signature _____

Typed name: Prof. Ralph Pudritz

Signature _____

Typed name: Dr. David Wilner.

Date: May 3, 2021

Simulating Protoplanetary Disk Dynamics and Investigating Their Exoplanet Outcomes

A dissertation presented

by

Ellen M. Price

to

The Department of Astronomy

in partial fulfillment of the requirements

for the degree of

Doctor of Philosophy

in the subject of

Astronomy & Astrophysics

Harvard University

Cambridge, Massachusetts

May 2021

© 2021 Ellen M. Price
All rights reserved.

Simulating Protoplanetary Disk Dynamics and Investigating Their Exoplanet Outcomes

Abstract

Protoplanetary disks are the formation sites of planets and represent an exciting challenge for any theorist. We have undertaken two studies of protoplanetary disks and two studies of unusual exoplanets to better understand extrasolar planetary systems.

First, we examine the effects of accretion on protoplanetary disk chemical evolution. In many chemical models, the physical conditions of a gas parcel are fixed throughout the simulation. Instead, we develop a simple surface density model to compute the evolution of the disk's surface and volume densities as functions of space and time. This information can be fed into a chemical model, simulating the change in local conditions as the gas parcel accretes towards its central star. We find that cosmic rays play a particularly interesting role in the chemical evolution, since cosmic-ray driven chemistry in the outer disk can then drive different chemistry in the inner disk, compared to a parcel that maintains a fixed location.

Next, we move to a different aspect of disk evolution: grain drift. Small grains in a protoplanetary disk are well-entrained with the gas, but larger ones tend to drift inward towards the central star. Unlike the previous model, in which any accretion track is independent of all others, a model that includes drift allows "communication" between intersecting gas and solid trajectories. This effect makes the model more computationally expensive to run, so we limit the model to two chemical species, CO and H_2O, in two phases, ice and gas. We find that a region of enhanced CO/H_2O is easily and robustly formed in our model disk, which may help explain observations of CO-enhanced comets like 2I/Borisov and C/2016 R2 (PanSTARRS).

Finally, we address extrasolar planets in extreme environments, with a particular focus on KOI 1843.03. The so-called ultra-short period (USP) planets are planets on particularly close-in orbits, and their formation mechanism is a matter of ongoing research. We seek to better understand USP

planets by modeling their interiors self-consistently, which allows us to place constraints on their probable iron content and core mass fraction if they are near or at the Roche limit. For KOI 1843.03, we are even able to favor a core comprised of pure Fe over one comprised of pure FeS. Ongoing work involves determining the shapes of transit light curves for non-spherical, tidally-distorted USP planets.

Contents

Title page i

Copyright ii

Abstract iii

Contents v

Front matter vii
- Acknowledgements . . . vii
- Dedication . . . ix
- List of Figures . . . x
- List of Tables . . . xii

1 Introduction 1
- 1.1 Protoplanetary disks . . . 1
- 1.2 Planet formation . . . 5
- 1.3 Planets and their variety . . . 7
- 1.4 Numerical methods for planetary science . . . 10
- 1.5 Goals of this dissertation . . . 16

2 Chemistry Along Accretion Streams in a Viscously-Evolving Protoplanetary Disk 17
- 2.1 Abstract . . . 17
- 2.2 Introduction . . . 18
- 2.3 Methods . . . 21
- 2.4 Results . . . 30
- 2.5 Discussion . . . 36
- 2.6 Conclusions . . . 43

3 Ice-Coated Pebble Drift as a Possible Explanation for Peculiar Cometary CO/H_2O Ratios 48
- 3.1 Abstract . . . 48
- 3.2 Introduction . . . 49
- 3.3 Methods . . . 51

3.4 Results . . . 57
3.5 Discussion . . . 64
3.6 Conclusions . . . 66
3.7 Supplementary equations . . . 67

4 Tidally-Distorted, Iron-Enhanced Exoplanets Closely Orbiting Their Stars 69
4.1 Abstract . . . 69
4.2 Introduction . . . 70
4.3 Methods . . . 71
4.4 Results . . . 80
4.5 Discussion . . . 87

5 Transit Shapes of Tidally-Distorted Rocky Exoplanets 93
5.1 Introduction . . . 93
5.2 Methods . . . 94
5.3 Results . . . 96
5.4 Discussion . . . 98

6 Concluding Remarks and Outlook 100
6.1 Grain growth and evolution . . . 101
6.2 Microchemical simulations . . . 101

Bibliography 104

I have not been able to enter my office without prior clearance for over a year now. I no longer see my friends and colleagues every day, and I chose not to visit my family for the holidays to avoid spreading COVID-19 to them. Finishing a dissertation during this time has seemed, to me, anticlimactic, in the sense that there will be no large, in-person celebration at its conclusion, and more challenging, since I have been working from home continuously for the past year. Even though the past year has been trying, I would not have made it here at all without support from friends, family, and mentors who made it possible.

To my family, thank you for encouraging and supporting me, both emotionally and financially, until I was able to support myself. From sending me to the best high school in the area to paying Caltech tuition, you have always wanted what was best for me and would give me the best chance at a promising future. I particularly thank my immediate family, Manual and Janice Price and Catherine Smith, for their tireless encouragement since the beginning of this process.

To my friends, thank you for letting me invade your offices, share my problems, and generally annoy you on an almost-daily basis. In particular, I want to recognize graduate or former graduate colleagues Theron Carmichael, Jamila Pegues, Roxana Pop, Jane Huang, Munazza Alam, and Locke Patton, who have been especially supportive during my graduate school career. I also want to recognize a few Caltech alums who have been great friends to me throughout the years: Nick "Copernicus" Parker, Max De Jong, Jacob Shenker, Cedric Flamant, Charles Tschirhart, Kelly Mauser, Juliette Becker, and Ben Yuan.

To my mentors, thank you for writing letters, meeting during and after work hours, and patiently explaining concept after concept to me until I finally understood. My high school teachers Tommy Abney, Nick Gerontakis, and Debbie Anderson, who fueled my passion for science; my work study mentors Christina Richey, Perry Gerakines, and David Hilton, who supervised my first endeavors into research; my college research advisors John Johnson and Leslie Rogers, who gave me a love for planetary science; my graduate school administrators, Robb Scholten and Peg Herlihy, who magically arranged extended time off for me when I was ill; and my graduate school supervisors and committee members Karin Öberg, Ilse Cleeves, and Sean Andrews, who pushed me to do my best

work and supported me to this final culmination of my work, all have a special place in my heart for helping me reach this point.

> Whatever you do, do it enthusiastically, as something done for the Lord and not for men, knowing that you will receive the reward of an inheritance from the Lord. You serve the Lord Christ.
>
> — Colossians 3:23–24, HCSB

To God be the glory.

To my friend, Rhiannon Johnson, who passed long before her time.

List of Figures

1.1 Tour of a protoplanetary disk. 2

2.1 Outline of an iterative method for determining disk temperature. 22
2.2 Various time-evolving fields in the accreting disk model. 25
2.3 Total disk mass and accretion rate for the accreting disk model. 27
2.4 Change in physical variables along accretion tracks in the accreting disk model. 28
2.5 Comparison of accreting and non-accreting disk models. 31
2.6 Carbon and nitrogen in organics as a function of time in the accreting disk model. . . . 44
2.7 Comparison of fiducial disk model to models without cosmic rays. 45
2.8 Time-dependent behavior of several chemical species in the accreting disk model. 46
2.9 Evolution of accreting disk model with higher cosmic ray ionization rate. 47

3.1 Temperature scaling fraction computed from stellar isochrons. 57
3.2 Temporal and spatial evolution of model disk temperature. 58
3.3 Temporal and spatial evolution of three bulk surface densities for the grain drift disk. . . 59
3.4 Fiducial model evolution of surface densities in the grain drift disk. 60
3.5 Evolution of CO/H_2O ice ratio in the grain drift disks. 65

4.1 Coordinate system and geometry of the simulation space for tidally-distorted planets. . . 73
4.2 Piecewise equations of state for planet interiors. 79
4.3 Contours of constant cmf as a function of transit radius and minimum orbital period for planets with pure Fe cores. 81
4.4 Composition and mass constraints on analogs of KOI 1843.03. 82
4.5 Aspect ratio constraints on KOI 1843.03. 83
4.6 Minimum orbital period as a function of transit radius and composition for planets with FeS cores. 84
4.7 Planet mass as a function of core mass fraction and orbital period for K2 137b. 85

4.8 Aspect ratio constraints on K2 137b. 85
4.9 Histograms of cmf and aspect ratio for K2 229b. 86
4.10 Histograms of cmf and aspect ratio for K2 106b. 86

5.1 Geometry of the raytracing problem for non-spherical planets. 97
5.2 Preliminary raytraced transits for non-spherical planets. 98

List of Tables

2.1 Fiducial accreting disk model parameters. 24
2.2 Fiducial accreting disk model temperature parameters. 26
2.3 Initial chemical abundances in the accreting disk model. 30
2.4 Abundances of enhanced and abundant species in the accreting disk model. 34
2.5 Comparison of our accreting disk model to Heinzeller model. 40

3.1 Explored model cases and parameter values for grain drift disks. 60
3.2 Model outcomes for grain drift disks. 64

4.1 Orbital velocities and fluxes for possibly-distorted planets in the *Kepler* sample. 88

Chapter 1

Introduction

1.1 Protoplanetary disks

Protoplanetary disks are the systems of gas and dust that surround a young star, and they are the birthplaces of planets. Because the characteristic timescales of planet formation are very long compared to a human lifetime, observing planet formation in real time is unrealistic. Instead, we observe statistical samples of disks that serve as "snapshots" of planet formation to piece together a complete picture of the process. The exact mechanism by which planets form is still a topic of ongoing theoretical research: While we know that planets frequently do form, we do not yet understand how they overcome the many obstacles to their formation, and this is discussed further below.

One reason we might want to study planet formation in other planetary systems is to learn indirectly about our own: Is our Solar System an anomaly, or are systems like this commonplace in our galaxy? How often do planets which may support life occur? However, we can also learn more about the Solar System by sampling comets, which can tell us something about the composition of the protosolar disk. With the appearances of the first observed interstellar comets, 1I/'Oumuamua and 2I/Borisov, we may one day be able to sample from comets from other planetary systems, learning even more about their early compositions.

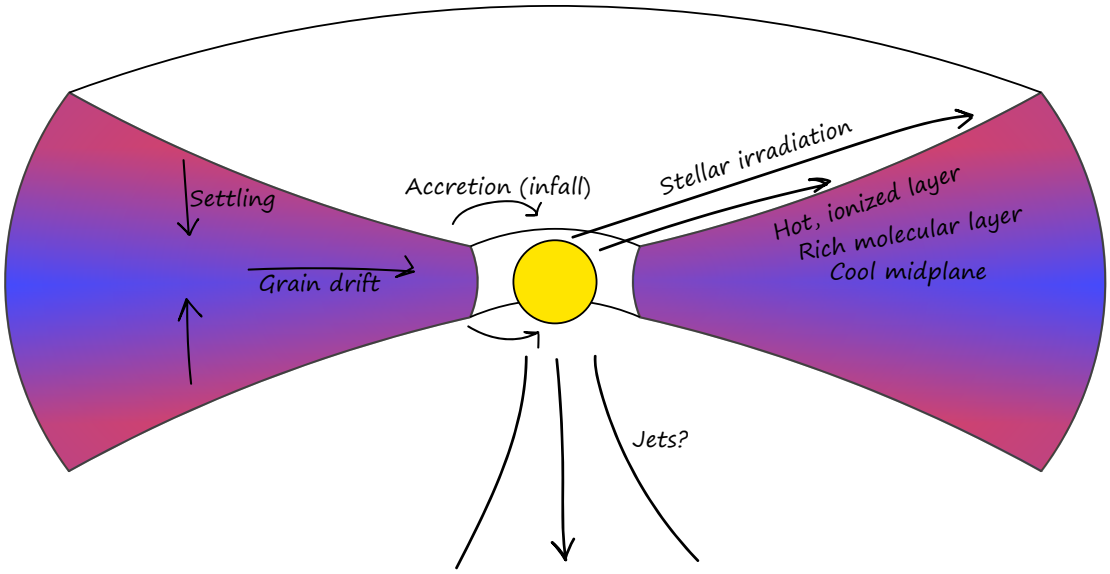

Figure 1.1: A major focus of this dissertation is protoplanetary disks, the birthplaces of planets. Here, we show a few major features of disks, including the temperature gradient (red to blue colors).

Protoplanetary disks assume a disk shape as a direct consequence of the conservation of angular momentum of collapsing parent cloud. Within this broad criterion, there is still room for variation, however, as described below. Figure 1.1 points out some important features of protoplanetary disks graphically.

Radial structure

Broadly, we radially separate a protoplanetary disk into an "outer" region and an "inner" region, though the exact location of the border between these regions is more a matter of personal preference than a strict rule; in this dissertation, the inner disk will refer to the region within about 10 au of the central star. One must keep in mind when discussing the inner and outer regions that material is free to move between the two via accretion (as an example), which is the topic of Chapter 2.

A significant temperature gradient arises between the inner disk and the outer disk due to the mechanism by which disk material is heated. Stellar irradiation can heat the material closest to the

star directly, but Chiang & Goldreich (1997) suggest that the inner material is heated by radiation that impinges on the disk atmosphere and is re-radiated, and they show how such a model compares with SED (spectral energy distribution) observations of disks. Their models have a radial temperature gradient because, as one moves to larger disk radii, the disk becomes vertically thicker, and so the re-radiated radiation needs to penetrate deeper into the disk to reach the midplane. From radiative transfer, we know that, as radiation passes through more material with nonzero absorption and/or scattering opacities, the intensity falls off exponentially.

The Chiang & Goldreich (1997) flat disk model is a vertically isothermal disk with a temperature that falls as a power law in radius; for that geometry, in which the disk's opening angle is not dependent on distance from the star R, they conclude that $T \propto R^{-3/4}$. The flat geometry may not be entirely realistic — they address a disk in hydrostatic and radiative equilibria as well — but the power law behavior remains; for those more complex models, $T \propto R^{-1/2}$, and this is a common starting point for disk temperature models.

In addition to the radial temperature gradient, the disk also has a radial density gradient: The mass density generally falls off with distance from the central star, but the exact form of the density is model-dependent. One well-known model for the surface density $\Sigma \equiv \int \rho \, \mathrm{d}z$, due to Lynden-Bell & Pringle (1974), is the so-called "self-similar" model, which applies when the temperature falls as a power law in radius. Clarke & Carswell (2007) give an explicit solution for the δ-function initial condition (an infinitely thin "pulse" of surface density) centered at R_0 based on the Lynden-Bell & Pringle (1974) derivation,

$$\Sigma(x, \tau) \propto \frac{1}{\tau x^{1/4}} \exp\left[-\frac{1+x^2}{\tau}\right] I_{1/4}\left(\frac{2x}{\tau}\right), \tag{1.1}$$

where $x = R/R_0$ is a dimensionless distance, τ is a dimensionless time, and $I_{1/4}$ is a modified Bessel function. Since any function can be decomposed into an infinite number of such pulses, the fundamental solution can be used to find the surface density at a given radius and time for an arbitrary initial surface density.

Analytic solutions for the vertically-integrated density structure of the disk are very useful, but they only apply to specific temperature and viscosity functions. The solution above implicitly

assumes that the inner boundary of the disk is $R = 0$, which implies an infinitely small, point-source star, though this assumption can be relaxed (see Tanaka 2011). Finally, by only considering the surface density, we wash out information about the vertical disk structure, discussed in the next section.

Vertical structure

In the vertical direction, we consider layers of material based on the level of irradiation, which sets the composition. The disk midplane is coolest and densest, and chemical species are frequently frozen out, or *adsorbed*, onto grain surfaces. Next highest above the midplane is a warm, molecular layer, where a rich chemistry can be found, driven by higher temperatures and X-ray and UV radiation (Rab et al., 2016). Finally, the topmost layer is hot and ionized because it receives unattenuated or only slightly attenuated stellar and interstellar radiation; this is the "superheated" layer of Chiang & Goldreich (1997).

Though these layers are chemically distinct due to the physical conditions driving the chemistry in each, they are also not completely independent. Vertical turbulent mixing can move material between layers; so, for example, dust grains can be lofted into the molecular layer where molecules can efficiently photo-desorb from the grain surfaces due to higher temperatures there (Rab et al., 2016).

Vertically, protoplanetary disks have a temperature and density gradient, just as in the radial direction. For some fixed distance R from the central star, the temperature increases towards the disk atmosphere, since that material is more directly heated by the star. In addition to the Chiang & Goldreich (1997) model, which has just two temperature "layers," D'Alessio et al. (1998) propose a continuous model for the disk's vertical temperature structure as a system of differential equations with two boundaries. Dartois et al. (2003) suggest a simple, analytic function for the vertical temperature with a few parameters that can be used as an alternative, which could speed up computation of the density structure, discussed next.

The vertical density structure is set by hydrostatic equilibrium, where the gas pressure gradient

is exactly balanced by the gravitational force from the star. If the disk is vertically isothermal, then the vertical density takes the form of a Gaussian. However, the disk is *not* vertically isothermal, and thus the equations for the vertical temperature and density can be solved together as a system to find a self-consistent solution (e.g., Andrews et al., 2012).

Chemical composition

The temperature and density gradients along with spatially-varying radiation field determine what chemical species are abundant in each disk region. For example, where the ionizing radiation field is weak, neutral-neutral reactions occur (Henning & Semenov, 2013). Where the disk is relatively cold, ions and molecules will freeze onto grain surfaces, where surface reactions can take place (Henning & Semenov, 2013). At low densities, surface chemistry reactions tend to produce hydrogenated species, like H_2O, because hydrogen is so mobile on grain surfaces (van Dishoeck & Blake, 1998). A full enumeration of reactions which can occur in disks is unrealistic because of the sheer number of reactions which may occur efficiently in at least one region of the disk.

For simulation purposes, we tabulate these reactions and classify them by the way their rate coefficient is computed. The rate coefficient encodes the rate at which the reaction proceeds and is typically a function of temperature. A common form of the rate k is the modified Arrhenius equation,

$$k(T) \propto \alpha T^{\beta} e^{-\gamma/T} \tag{1.2}$$

where α, β, and γ are constants that can be measured in the lab. To obtain the rate of change of the concentration of a species in a chemical model, k is multiplied by the concentrations of all the reactants. This is demonstrated below.

1.2 Planet formation

In a protoplanetary disk, smaller dust particles are caught up with the gas motion and follow the gas trajectories closely, while larger particles begin to deviate and drift inwards; as the particles

grow larger still, drift becomes negligible and the particles follow Keplerian orbits (Weidenschilling, 1977). Since the motion of the particles is size-dependent, we can expect that dust and pebbles — that is, small solid particles — can have nonzero relative velocities and may collide. Collisions may result in bouncing, fragmentation, or coagulation, and the exact outcome of the collision will certainly depend on the sizes of the particles involved and relative velocity. Furthermore, particles tend to settle towards the midplane, so collisions are more likely to occur there than in the upper layers of the disk (Johansen et al., 2014). There are significant barriers to dust growth through this mechanism, however. The "bouncing barrier" refers to the fact that particles greater than about a decimeter in size are more likely to bounce in a collision than to aggregate (Morbidelli & Raymond, 2016). Another barrier is the "meter-size barrier" or "drift barrier" (Morbidelli & Raymond, 2016), which alludes to how particles with a Stokes number around unity drift most rapidly (e.g., Birnstiel et al., 2010) and may drift into the star faster than they can grow to larger sizes. Brauer et al. (2008) finds that, even when more realistic and self-consistent physics is included in their planet formation model, these barriers remain significantly problematic. Once particles do become large enough — however that may happen — gravitational forces far outweigh aerodynamic forces, and accretion of small particles onto large ones occurs rapidly.

Many solutions to these barriers have been proposed in the literature, however, and so it seems likely that they can be overcome in typical disk environments. For example, magnetorotational turbulence can concentrate boulders in a small region and increase their radial drift times, and so gravoturbulence may play some role in mitigating the drift barrier mentioned above and lead to the formation of planets (Johansen et al., 2006). This is a particularly exciting development because turbulence becomes a solution rather than a problem for planet formation. Furthermore, Bai & Stone (2010) find that, by considering a more realistic radial drift velocity in the disk midplane, local enhancements of solids can greatly reduce the drift velocity, enhancing planet formation. For micrometer dust, a proposed resolution to the bouncing problem is that particles coated with ice are "stickier" than particles without an ice coating (Gundlach & Blum, 2015), which may decrease the probability of bouncing at that size.

Though the exact process by which planets form is still a topic of debate, we do have some observational evidence for planet formation in action. The protoplanetary disk PDS 70, for example, is observed to have two protoplanets embedded in it and actively accreting disk material (e.g., Wagner et al., 2018). This kind of direct observation is not always feasible, but we also have secondary indicators of possible planet formation. For example, gaps in a protoplanetary disk may be carved by an embedded giant planet; similarly, spiral waves in the disk may indicate a low-mass planet (Andrews, 2020). Unfortunately, as Andrews (2020) mentions, the indirect evidence for planet formation is more ambiguous than direct observations, because the spiral arms that could indicate low-mass planets could also indicate magnetic field concentrations and MHD winds.

1.3 Planets and their variety

One way to partition the discovered exoplanets is into "rocky" and "non-rocky" groups, but this separation does not capture the immense variety of exoplanets and exoplanetary systems.

One planet of particular interest to this dissertation is KOI 1843.03, an exoplanet candidate in the *Kepler* sample. It is a particularly fascinating planet because of its short orbital period (4.2 hr) and theorized high iron content based on the mean density inferred from transit light curve measurements (Rappaport et al., 2013). In Chapter 4, we examine this planet in far more detail and attempt to constrain its core composition. Because its iron content is similar to that of Mercury in our own Solar System, KOI 1843.03 is sometimes called an "exo-Mercury" planet, but it is important to recall that Mercury has a much longer orbital period and therefore is not in such extreme conditions as this exoplanet.

On the other side of the density spectrum, some planets, dubbed "super-puffs," have strangely low densities and masses, implying a much larger radius for a fixed mass than one would typically expect. Kepler 51b is just one of these unusual planets. Wang & Dai (2019) suggest that one explanation for such low inferred densities and flat transmission spectra is that small dust grains have been lofted into the upper atmosphere of the planet, artificially inflating the transit radius and decreasing

the measured density. Piro & Vissapragada (2020) instead suggest that some super-puff planets may be explained by rings. While this may not be the case for Kepler 51b — it depends on the material of the rings — the authors find that Kepler 87c and 177c are the most likely super-puffs to have rings.

Between these extreme cases, we have found candidate and confirmed exoplanets with properties that span the limits on many axes and push the boundaries of what we thought was possible for planets and planetary systems.

Planet interior structures

Wood et al. (2006) gives a detailed review of the process by which Earth's core differentiated from its mantle, but the exact mechanism is less important to this dissertation than the end result: Earth is differentiated into an iron-rich core and silicate-rich mantle. Differentiation is not limited to planet-sized bodies, though, because Thomas et al. (2005) argues that the asteroid Ceres is also differentiated. The significance of the composition of a differentiated planet is explored in Chapter 4, but, in essence, the sizes and compositions of the core and mantle of a two-layer planet change the gravitational field of the planet, which has important implications for its equilibrium shape.

When characterizing an exoplanet, one may wonder why the interior structure is of any scientific interest. A key question in this field regards the habitability, or potential for life, on exoplanets. Many believe that the presence of liquid water is key for life, as it is on Earth. We might reasonably say that distance from the star is important for determining whether water attains its liquid form on the surface of an exoplanet, but distance from the central star alone is not enough to make that determination. The atmosphere — or lack thereof — of an exoplanet can play a significant role in determining the surface temperature, since greenhouse gases trap heat inside the atmosphere. Noack et al. (2014) explore the effects of planet interior structure on CO_2 outgassing and find that the habitability of a planet may depend strongly on the structure and whether plate tectonics are active; furthermore, planets with larger cores typically release much less CO_2 through outgassing.

Ultra-short period planets

A particularly exciting class of planets is the ultra-short period planets class, of which KOI 1843.03, discussed above, is an example. Ultra-short period (USP) planets are extrasolar planets with orbital periods less than one day, meaning the length of one year for a USP planet could be just a handful of hours. These planets are near or at their Roche limit — the distance from the star where tidal forces begin to rip the planet apart. USP planets are relatively rare and are estimated to form around about 0.5% of G dwarf stars (Sanchis-Ojeda et al., 2014). The mechanism of this formation remains a mystery, though some recent theories include those by Lee & Chiang (2017), Petrovich et al. (2019), and Millholland & Spalding (2020).

Petrovich et al. (2019) suggest that USP planets are not so different from hot Jupiter planets in their formation: Perhaps they began with orbits of approximately 5 – 10 days and move inward via high-eccentricity migration. They propose that USP planets are typically the innermost planet in a multi-planet system and that those companions excite the eccentricity of the innermost planet through secular chaos. Then, tides raised on the surface of the planet by the central star damps the eccentricity until the orbit attains a much lower eccentricity, now as a USP planet. Lee & Chiang (2017), on the other hand, argue against such a theory, on the basis that secular interactions with companions smaller than Jupiter cannot compete with general-relativistic precession. Instead, they support a theory based on migration from the inner edge of the protoplanetary disk inwards to USP orbits. Finally, Millholland & Spalding (2020) propose yet another theory of formation, wherein a planet on a close-in orbit can experience runaway semimajor axis decay that stops when the obliquity reaches high values. In short, there is no one accepted theory of USP planet formation, but the protoplanetary disk structure and composition ultimately determines how planets migrate and from what material they form.

1.4 Numerical methods for planetary science

This dissertation takes a largely numerical approach to understanding phenomena like protoplanetary disk evolution and planet compositions. Throughout the sciences, physical systems are frequently described by ordinary and partial differential equations. From the propagation of waves to the complex interactions of fluids, there is frequently an ordinary (ODE) or partial (PDE) differential equation that describes the evolution of the system in time and/or space. One of the best-known set of PDEs is the Navier-Stokes equations for fluid flow, which reduce to the Euler equations in the limit of no viscosity. The gas phase of protoplanetary disk material, like any other fluid, should be described by these equations, so they form an important basis for simulations of disk evolution.

How to solve an ODE

Typically, an ODE is expressed as a system of equations in one independent variable, such as time; the most general form of an ODE is

$$\frac{\mathrm{d}\boldsymbol{y}}{\mathrm{d}t} = f(\boldsymbol{y})\,, \tag{1.3}$$

where $\boldsymbol{y}$ is a vector of unknown functions and t is the independent variable. These equations encode, for example, how a planet moves along its trajectory with time or how the concentration of a chemical species changes in a well-mixed reaction.

There are many methods to solve ODEs, but they broadly fall into two categories, *implicit* and *explicit* solvers. To explain this difference, we consider a simple *linear* ODE

$$\frac{\mathrm{d}\boldsymbol{y}}{\mathrm{d}t} = \mathbb{A}\boldsymbol{y} \tag{1.4}$$

where $\mathbb{A}$ is some linear operator, which, in this case, does not depend on $\boldsymbol{y}$ or time t. This equation can be solved exactly using the operator exponential, but we are interested in its numerical solution, which requires discretization, yielding

$$\frac{\boldsymbol{y}^{n+1} - \boldsymbol{y}^{n}}{\Delta t} = \mathbb{A}\boldsymbol{y}, \tag{1.5}$$

where $\boldsymbol{y}^n = \boldsymbol{y}(t^n)$ is the solution at time t^n and Δt is a small timestep. This equation would be fully determined if not for the $\boldsymbol{y}$ that appears on the right-hand side: Should we choose $\boldsymbol{y}^n$, $\boldsymbol{y}^{n+1}$, or some combination of the two?

The explicit Euler solver chooses $\boldsymbol{y}^n$ for the right-hand side, and so, upon rearrangement of terms, we find

$$\boldsymbol{y}^{n+1} = (\mathbb{I} + \Delta t \mathbb{A})\, \boldsymbol{y}^n, \tag{1.6}$$

where $\mathbb{I}$ is the identity operator. Equation 1.6 completely determines each solution as a function of only the previous step's solution. While this is a simple approach and very easy to implement, it is not practical to use if the operator $\mathbb{A}$ is *stiff*.

Stiffness is a property frequently observed in simulations of chemical reactions, such as those involved in protoplanetary disk evolution. Formally, stiffness is encoded in the eigenvalues of $\mathbb{A}$, but, informally, it occurs when the timescales of processes in the simulation are separated by orders of magnitude. In a chemical reaction network, this is very common: Some reactions are, for fixed conditions, inherently faster than others. The explicit Euler solver above would perform very poorly for a stiff choice of $\mathbb{A}$, requiring inconveniently small timesteps Δt to capture the dynamics without instability.

The implicit Euler solver makes the other obvious choice for the discretization in Equation 1.5 and puts $\boldsymbol{y}^{n+1}$ on the right-hand side. After rearranging the equation again, we find

$$(\mathbb{I} - \Delta t \mathbb{A})\, \boldsymbol{y}^{n+1} = \boldsymbol{y}^n. \tag{1.7}$$

Since $\mathbb{A}$ is a linear operator in this example, a linear equation of the form $\mathbb{A}\boldsymbol{x} = \boldsymbol{b}$ must be solved at each timestep to get to the next solution. In exchange for the increased effort involved, however, implicit Euler can generally use larger timesteps than explicit Euler without instability. Implicit Euler can also be applied to stiff equations.

These are the two simplest integration schemes for ODEs, and yet neither are sufficient to capture disk chemistry in a reasonable computation time. First, the methods above are only first-order accurate, meaning that the error that accumulates on each step is of order Δt: Increasing

the timestep will naturally increase the expected error. Much more sophisticated methods for time integration exist, however, which are of higher order and may take larger timesteps. For explicit integration, the class of Runge-Kutta methods exists, including the popular RK4 integration scheme. For implicit integration, BDF (backwards differentiation formula) is of high order and accuracy, and it is very appropriate for stiff equations.

Concretely, consider a simple chemical reaction involving species A, B, and C that proceeds at rate k

$$A + B \xrightarrow{k} C. \tag{1.8}$$

If we want to encode this reaction into set of ODEs for the concentrations of the species, then we would write

$$\frac{\mathrm{d}\left[A\right]}{\mathrm{d}t} = \frac{\mathrm{d}\left[B\right]}{\mathrm{d}t} = -k\left[A\right]\left[B\right] \tag{1.9}$$

$$\frac{\mathrm{d}\left[C\right]}{\mathrm{d}t} = k\left[A\right]\left[B\right]. \tag{1.10}$$

However, we note that this equation is actually nonlinear because of the product $[A]\,[B]$, so we require a more sophisticated approach than the above method to solve this system of ODEs: Instead of solving a linear equation at each timestep, we would solve a nonlinear equation. If k is time-dependent or depends in some way on $[A]$, $[B]$, and/or $[C]$, then the equation is still nonlinear, but it may become even harder to solve.

How to solve a PDE

PDEs are generally harder to solve than ODEs because of their higher dimensionality. Whereas the unknown function in an ODE depends only on one independent variable, such as time, the PDEs we find in physics tend to have unknowns which depend on time and space; the equations of radiative transfer, for example, depend on time, space, frequency, and angle. PDEs that describe physical systems often have two kinds of spatial operators: advection and diffusion. Both are needed in a protoplanetary disk simulation.

Advection describes how some field moves along with a background "wind." The first of the Navier-Stokes equations is a good example of an advection equation,

$$\frac{\partial \rho}{\partial t} + \nabla \cdot (\rho \boldsymbol{u}) = 0, \tag{1.11}$$

where ρ is a density field and $\boldsymbol{u}$ is the velocity of the fluid. This equation encodes the conservation of mass in the absence of sources or sinks. Diffusion, on the other hand, is exemplified by the heat equation, such as

$$\frac{\partial u}{\partial t} = \nabla^2 u \tag{1.12}$$

where u is some field of interest that diffuses in time. The process of diffusion tends to make the field "spread out" over time.

There are many methods to solve PDEs such as these: finite elements, finite volume, and discontinuous Galerkin are just a few. For fluids in particular, there are additional specialized methods, such as smoothed particle hydrodynamics. Each method is suited to a particular class of equation. In the work that follows, the method used is, by comparison, much simpler than any of these. One of the simplest methods available to solve a PDE is finite differences, where the spatial derivatives are reduced to linear operators. For example, suppose we want to solve the heat equation on a one-dimensional grid with constant spacing Δx. The derivative is approximated, to second order, by

$$\frac{\partial^2 u}{\partial x^2} \approx \frac{1}{\Delta x^2} \left(u_{i-1} - 2u_i + u_{i+1} \right), \tag{1.13}$$

where u_i is the value of the function u at grid point i. This equation can be conveniently expressed as a tridiagonal linear operator, like

$$\mathbb{A} = \frac{1}{\Delta x^2} \begin{pmatrix} -2 & 1 & 0 & 0 \\ 1 & -2 & 1 & 0 \\ 0 & 1 & -2 & 1 \\ 0 & 0 & 1 & -2 \end{pmatrix} \tag{1.14}$$

in the case where we sample at four grid points.

At this point, we must address boundary conditions. ODEs need an initial condition to fully specify their evolution; PDEs need an initial condition *and* some number of boundary conditions

to be well-posed. The matrix $\mathbb{A}$ above is appropriate when $\boldsymbol{u}$ has homogeneous Dirichlet boundary conditions: We imagine a virtual grid point on either side of the domain, extending the domain in each direction. For a Dirichlet boundary condition, we specify the value of the function at these grid points. The case when the value is zero is particularly easy to handle, as shown above. More care must be taken to address nonzero Dirichlet conditions or Neumann conditions, where the value of the derivative is specified at one side of the domain.

Another important caveat is that advection problems frequently require *upwind* derivatives to remain numerically stable. This requires us to know in what direction the background velocity field is oriented at a given location and time. These derivatives are only used when appropriate to the equation, and they are only first-order accurate.

Disk modeling theory

In a perfect world, we could use the three-dimensional Navier-Stokes equations (for the disk gas evolution), the equations of radiative transfer (for heating of dust grains), the equations of aerodynamics (for dust grain motion), a description of coagulation and fragmentation (such as the Smoluchowski equations, for dust growth), and a full chemical network with rates dependent on, for example, temperature, density, and irradiation, to completely describe the evolution of every element of a protoplanetary disk.

Consider how many resources a simulation like that would take. The Navier-Stokes equations are given as five variables in three spatial dimensions. Radiative transfer is particularly intensive to compute, since specific intensity is given as a single field in two angular, three spatial, and one frequency dimension, making it a total of six-dimensional. The Smoluchowski equation describes how a series of dust sizes evolve through collisions, so the number of variables scales as the number of dust size "bins" when the equation is discretized. The chemical network alone would be challenging to address, since the number of variables scales as the number of chemical species, which might be hundreds or thousands. The independent variable "grid" for a set of coupled equations in six dependent variables would be of size $\mathcal{O}(N^6)$ assuming a constant number of discrete grid points

N in each of six dimensions. Let us assume that there are P chemical species and Q dust sizes; in a two-phase model, where a chemical species exists either in the gas or solid phase, this gives us $2PQ$ independent variables, so let us assume that the independent variable vector is of size $\mathcal{O}(PQ)$. Each of these variables needs to be stored on the grid, but, since specific intensity is the only variable that depends on frequency or angle, we can write our estimate of size as $\mathcal{O}(N^3PQ + N^6)$. Suppose now that $N = P = Q = 10^2$; this is almost certainly insufficient, but this number is simply for demonstration purposes. A single vector of unknowns for these evolution equations is then of order 10^{12} in size.

If we want to store this vector on a computer, assuming we work in double-precision floating point, each variable occupies 8 bytes of memory. Thus, storing a *single time snapshot* of the simulation described would require 8 terabytes. To put that in context, Wolfram|Alpha[1] estimates that this is almost half the text content of the Library of Congress. In addition to storing that amount of information as a vector, we would also require an operator describing how a snapshot evolves to the next timestep; if this operator is linear, it is approximately 8000 zettabytes in size. Wolfram|Alpha estimates that the information content of all global data is only about one zettabyte.

Clearly, the naïve approach described above will *not* work. The art of protoplanetary disk modeling involves finding approximations that reduce the dimensionality of the problem to a reasonable size. For example, we might choose to express our problem in cylindrical coordinates because the disk is natively cylindrical in shape. In that coordinate system, we might assume that no variable depends on the azimuthal angle, reducing the spatial dimension to two. If we furthermore assume a simple vertical structure and integrate our equations over the vertical dimension, we have reduced the spatial dimension to one. For the radiation field, which requires the most independent variables, we might make an approximation that it is completely determined by its first two *moments*, as in the M1 approximation. Then, we need not consider the two angular dimensions of the problem at all, reducing the total dimensionality down to one spatial and one frequency variable — a significant improvement! These approximations do not come without tradeoffs, however. Azimuthal symmetry,

[1] `https://www.wolframalpha.com`

for example, precludes the possibility of azimuthal asymmetries like spirals that have been observed by projects such as DSHARP (the Disk Substructures at High Angular Resolution Project) (Huang et al., 2018).

1.5 Goals of this dissertation

The following chapters take a closer look at protoplanetary disk evolution and some of the extreme exoplanets formed in other planetary systems. In Chapter 2, I consider the process of accretion in greater detail, showing how it plays a strong role in influencing disk chemistry. Chapter 3 continues examining the dynamics of disk solids and how they change the CO/H_2O ratio as a function of space and time. Chapter 4 shifts to considering extreme USP planets like KOI 1843.03 and how they may be deformed into non-spherical shapes. Finally, Chapter 5 takes the first steps toward answering the question of whether non-spherical USP planets could be detected by current instruments.

Chapter 2

Chemistry Along Accretion Streams in a Viscously-Evolving Protoplanetary Disk

This chapter originally appeared in the literature as:

Price, E. M., Cleeves, L. I., & Öberg, K. I. 2020, ApJ, 890, 154, doi: 10.3847/1538-4357/ab5fd4

©AAS. Reproduced with permission.

2.1 Abstract

The composition of a protoplanetary disk is set by a combination of interstellar inheritance and gas and grain surface chemical reactions within the disk. The survival of inherited molecules, as well as the disk *in situ* chemistry depends on the local temperature, density and irradiation environment, which can change over time due to stellar and disk evolution, as well as transport in the disk. We address one aspect of this coupling between the physical and chemical evolution in disks by following accretion streamlines of gas and small grains in the disk midplane, while simultaneously taking the evolving star into account. This approach is computationally efficient and enables us to take into account changing physical conditions without reducing the chemical network. We find that many species are enhanced in the inner disk midplane in the dynamic model due to inward trans-

port of cosmic-ray driven chemical products, resulting in, e.g., orders-of magnitude hydrocarbon enhancements at 1 au, compared to a static disk. For several other chemical families, there is no difference between the static and dynamic models, indicative of a robust chemical reset, while yet others show differences between static and dynamic models that depend on complex interactions between physics and chemistry during the inward track. The importance of coupling dynamics and chemistry when modeling the chemical evolution of protoplanetary disks is thus depends on what chemistry is of interest.

2.2 Introduction

Planets form in the dust- and gas-rich disks around young stars, i.e., in protoplanetary disks. The chemical composition of the disk directly impacts the compositions of forming planets and planetesimals. Rocky planets, ice giants, and comets all assemble mainly from disk solids, and their composition depends on the refractory and volatile content of dust grains. By contrast, gas giants obtain much of their mass directly from the disk gas, and their composition therefore depends on both the disk's gas and dust chemical compositions (e.g., Mizuno, 1980; Bodenheimer & Pollack, 1986; Öberg et al., 2011; Kokubo & Ida, 2012; Cridland et al., 2016, 2017b).

The chemistry of the disk spatially varies due to gradients in radiation fields, temperature and density structures, and cosmic ray attenuation. These effects act to produce a radially-changing disk molecular composition (e.g., Aikawa et al., 1997; Willacy & Langer, 2000; Bergin et al., 2007). Moreover, at the relevant pressures and densities, much of the disk does not reach local steady state within the few million year lifetime of the gas disk (e.g., Aikawa et al., 1998). Chemical processing of the material can thus have a significant effect on the planetesimals' compositions (Eistrup et al., 2016). Accurately predicting the time-evolving chemical history of a disk and comparing with observations of disk gas are therefore key to understanding what compositions planets can potentially acquire.

Observations of molecules in disks are limited (McGuire, 2018) due to their low masses, rela-

tively cool temperatures, and small angular extents. The inner disk ($R \lesssim 10$ au) is observed to have gas-phase molecules like H_2O, CO, nitrogen-bearing species, and hydrocarbons. *Spitzer* observations of the upper disk layers in the inner disk suggest a partial "reset-like" chemistry (Pontoppidan et al., 2014) due to the extreme densities, temperatures, and radiation fields close to the star. As shown in this study, this chemistry is expected to be modified by continuous inward transport of molecules formed in the outer parts of the disk, resulting in deviations from steady-state chemistry.

The outer disk ($R \gtrsim 10$ au), on the other hand, is characterized by sequential freeze-out of abundant volatiles (Henning & Semenov, 2013) and a slower chemical conversion that may preserve more of the disk's initial composition, as set by the molecular cloud. In this region, the relative importance of inheritance and *in situ* chemical processing depends on the vertical location within the disk. For H_2O ice in the midplane, models demonstrate that the outer disk likely exhibits an "inheritance-like" chemistry, where the timescales for chemical evolution can be longer than the disk lifetime, thus processing little of the ice (Semenov & Wiebe, 2011; Cleeves et al., 2014b). For cyanide species, observations are more consistent with chemical reprocessing (Öberg et al., 2015).

These different results can, in part, be explained by strong vertical gradients in physical conditions in the outer disk. The uppermost, surface layer experiences strong irradiation, so relatively fast photochemistry dominates. Beneath the surface layer is a warm molecular layer where ion–molecule chemistry chemistry dominates; CO is present but H_2O is frozen out onto grains. Finally, close to the midplane, molecules freeze out onto grains and slow grain surface reactions dominate the chemistry (Henning & Semenov, 2013).

Modeling disk chemistry is complicated by the fact that disks and their host stars are dynamic — densities, temperatures and radiation fields all evolve with time. Theory and observations show that protoplanetary disks are actively accreting (e.g., Lynden-Bell & Pringle, 1974; Gullbring et al., 1998), with some material transferred onto the star and some material moved outward, conserving angular momentum. Other dynamical processes that may be relevant include vertical mixing, turbulence, and grain drift and settling (Whipple, 1973; Weidenschilling, 1977; Morfill, 1983; Weidenschilling & Cuzzi, 1993; Hanner, 1999; Bockelée-Morvan et al., 2002; Willacy et al., 2006; Semenov et al., 2006;

Cridland et al., 2017a; Bacciotti et al., 2018). In addition to material physically moving in the disk, the star itself introduces an added complication since it, too, is evolving in time (e.g., Siess et al., 1997), changing the incident radiation field and temperature profile of the disk.

The most common astrochemical treatment of a viscously-evolving disk is to fix the physical conditions to their local values at a given time and allow the chemistry to evolve at these fixed conditions. A handful of models have explored the coupling of some dynamical processes and chemistry. Early examples of coupling chemistry with accretion flows include Bauer et al. (1997) (and subsequent papers) and Aikawa et al. (1999). Nomura et al. (2009) followed the chemistry along simple streamlines in an α-disk model and assumed a constant accretion rate. Heinzeller et al. (2011) used the same physical model with the addition of X-ray heating and investigated the effects of radial accretion, turbulent mixing, and disk winds. Including accretion in the model caused significant changes in the chemical composition of the disk midplane. Cridland et al. (2016) and Cridland et al. (2017b) used the Chambers (2009) analytic model of viscous disk accretion to investigate the relationship between disk chemistry and planetary atmospheres, finding that the location and time at which the planet atmosphere accretes its atmosphere strongly affects its composition.

We build on these previous efforts and follow local physical conditions in accretion streams of gas and small, presumably coupled, grains in the disk midplane. We choose to focus on the midplane in this work because the gas and ice mantles on grains in the midplane eventually become available for incorporation into forming planetesimals, and because it allows some simplifying assumptions to be made regarding radiation fields and accretion stream geometries. This paper is structured as follows. In Section 2.3, we introduce the method we use to trace both chemistry and physical conditions as functions of time. In Section 2.4, we present the results of our model. We discuss and conclude our analysis in Sections 2.5 and 2.6, respectively.

2.3 Methods

Our goal is to compute the time-dependent tracks that gas follows through a vicously evolving disk around an evolving pre-main sequence star and to solve for the chemical abundances along these tracks. Note that the tracks are treated as completely independent from one another, i.e., are not mixed, greatly simplifying the computation. Additionally, we treat the dust as well-coupled to the gas and do not address dust grain evolution, which may be chemically important. The main role of the dust is to provide surface area for chemical reactions. Dust growth and fragmentation fundamentally change the surface area to volume ratio of dust, however the dynamical evolution is more complex than can be treated in the present prescription, which we will address in future work.

One of the primary challenges to overcome in this method is that the surface density evolution and temperature structure are interdependent. To solve for both self-consistently, we use an iterative procedure, outlined in Figure 2.1.

Accretion disk model

We construct the physical disk model using the α-disk framework (Shakura & Sunyaev, 1973). We work in a cylindrical coordinate system parametrized by (R, ϕ, z); here, R is the radial coordinate (distance from the star in the x-y plane), ϕ is the azimuthal angle, and z is the vertical coordinate (height above the midplane).

The viscosity of an α-disk is given by

$$\nu = \alpha c_s h = \alpha c_s^2 / \Omega_{\rm Kep} \tag{2.1}$$

where $\Omega_{\rm Kep} \equiv \sqrt{GM_\star/R^3}$ is the Keplerian angular velocity, c_s is the local sound speed, h is the local disk scale height determined by the midplane temperature, and $M_\star$ is the stellar mass; we assume that the disk mass is negligible compared to $M_\star$. α is a small dimensionless parameter with typical values 10^{-2} to 10^{-4}; this range is supported observationally by, e.g., Flaherty et al. (2018), which found $\alpha < 0.007$ for the TW Hya disk. The sound speed is given by

$$c_s^2 = \frac{k_B T}{\mu m_p}, \tag{2.2}$$

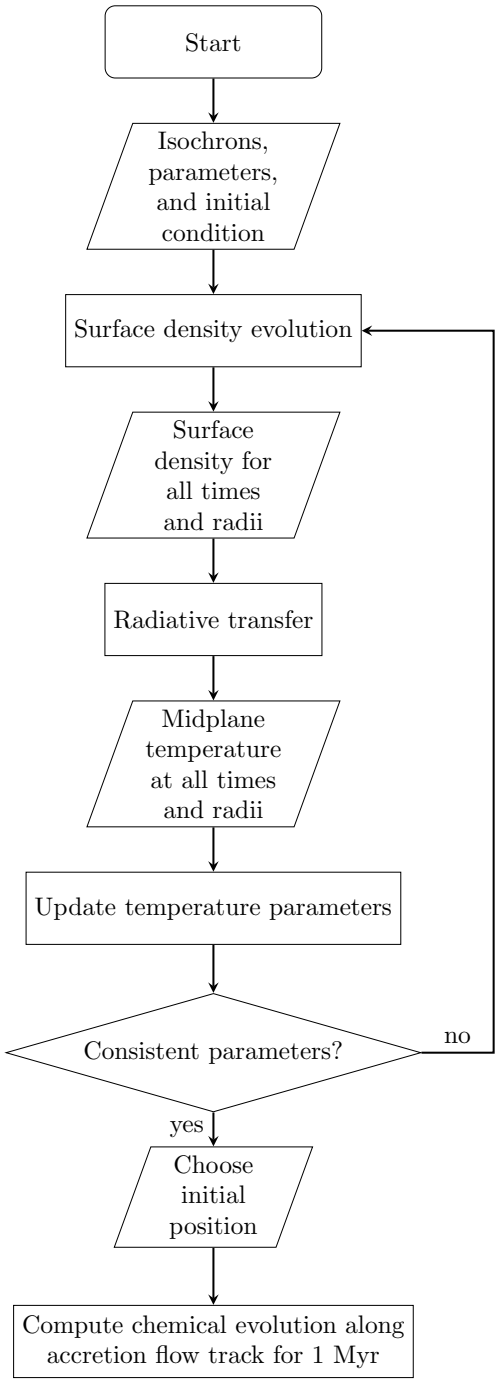

Figure 2.1: Outline of the method presented in Section 2.3. In this diagram, rectangles represent processes, trapezoids represent inputs and outputs, and diamonds represent decisions. We begin by making an initial guess of parameters T_0, ψ, ω, α_0, α_1, and β_1 (see Equation 2.8) and iterate between solving Equation 2.3 and using radiative transfer until a consistent set of parameters is found. At that point, we can choose any initial point and solve for a gas parcel's trajectory through the disk from Equation 2.10. Finally, the chemical evolution is solved in a postprocessing step.

where μ is the mean molecular weight of the gas, k_B is the Boltzmann constant, and T is the temperature of the gas and dust; we take the gas temperature equal to the dust temperature, which is reasonable in the disk midplane where the dust and gas are well-coupled through collisions (Henning & Semenov, 2013). This temperature is computed and subsequently parametrized as a function of time and radius (see Section 2.3).

We begin with the general surface density evolution equation (e.g., Pringle, 1981; Clarke & Carswell, 2007; Armitage, 2010),

$$\frac{\partial \Sigma}{\partial t} - \frac{3}{R}\frac{\partial}{\partial R}\left[R^{1/2}\frac{\partial}{\partial R}\left(\nu \Sigma R^{1/2}\right)\right] = 0. \tag{2.3}$$

This equation can be derived from the Navier-Stokes and mass continuity equations for a fluid, as shown in Clarke & Carswell (2007). Because of the flexible form of the temperature we choose (see Section 2.3), there exists no easily-found analytic solution for the surface density. Thus, we solve the equation numerically, using a simple finite difference scheme with second-order accurate spatial derivatives and a Crank-Nicoloson timestepping scheme. We implement this method using PETSc (Balay et al., 2018, 1997; Abhyankar et al., 2014).

Our initial surface density profile is informed by observations of disks, so we choose a form similar to

$$\Sigma(t = 0, R) \propto \left(\frac{R}{R_1}\right)^{-\gamma} \exp\left[-\left(\frac{R}{R_1}\right)^{2-\gamma}\right] \tag{2.4}$$

in the notation of, e.g., Andrews et al. (2012). However, for $\gamma = 1$, a reasonable value based on observational fitting, this initial condition would approach infinity as R approaches zero. This presents a computational challenge, because the value of Σ cannot simply be fixed to a value at small radii due to disk evolution, yet an infinite value at $R = 0$ is both unphysical and difficult to handle numerically. We circumvent this problem by introducing a sharp exponential taper at finite radius, given by

$$f(R) = \begin{cases} \exp\left[-\left(\frac{R-R_3}{R_4}\right)^{2\xi}\right], & R < R_3 \\ 1, & R \geq R_3 \end{cases} \tag{2.5}$$

Parameter	Symbol	Value
Stellar mass	$M_\star$	$1 M_\odot$
Viscosity parameter	α	10^{-3}
Mean molecular weight	μ	2.35
Normalization radius	R_0	1 au
Shape parameter	R_1	40 au
Σ normalization radius	R_2	10 au
Shape parameter	R_3	0.3 au
Shape parameter	R_4	0.1 au
Value of Σ at R_2	Σ_2	100 g cm^{-3}
Exponential taper exponent	ξ	4
Gas-to-dust ratio		100
Cosmic ray rate	$\zeta_{\rm CR}$	10^{-18} s^{-1}

Table 2.1: Fiducial model parameters.

with shape parameters R_3, R_4, and $\xi > 0$ that may be chosen freely. This function decays faster than Equation 2.4 blows up[1], so it is effective in producing the desired Dirichlet boundary condition[2] at small R. Because Equation 2.4 decays exponentially at large R, we do not need to introduce additional factors to produce a Dirichlet boundary condition at $R/R_1 \gg 1$. In practice, then, we multiply Equation 2.4 by Equation 2.5 and then normalize to a chosen value $\Sigma_2 = \Sigma(t = 0, R_2)$, where R_2 is a chosen normalization radius. Parameters relevant to this model are listed in Table 2.1.

Disk temperature and density structures

As mentioned previously, we must assume a temperature structure to solve for the surface density, ultimately resulting in a new temperature structure. We use the Siess et al. (2000) isochrons for a $M_\star = 1 M_\odot$, $Z = 0.02$ star to obtain the stellar radius and effective temperature on a linearly-spaced grid of given ages. We combine the dust density, assuming azimuthal symmetry, with the stellar parameters and compute the resulting dust temperature structure using RADMC-3D (Dulle-

[1] At first glance, it may appear that imposing zero surface density at finite radius inhibits accretion. However, if we examine the functional form of the accretion rate, $\dot{M} = -2\pi R \Sigma u_R$ (Pringle, 1981), we see from Equation 2.10, which gives u_R, that the factors of Σ cancel; so the accretion rate can still be finite when Σ approaches zero.

[2] A boundary condition in which the value of the unknown function is fixed to a given value at the boundaries only; in this case, the value zero is enforced.

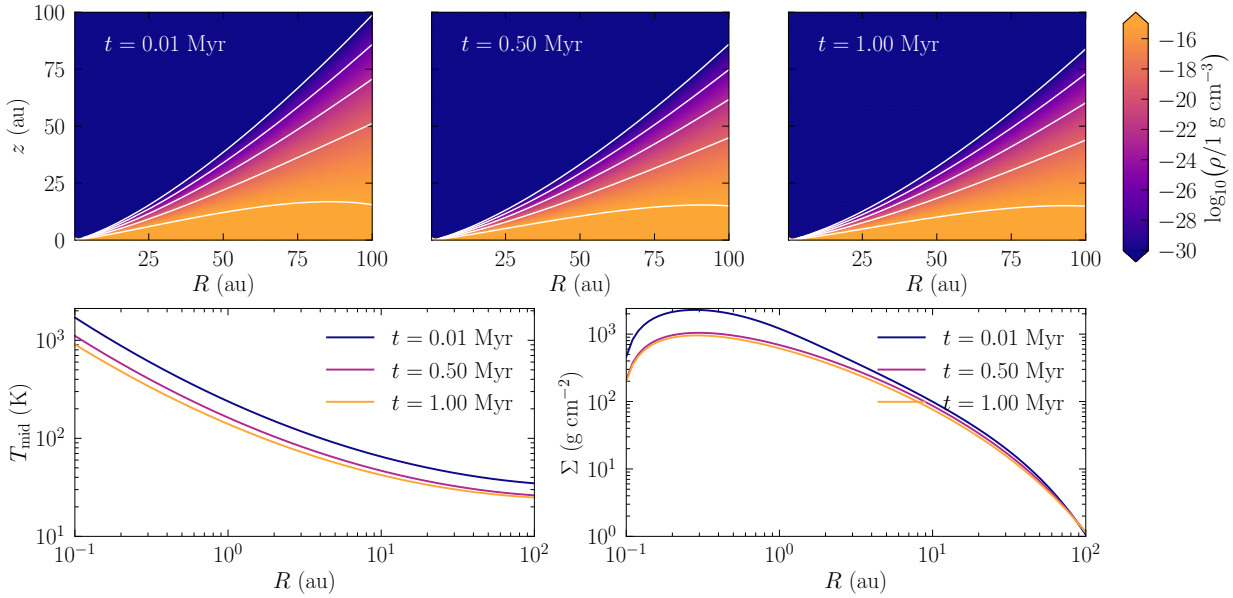

Figure 2.2: Disk density, midplane temperature, and surface density sampled at different times, computed by solving the equations in Section 2.3. The top three panels show the mass density ρ as a function of radius, s, height, z, and time. The bottom panels show the midplane temperature and surface density, both as functions of radius and time.

mond et al., 2012); at the end of the Monte Carlo simulation, the effects of accretion heating are added in flux space, so

$$T^4_{\text{final}} = T^4_{\text{RADMC}} + T^4_{\text{accretion}} \tag{2.6}$$

and

$$T^4_{\text{accretion}} = \frac{GM_\star \dot{M}}{8\pi\sigma R^3} \tag{2.7}$$

(e.g. Hartmann, 2009). We iterate this procedure, fitting each time for the unknown parameters in our temperature model until the solutions converge to a relative precision of 5%.

We assume a temperature function — which enters into Equation 2.3 through the viscosity term — that takes the flexible form

$$T(t, R) = T_0 \left(e^{-\psi t/t_0} + \omega\right) e^{\beta_0 \log x + \beta_1 \log^2 x}, \tag{2.8}$$

where $x = R/R_0$ is a dimensionless radius; $\beta_0 = \alpha_0 t/t_0 + \alpha_1$; and T_0, ψ, ω, α_0, α_1, and β_1 are parameters to be determined. We find that this large number of parameters is necessary to capture,

Symbol	Value	Symbol	Value
T_0	110 K	α_0	0.044
ψ	2.5	α_1	-0.71
ω	1.2	β_1	0.063

Table 2.2: Fiducial model temperature parameters from iterative fitting procedure.

with reasonable accuracy, the full radial- and time-dependent behavior of the disk temperature structure. The approximate final parameters we derive for this model are listed in Table 2.2. We do not use the raw temperatures from RADMC-3D because derivatives of the temperature function are needed for the time evolution of the surface density, and using the output without fitting would introduce unnecessary noise.

Once the temperature structure is known, the disk structure is fully determined at all times and radii. This information allows us to compute, for example, the disk mass and accretion rate as functions of time. These quantities are shown in Figure 2.3, from which we confirm that the accretion rate is reasonable.

We solve Equation 2.3 for a given set of temperature parameters to obtain the surface density at all radii and all times. We interpolate this function and obtain the gas density by assuming that it has a vertical Gaussian profile, i.e.

$$\rho(R, z) = \frac{\Sigma\left(R\right)}{\sqrt{2\pi}h} \exp\left(-\frac{z^2}{2h^2}\right). \tag{2.9}$$

Further we adopt a gas-to-dust mass ratio of 100 at all radii, and assume only small micron-sized grains as prescribed in Fogel et al. (2011), such that the dust grains are well-coupled to the gas motion; we do not include larger grains here.

Computing tracks

For the physical model and stellar evolution described in the previous sections, we can compute self-consistent tracks of material through the disk following the velocity field implied by the evolving

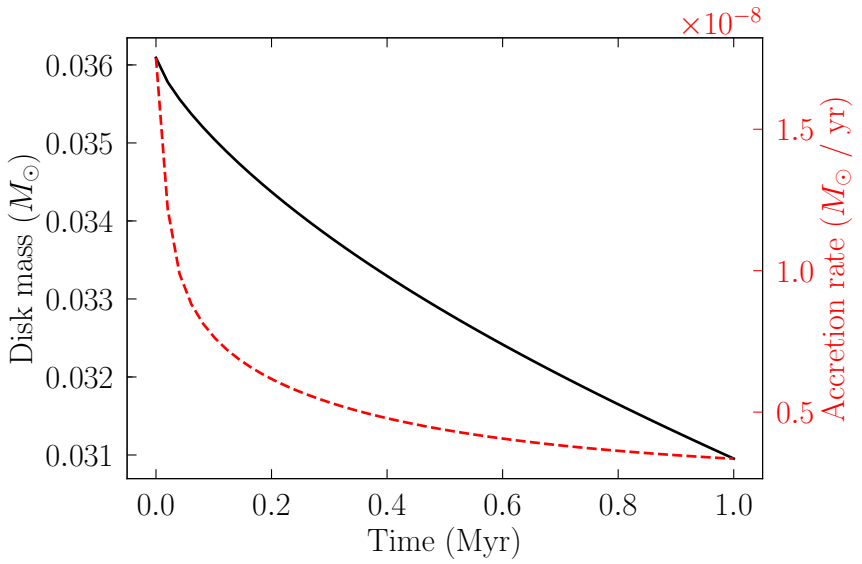

Figure 2.3: Total disk mass (black, solid line) and accretion rate (red, dashed line) as a function of time.

surface density profile. These tracks are given by the solution to the differential equation

$$u_R = -\frac{3}{R^{1/2}\Sigma}\frac{\partial}{\partial R}\left(R^{1/2}\nu\Sigma\right) \tag{2.10}$$

(e.g., Clarke & Carswell, 2007), where u_R is the velocity in the radial direction. Once the solution for Σ is known, this equation may be solved numerically. In Figure 2.4 we show several representative solutions with the temperature, density, surface density, and cosmic ray rate evaluated along the midplane tracks. Note that for many of the tracks the changes in temperature, density, and cosmic ray ionization are small to moderate. The only track that experiences order of magnitude changes in any of these physical variables is the 5→1 au track.

We follow tracks in the disk midplane for 1 Myr, the typical lifetime of a protoplanetary disk (Furlan et al., 2009; Mamajek, 2009), with the exception of tracks that cross 1 au, in which case we stop the track as it is crossing. We impose the radius restriction to avoid any effects from our inner boundary condition, which, as discussed above, was imposed to ensure that the solution is unique. Though dust growth will occur on similar time scales as those we consider, this effect is ignored in the present study to isolate the effects of gas dynamics.

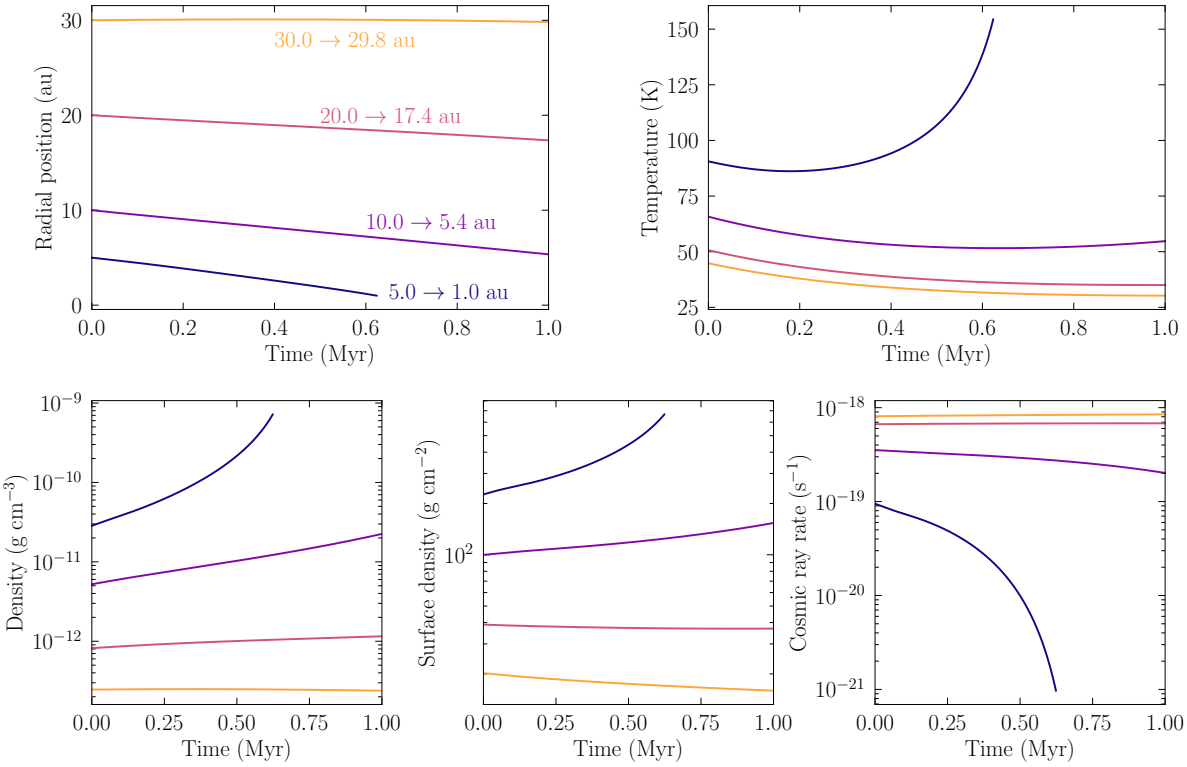

Figure 2.4: Change in physical variables (temperature, density, surface density, and cosmic ray rate) along tracks through the disk, as a function of starting radius. Note that density, surface density, and temperature changes with time are due to a combination of inward movement, which generally implies increasing density, surface density and temperature, an overall decreasing disk mass, and an evolving star, which decreases in luminosity with time. The strong decrease in cosmic ray ionization rate during the 5 → 1 au track is due to efficient attenuation of cosmic rays in the inner, high-surface density disk. Tracks are computed as described in Section 2.3.

Disk chemistry

Our disk chemistry code builds on that of Fogel et al. (2011) and Cleeves et al. (2014a), which itself is a modified version of ALCHEMIC (Semenov et al., 2010). The Fogel et al. (2011) code calculates the chemical evolution in zones that are completely independent and stationary. We instead consider parcels that are independent but not stationary, following accretion tracks through the disk, as described above. Because the tracks do not cross, the chemical evolution can be treated as a postprocessing step once the surface density model is determined.

To compute the change in abundance of each chemical species as a function of time, we must ac-

count for the fact that both the number of each species *and* the volume[3] of the gas parcel are changing as functions of time, due to the chemistry and dynamics, respectively.

We denote the number density of a single species i as $n_i \equiv N_i/V$, where N_i is the number of species i and V is the volume of the gas parcel. Applying the quotient rule for derivatives to n_i, we find that

$$\frac{\mathrm{d}n_i}{\mathrm{d}t} = \frac{1}{V^2}\left(V\frac{\mathrm{d}N_i}{\mathrm{d}t} - N_i\frac{\mathrm{d}V}{\mathrm{d}t}\right) = \left.\frac{\mathrm{d}n_i}{\mathrm{d}t}\right|_V + \left.\frac{\mathrm{d}n_i}{\mathrm{d}t}\right|_{N_i}. \tag{2.11}$$

We can identify the first term as the rate of change of n_i due to chemistry alone and the second term as the rate of change of n_i due to dynamics alone.

The first term, the rate of change due to chemistry, is straightforward to compute given a chemical network defining all possible reactions. Consider two types of chemical reactions, those for which n_i is a reactant (Equation 2.12) and those for which n_i is a product (Equation 2.13):

$$n_i + n_j \rightarrow \cdots \tag{2.12}$$

$$n_{j1} + n_{j2} \rightarrow n_i + \cdots \tag{2.13}$$

Let R_j be the rate of reaction j for which n_i is a reactant and let P_j be the rate of reaction j for which n_i is a product. Then,

$$\left.\frac{\mathrm{d}n_i}{\mathrm{d}t}\right|_V = \sum_j P_j n_{j1} n_{j2} - n_i \sum_j R_j n_j. \tag{2.14}$$

To write the second term, the rate of change due to dynamics, in terms of quantities we know, we apply the chain rule for derivatives, where the total mass density $\rho \equiv M/V$ for an unchanging parcel mass M:

$$\left.\frac{\mathrm{d}n_i}{\mathrm{d}t}\right|_{N_i} = N_i\frac{\mathrm{d}\left(\frac{1}{V}\right)}{\mathrm{d}t} = N_i\frac{\mathrm{d}\left(\frac{1}{V}\right)}{\mathrm{d}\rho}\frac{\mathrm{d}\rho}{\mathrm{d}t} = \frac{N_i}{M}\frac{\mathrm{d}\rho}{\mathrm{d}t} = \frac{n_i}{\rho}\frac{\mathrm{d}\rho}{\mathrm{d}t} \tag{2.15}$$

Using Equation 2.11, we construct a simultaneous system of coupled ordinary differential equations. We solve the system of equations using the CVODE code from the Lawrence Livermore National Laboratory SUNDIALS package (Hindmarsh et al., 2005); this code was chosen because it is

[3]The volume of the parcel is changing because, as the parcel approaches the star, the local density increases; as we are neither creating nor destroying matter, this directly corresponds to a volume decrease.

Species	Abundance	Species	Abundance
H_2	5.0×10^{-1}	O	1.0×10^{-8}
O_2	1.0×10^{-8}	He	1.4×10^{-1}
N_2	3.6×10^{-5}	CN	6.0×10^{-8}
H_3^+	1.0×10^{-8}	S^+	1.0×10^{-11}
Si^+	1.0×10^{-11}	Mg^+	1.0×10^{-11}
Fe^+	1.0×10^{-11}	CO	1.0×10^{-4}
C	5.0×10^{-9}	NH_3	8.0×10^{-8}
HCN	2.0×10^{-8}	C^+	1.0×10^{-10}
HCO^+	9.0×10^{-9}	C_2H	8.0×10^{-9}
H_2O(gr)	8.4×10^{-5}	CO(gr)	1.5×10^{-5}
CO_2(gr)	2.4×10^{-5}	CH_3OH(gr)	4.2×10^{-6}
NH_3(gr)	3.4×10^{-6}	CH_4(gr)	2.5×10^{-6}
GRAIN0	6.0×10^{-12}	GRAIN	6.0×10^{-12}

Table 2.3: Initial chemical abundance, which assumes inheritance from the molecular cloud stage. The species' abundances are given with respect to total hydrogen.

efficient, under current development, and easily accessed from C. The system is stiff (meaning that reactions occur on many different timescales), so we choose the backward differentiation formula (BDF) method with Newton iteration. The linear system is large and sparse, so we use MUMPS (Amestoy et al., 2001a, 2006) as a direct solver, through the PETSc interface. Our initial chemical abundances are given in Table 2.3 and are characteristic of observed molecular cloud and protostellar envelope abundances; the values are inspired by Aikawa & Herbst (1999), updated by Fogel et al. (2011), and further updated with ice abundances from observations of protostellar envelopes (Boogert et al., 2015). The physical conditions are updated at each time step according to the surface density solution, which need only be computed once.

2.4 Results

To explore the importance of gas accretion dynamics for the chemical evolution of a disk, we run three simulations for a given starting radius: one with the full dynamical treatment (the dynamic model), one with a fixed position at the initial radius of the track (the initial point evolution model), and one with a fixed position at the end radius of the track (the final point evolution model).

Though the radius R remains fixed for these static models, the local physical conditions are allowed to vary as the disk evolves. All simulations are run for 1 Myr, except when a track reaches 1 au before that time has elapsed.

Effect of adding dynamics

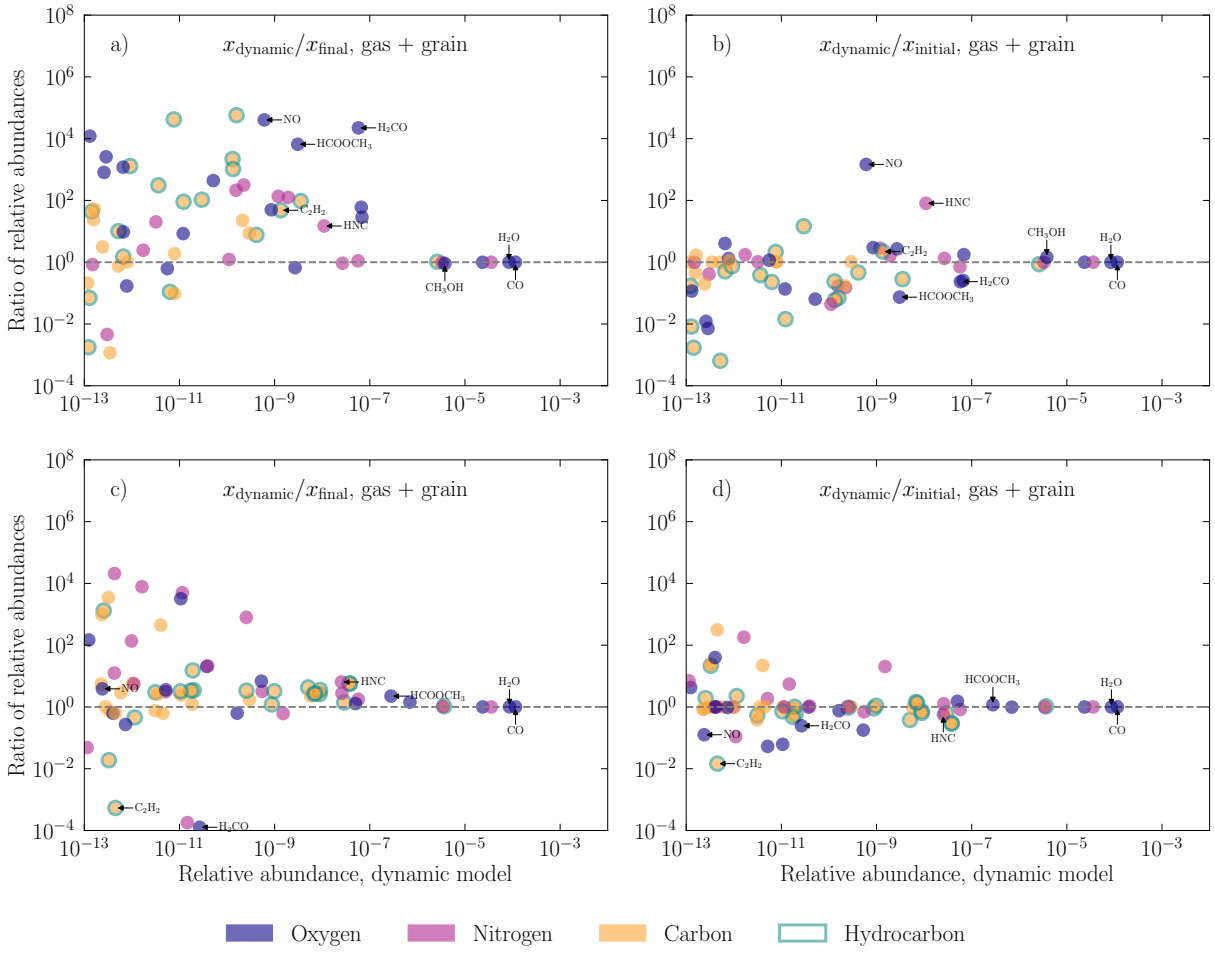

Figure 2.5: For dynamic tracks that evolve from 5 au (top row) and 10 au (bottom row), we show the relative abundances (gas + grain) of various species in our dynamical model compared to the final point evolution (left column) and to the initial point evolution (right column). Species are color-coded by the heaviest atom in the species; for example, the heaviest atom in CO_2 would be oxygen, and the heaviest atom in HNC would be nitrogen. Interesting chemical families have color-coded borders as indicated in the lower key. The dashed horizontal line indicates where the abundances would be identical in the dynamic and static models. Any species that appears above the line is overproduced when dynamics are included. Molecules that are discussed in the text are labelled.

In Figures 2.5a and 2.5b, we compare the *total* (that is, gas and solid phases combined) final relative abundances[4] of the $5 \rightarrow 1$ au model to those of the two static point models at 5 au and 1 au. By comparing the total quantity, we remove the effects of sublimation, i.e., snowline crossings, enabling us to isolate overall compositional changes. In each case, the ratio of abundances between the dynamic and static models are plotted against the abundance with respect to hydrogen in the dynamic model, all at the end of the simulation.

Chemical families of interest have been highlighted with colored outlines, and the inner color of each point corresponds to the heaviest atom in the molecule. Figure 2.5 shows that most species are enhanced in the dynamic model compared to the final point model, often by orders of magnitude. The notable exceptions are the handful of highly abundant species at the model inception, such as H_2O, CO and CH_3OH. There are ∼20 substantially-enhanced ($x_{\rm dynamic}/x_{\rm static} > 10$) and abundant ($x_{\rm dynamic} > 10^{-10}$) species at the end of the $5 \rightarrow 1$ au dynamic model track as compared to the static point model run at 1 au, and these are listed in Table 2.4.

Most of the enhanced species are carbon chains, more saturated hydrocarbons, and nitriles. There are also a few complex organic molecules that are ehanced, such as CH_3OCH_3 and $HCOOCH_3$. Only two species, HNC and NO (see Table 2.4), are more than one order of magnitude enhanced when comparing the $5 \rightarrow 1$ au dynamic track and the 5 au (initial point) static model. This behavior indicates that much of the 1 Myr chemical composition in the dynamic track is set by reactions close to the starting point of the track, which is then transported inwards. The depletion of many species compared to the initial point model (Figure 2.5) shows that the survival is not perfect, however, and both transport and local chemistry needs to be taken into account when modeling chemical abundances in the inner disk.

Figures 2.5c and 2.5d show the analogous data for the track beginning at 10 au. In contrast to the $5 \rightarrow 1$ au track, the $10 \rightarrow 5$ au track presents few species that are both abundant and substantially

[4]Throughout this section and others, we will refer to the "relative abundance" of a species. Generally, one normalizes the absolute abundance by $[\mathrm{H}] + 2[\mathrm{H_2}]$. However, we find that there may be substantial amount of hydrogen in less abundant species, which can introduce a systematic error in the relative abundances. To avoid this problem, we total the amount of hydrogen across all species and normalize by this quantity.

enhanced compared to the final point model. A quite small difference of 5 au vs. 10 au in starting radius thus result in a large difference when evaluating the role of dynamics in disks. Furthermore, there is not necessarily a consistent enhancement/depletion pattern between the two scenarios. Some species, such as C_2H_2, which were enhanced in the 5 au dynamic model compared to the final point static model, are now *depleted* when adding dynamics to the 10 au model (Figure 2.5c).

For tracks starting at radii $R \geq 20$ au, we see little to no chemical difference between the initial, final, and dynamic models. This can be understood when considering that the physical conditions do not change significantly along these tracks, and, where there are changes, they tend to be towards lower temperatures and densities, which typically decrease the chemical reaction rates.

In summary, adding dynamics in the form of inward accretion streams has a large effect on the chemical evolution of the innermost disk as exemplified by the 5 to 1 au track, while the effects on the chemical evolution exterior to 5 au are small. In all models, adding accretion dynamics does not affect the abundances of the initially most abundant molecules such as CO and H_2O, which on our timescales are not substantially destroyed or enhanced.

Carbon and nitrogen in organics

One interesting question for planet formation is whether adding dynamics changes the overall organic composition at different disk locations[5]. We assess this by considering the fraction of N and C in organic form in the static and dynamic tracks.

In Figure 2.6, we show the time evolution of the total amount of carbon and nitrogen in organics for the different dynamic tracks considered in the previous section compared to their static counterparts. The carbon in organics changes very slightly on the 5 au dynamic track. The change increases moving to the 10 au dynamic model, but is still modest; adding dynamics changes the carbon in organics by less than 10%. We note that the effect of adding dynamics on the fraction of carbon in organics can produce different outcomes: The dynamic $5 \rightarrow 1$ au model ends with an in-

[5]Here, "organic" refers to a gas- or solid-phase molecule or ion that contains both hydrogen and carbon.

Species	Abundance w.r.t. hydrogen	Enhancement
Comparing to final point model		
C_2H_2	1.3×10^{-9}	4.8×10^{1}
C_2H_2N	2.2×10^{-10}	3.2×10^{2}
C_2H_3N	1.5×10^{-10}	2.1×10^{2}
C_2H_4	3.5×10^{-9}	9.6×10^{1}
C_3	2.1×10^{-10}	2.2×10^{1}
C_3H_2	1.3×10^{-10}	2.2×10^{3}
C_3H_3	1.6×10^{-10}	5.8×10^{4}
C_3H_4	1.3×10^{-10}	1.0×10^{3}
CH_3N	1.9×10^{-9}	1.3×10^{2}
CH_3OCH_3	6.6×10^{-8}	6.0×10^{1}
CH_5N	1.2×10^{-9}	1.4×10^{2}
H_2CO	5.8×10^{-8}	2.2×10^{4}
$HCOOCH_3$	3.1×10^{-9}	6.6×10^{3}
HNC	1.1×10^{-8}	1.5×10^{1}
N_2O	8.5×10^{-10}	5.0×10^{1}
NH_2CHO	6.9×10^{-8}	2.8×10^{1}
NO	6.1×10^{-10}	4.1×10^{4}
Comparing to initial point model		
HNC	1.1×10^{-8}	8.1×10^{1}
NO	6.1×10^{-10}	1.5×10^{3}

Table 2.4: Total (gas + grain) abundances of significantly enhanced, abundant species in the dynamic model compared to the two static point evolution models for the 5 au track.

termediate carbon fraction in organics compared to the two static counterparts, while the dynamic $10 \rightarrow 5.4$ au model ends with a lower carbon fraction than either static model.

The fraction of nitrogen in organics is more sensitive to whether or not dynamics is taken into account. In the $5 \rightarrow 1$ au dynamic model, the nitrogen fraction in organics ends at a value higher than either static model but is closer to that of the initial point model; in the $10 \rightarrow 5.4$ au dynamic model, the nitrogen fraction is instead lower than either static model but is still closer to the value along the initial point model. There is an almost 50% change in the nitrogen fraction along both the 5 au and 10 au dynamic tracks.

At the end of the 5 au dynamic track, the nitrogen-bearing organic with the highest abundance is NH_2CHO. NH_2CHO forms efficiently from NH_2 and H_2CO at early times, and this enhancement is then transported inwards, increasing the overall nitrogen fraction in organics. At the end of

the 5 au track, NH_2CHO comprises about 35% of all nitrogen in organics.

At the end of the 10 au dynamic track, the nitrogen-bearing organic with the highest abundance is instead H_2CN ice. This molecule accounts for about 52% of all nitrogen in organics at the end of the track.

Effect of cosmic rays

We may suspect that cosmic rays play a significant role in the disk chemistry of our dynamic models, given their stated importance in previous static models (Cleeves et al., 2014b; Eistrup et al., 2016). Evidence for this behavior comes from the fact that the dynamic track's evolution tends to more closely resemble the initial point model than the final point model, so much of the chemical processing must happen near the initial position of the gas parcel. Without cosmic rays playing a large role, this would be counterintuitive, since, for inward-moving tracks, the end of each track has higher temperatures and densities that would drive chemical processing at a higher rate than at the beginning of the track. By contrast, the cosmic ray flux in the midplane is at its *highest* at the beginning of the track (Figure 2.4), where the surface density is lowest. Cosmic rays, then, provide a mechanism by which chemistry may be faster at lower disk temperatures and densities.

Figure 2.7 shows a comparison between the $5 \rightarrow 1$ au and $10 \rightarrow 5$ au fiducial dynamic models and their counterparts with the cosmic ray flux set to zero at all times and radii. We clearly see that including cosmic rays has a dramatic effect on the chemistry along these tracks. Including cosmic rays increases the abundances of many species. We note that this is especially true for the families of molecules that were enhanced in the fiducial models compared to he static models, such as hydrocarbons, which generally appear below the dashed line, where the two models would have equal abundances.

2.5 Discussion

General trends

In this section we discuss the origin of the enhancement patterns we see in the 5 au and 10 au tracks. In general, we find that including cosmic rays tends to enhance many species by the endpoint of an inward-moving track and we thus suspect that many of the observed trends can be traced back to a cosmic-ray driven chemistry close to the initial point of the tracks where cosmic ray penetration to the midplane is the most efficient. Figure 2.8 (top and middle panels) shows that for the species enhanced in the dynamics $5 \rightarrow 1$ au track compared to the final point model, the chemical abundances are indeed mainly set during the first few hundred thousand years, when the gas parcel is > 4 au.

In more detail, we can see from Figure 2.8 (top panel) that some of the most abundant and enhanced hydrocarbons in our 5 au model — namely, C_2H_2, C_3H_4, and C_2H_4 — are produced rapidly at very early times and then experience a plateau until about 0.01 Myr, when they experience a second rapid growth. The initial increase in C_3H_4 and C_2H_4 is simply because atomic carbon is present in our initial condition, and this atom reacts readily to form these products. We expect this to hold at all radii.

The second growth step is more interesting and we examine the reaction rates, which allows us to isolate the dominant reaction pathways, for several species of interest. A representative example is C_2H_2, a hydrocarbon species observed in the inner disk with *Spitzer* (and may soon be observed with the *James Webb Space Telescope*) that is enhanced at the end of the $5 \rightarrow 1$ au track both when compared with the final point model and when compared to the endpoint of the same dynamic track without cosmic rays. We find the following pathway for the formation of C_2H_2 at 0.05 Myr along the 5 au track.

$$\begin{aligned} \mathrm{He} &\xrightarrow{\mathrm{CRP}} \mathrm{He^+ + e^-} \\ \mathrm{He^+ + CO} &\longrightarrow \mathrm{C^+ + O + He} \\ \mathrm{C^+ + CH_4} &\longrightarrow \mathrm{C_2H_3^+ + H} \\ \mathrm{C_2H_3^+ + NH_3} &\longrightarrow \mathrm{NH_4^+ + C_2H_2} \end{aligned} \tag{2.16}$$

Gas-phase C_2H_2 is thus produced by a reaction chain that begins with the ionization of helium. Through an electron exchange, a C^+ ion is produced, which then reacts with methane and ammonia to finally produce neutral C_2H_2.

A similar analysis of C_3H_4, shows that it forms from $C_2H_3^+$, where $C_2H_3^+$ is produced through the same pathway as listed above for C_2H_2.

$$\begin{aligned} C_2H_3^+ + CH_4 &\longrightarrow C_3H_5^+ + H_2 \\ C_3H_5^+ &\xrightarrow{gr^-} C_3H_4 + H \end{aligned} \tag{2.17}$$

The mechanism for producing C_2H_4, below, goes through a different set of species but still traces back to the high cosmic ray rate at 5 au:

$$\begin{aligned} C^+ + CH_3OH &\longrightarrow CH_4O^+ + C \\ C + H_2 &\longrightarrow CH_2 \\ H + CH_2 &\longrightarrow CH + H_2 \\ CH + CH_4 &\longrightarrow C_2H_4 + H. \end{aligned} \tag{2.18}$$

In summary, all hydrocarbons that are observed to be enhanced in the dynamic model, compared to the final point model, are enhanced due to the high level of cosmic ray ionization on the dynamic track compared to the final point model.

In Figure 2.5, we see that a few oxygen-bearing organics, including H_2CO and $HCOOCH_3$, are both enhanced along the 5 au track relative to its static final counterpart; yet, the related species CH_3OH is not significantly enhanced or depleted, though it is also more abundant than the aforementioned species. Figure 2.8 (middle panel) shows the complete time evolution of these two species. H_2CO and $HCOOCH_3$ have the same overall behavior, wherein the molecule has a plateau at early times, followed by a rapid growth beginning around 0.02 Myr. We determine the main formation pathways for both molecules at this time, similar to our analysis for hydrocarbons above. H_2CO is formed primarily from gas phase chemistry at 0.02 Myr by

$$O + CH_3 \longrightarrow H_2CO + H. \tag{2.19}$$

The radical precursor CH_3 comes in part from

$$\begin{aligned} H_3{}^+ + CO &\longrightarrow HCO^+ + H_2 \\ HCO^+ + CH_3OH &\longrightarrow CH_5O^+ + CO \\ CH_5O^+ + CH_3OH &\longrightarrow CH_3OCH_4{}^+ + H_2O \\ CH_3OCH_4{}^+ &\xrightarrow{gr^-} CH_3 + CH_4 + O. \end{aligned} \tag{2.20}$$

Essentially, CH_3OH is acting as a catalyst for the reactions but is not significantly produced or destroyed in the reaction scheme. Similar to the hydrocarbons, the reaction chain is initiate by cosmic ray chemistry, which is responsible for the formation of $H_3{}^+$. $HCOOCH_3$ mostly exists in its ice form, but it is initially formed in the gas phase (our model does not include a grain surface pathway) and then subsequently freezes onto grains. The gas-phase formation of $HCOOCH_3$ is

$$\begin{aligned} CH_5O^+ + H_2CO &\longrightarrow H_5C_2O_2{}^+ + H_2 \\ H_5C_2O_2{}^+ &\xrightarrow{gr^-} HCOOCH_3 + H; \end{aligned} \tag{2.21}$$

These reactions are initiated by the H_2CO as described in Equation 2.20, hence their linked time evolution.

Figure 2.5 shows that there are a few species, particularly NO and HNC, that are enhanced in our fiducial model compared to *both* static point models. This is interesting because it shows that the combination of transport and chemistry can result in excess production of some molecules in the disk midplane beyond any static model predictions. Figure 2.8 shows the time-dependent behavior of NO, HNC, and OCN, a possible precursor of NO. At 0.3 Myr, HNC is primarily formed by:

$$\begin{aligned} HCO^+ + HCN &\longrightarrow HCNH^+ + CO \\ HCNH^+ + NH_3 &\longrightarrow NH_4{}^+ + HNC. \end{aligned} \tag{2.22}$$

At the same time point, NO is produced from

$$\begin{aligned} HCO^+ + NH_2CHO &\longrightarrow NH_2CH_2O^+ + CO \\ NH_2CH_2O^+ &\xrightarrow{gr^-} OCN + 2\,H_2 \\ O + OCN &\longrightarrow NO + CO. \end{aligned} \tag{2.23}$$

The OCN precursor shows a similar growth behavior as NO at early times, but the two deviate dramatically as the parcel moves inward in the disk. In general we do not see a close connection between the abundances of different precursors and the final products, which implies that the production of NO and HNC, and by analogy many other molecules, are impossible to predict without running the full chemical code, including the relevant dynamics.

While we can trace enhancements of species many species in the dynamical model back to the high cosmic ray rate at the beginning of the 5 au track, this is not true for every single species. In addition to the transport of cosmic-ray initiated chemistry at larger radii, we also see some species who enhancement is due to a complex interaction between transport and local chemistry. Second, we find that there are some chemical families that are more sensitive to the addition of dynamics then others. Hydrocarbons as a family tend to be enhanced in the dynamic model compared to the static final point model, as are some oxygen-bearing organics and complex nitriles (Figure 2.5). We emphasize, however, that it is virtually impossible to know *a priori* which particular species will be enhanced due to inward transport and chemistry and which will barely be effected without actually running the complete model. The one exception to this rule may be the survival of initially very abundant, stable molecules, which in our models maintain close to their initial abundances at all investigated times and locations.

Comparison to existing models

When comparing our dynamic and static chemistry model outcomes to the most similar model in the literature by Heinzeller et al. (2011), we find both similarities and differences. Table 2.5 summarizes the this comparison. H_2O is barely affected by the inclusion of dynamics in both models. NH_3 is also not strongly affected in either model, though what little effect there is goes in opposite directions. Both models predict some CH_3OH depletion in dynamic compared to static 1 au models, but the magnitude of the depletion differs. The biggest difference is for C_2H_2, however, where we find a large enhancement when including dynamics due to inward transport of cosmic ray-mediated chemistry, while Heinzeller et al. finds a depletion.

Species	This work	$10 \times \zeta_{CR}$	$2 \times T_{gas}$	$2 \times T_{gas}$ and $10 \times \zeta_{CR}$	Heinzeller et al. (2011)[a]
H_2O	1	1	1	1	1
NH_3	1	0.8	1	0.9	1
CH_3OH	0.9	0.4	0.9	0.4	0.03
C_2H_2	50	200	5	1	0.008

Table 2.5: Comparison to Heinzeller et al. (2011) model ACR; we list the ratio of the dynamic model value (either number density or column density) to its corresponding static model value. A value of unity indicates no change, while values less than or greater than unity indicate depletion or enhancement, respectively.

[a] Heinzeller et al. (2011) Table 3 lists the column densities for the species of interest. Since we do not have column densities for our midplane model, we warn the reader against comparing the table values directly.

An important difference between the two models, and therefore a potential source of the different model outcomes, is the treatment of cosmic rays. The Heinzeller et al. model computes its cosmic ray ionization rate from the density profile and dust opacity of Nomura et al. (2007). This model is different from ours and will therefore predict different levels of attenuation. More importantly, Heinzeller et al. adopts an unattenuated cosmic ray ionizaton of $\zeta_{CR} = 10^{-17}$ s^{-1}, whereas we have used $\zeta_{CR} = 10^{-18}$ s^{-1} in our models, following models by Cleeves et al. (2014a). To test whether this explains the different model outcomes, we reran our dynamic and static models with an order of magnitude higher cosmic ray ionization rate (see figure in the Appendix). While an enhanced cosmic ray ionization rate has a clear impact on the disk chemistry and changes the relative enhancements of many molecules in the dynamics vs. static models, theC_2H_2 enhancement seen in the fiducial model is preserved. The mechanism which produces C_2H_2 at early times is the same as that given in Equation 2.16. Different cosmic ray ionization rates alone does hence not explain the model differences.

A second difference between the two models is that the Heinzeller et al. (2011) disk is warmer than the model presented here. To explore if the different temperature profiles can explain the observed chemical differences, we also ran models with an artificially boosted temperature profile,

keeping the tracks the same[6]. We tested this warmer disk at both the fiducial and increased cosmic ray rate. The results of these trials are summarized in Table 2.5. No combination of parameters results in a depletion of C_2H_2, but in the warmer disk with high cosmic ray flux (i.e. the model that is most similar to Heinzeller et al. 2011), we no longer produce a substantial C_2H_2 enhancement. In this model fast reactions consume C_2H_2 at the final time, incorporating C_2H_2 into larger molecules like $C_5H_4N^+$ and $C_6H_5^+$. We note that this test implies that both our and their model results are sensitive to the precise disk structural model, which needs to be taken into account when directly interpreting disk chemistry results from observations.

Simplifying assumptions

To make the code computationally efficient, we have imposed a number of simplifying assumptions. One such assumption is that we do not presently consider vertical mixing in our disk model. Other studies have considered the impact of vertical mixing of gas and with solids on disk chemistry. Furuya et al. (2013) found in their models that vertical mixing significantly decreased the column density of water ice in the disk. Kama et al. (2016) found a sequestration of carbon due to the vertical transport of carbon- and oxygen-bearing material from the disk surface to the midplane, where it freezes out onto grains. Ciesla & Sandford (2012) found that mixing of grains enhanced their UV exposure during the disk lifetime, which facilitates the production of organics.

To evaluate the potential impact of treating the midplane in isolation, we follow Semenov & Wiebe (2011) and compute the turbulent mixing timescale for the disk parameters we use. Under our assumptions, we find the temperature-dependent terms cancel, and the turbulent mixing timescale becomes a function of radius only,

$$\tau_{\rm phys} = h^2/D_{\rm turb} = \frac{\rm Sc}{\alpha\Omega}, \tag{2.24}$$

where Sc is the Schmidt number, which encodes the efficiency of turbulent diffusivity (Semenov & Wiebe, 2011); h is the scale height of the disk; $D_{\rm turb}$ is the diffusion coefficient; α is the dimension-

[6]This is not, strictly speaking, a fully consistent approach, since the temperature profile also influences the tracks through the surface density evolution equation.

less viscosity parameter; and Ω is the orbital angular velocity. Substituting the relevant numbers, and evaluating this expression at 1 au and 10 au, we find timescales of 160 Sc yr and 5000 Sc yr, respectively. Note that the value of α we assume, 10^{-3}, is informed by measurements from Flaherty et al. (2018), who measure low turbulence in the TW Hya disk.

Taking $\mathrm{Sc} = 1$ and $\mathrm{Sc} = 100$ as two possible values (the same values considered by Semenov & Wiebe 2011), these timescales will always be shorter than the $\sim 10^6$ yr timescale for surface chemistry (neglecting tunneling) at the disk midplane quoted from Semenov & Wiebe (2011), and if mixing is efficient we would therefore expect it to change grain surface compositions. We also consider how τ_{phys} compares to the gas-phase processes in the disk. Ion-molecule chemical reactions have a typical timescale on the order of 10^0 – 10^1 yr (Semenov & Wiebe, 2011), which is short compared to mixing time scales at all relevant disk radii. Whether or not mixing could affect our results is thus a complex question, which depends on the relative importance of gas and grain surface chemical processes. We note that hydrocarbons, the species most affected by including dynamics in our model, are mainly gas phase chemistry products and we therefore expect this result to hold, while many of O-bearing organics, which form partially or wholly on grains, may be more sensitive to mixing. This is also in line with the findings of Semenov & Wiebe (2011).

Whether inner disk midplanes are subject to substantial vertical mixing is somewhat unclear, however. The few observational constraints on disk turbulence that exist are based on observations of gas in the outer disk, and typically well above the midplane. Based on such observations, Teague et al. (2016), for example, measured $v_{\mathrm{turb}} \sim 0.2$ – $0.4 c_s$ in TW Hya. Hughes et al. (2011) found $\alpha \sim 0.01$ in HD 163296, and Flaherty et al. (2018) found evidence for low turbulence in TW Hya with $\alpha < 0.007$. These low turbulence measurements may not be surprising because the magneto-rotational instability (MRI) may not be as active as originally thought (Simon et al., 2018). Additional observations are clearly needed to establish levels of turbulence at all disk scales as the effects will likely be chemically important.

In addition, the present prescription does not allow for mixing of the gas or mixing of the dust between different radial regions. Dust actively evolves by growth and fragmentation in protoplan-

etary disks (e.g., Dullemond & Dominik, 2005). These processes influence the dust surface area relative to volume, and therefore we expect it to impact chemistry. However, dust evolution likely cannot be explained by a simple monotonic growth, and therefore would require a full treatment of dust evolution, which is beyond the scope of this paper.

2.6 Conclusions

We have undertaken a self-consistent model of midplane disk chemistry and dynamical evolution that includes viscous accretion, under the assumption of well-coupled gas and dust. We find that taking accretion into account, and the associated changes in physical conditions along a gas parcel's journey, can substantially change the abundances of many species within 10 au. Many of these species are enhanced because of cosmic ray-driven reactions in the outer disk, which are then transported into the "cosmic ray dark" inner disk regions where the gas attenuation is very high. There are, however, also species that are depleted when including dynamics, and predicting *a priori* how the chemistry will be affect by the inclusion of dynamics is challenging. Abundant species — most notably H_2O, CO_2 and CO — are largely unaffected by the inclusion of dynamics, so a static model would approximate their abundances well. Any individual species' enhancement or depletion can be very sensitive to the incident flux of cosmic rays, and quantitative comparisons with observations will require better constraints on this fundamental parameter.

E.M.P. gratefully acknowledges support from National Science Foundation Graduate Research Fellowship Program (GRFP) grants DGE1144152 and DGE1745303. This work was supported by an award from the Simons Foundation (SCOL # 321183, KO).

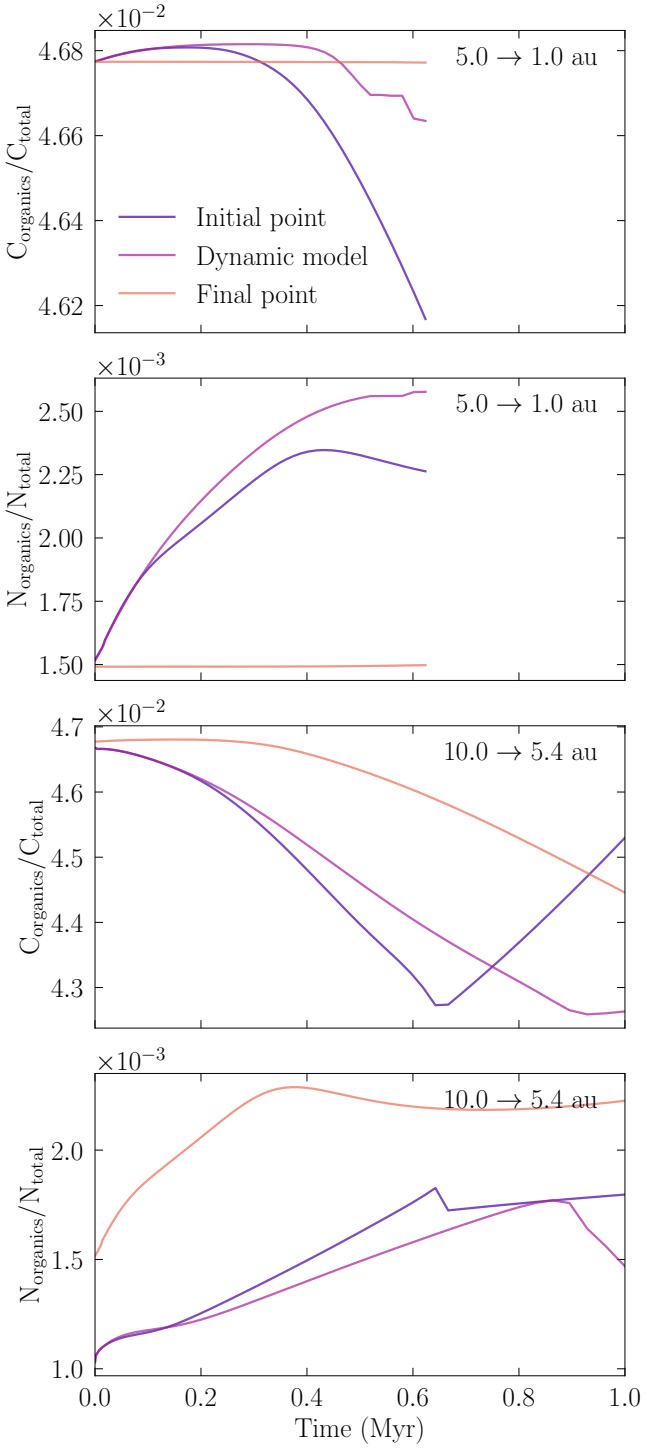

Figure 2.6: Time evolution of the amount of carbon and nitrogen in organics (gas and grain), expressed relative to the total amount of carbon and nitrogen, respectively. Two different initial radii, 5 au and 10 au, are shown; the top two panels are for the 5 au track, while the bottom two panels are for the 10 au track.

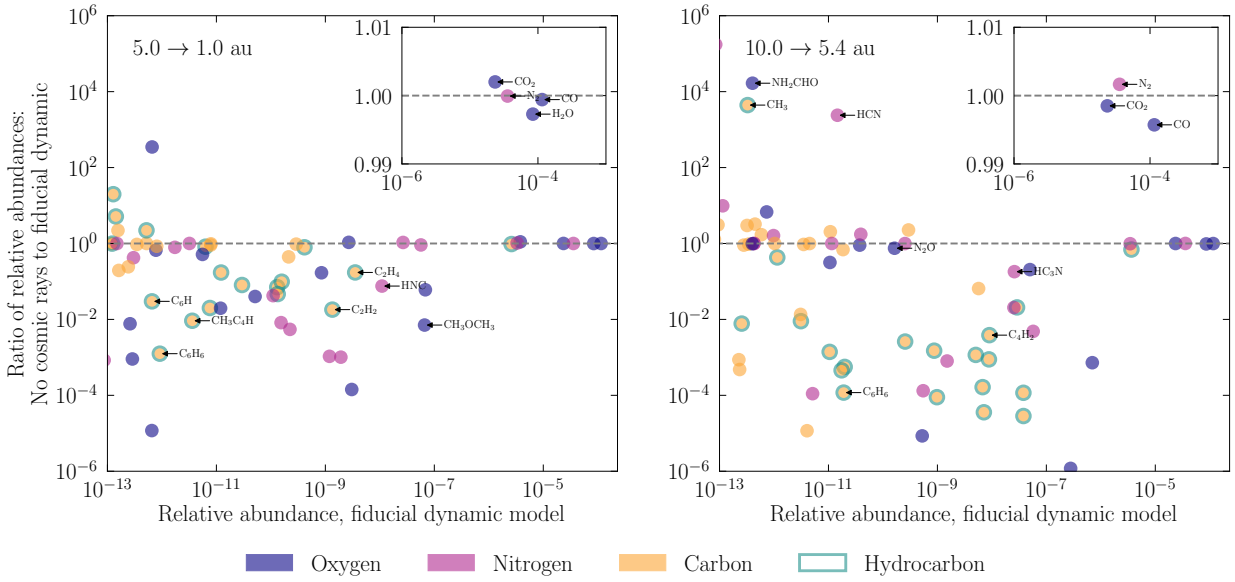

Figure 2.7: Comparison of two dynamic track models to identical models without cosmic rays. The gray dashed line indicates where the two models would produce the same results. Note that the value plotted is the total (gas + grain) relative abundance of each species. Inset axes are included to emphasize the small, but sometimes significant, enhancement or depletion of very abundant species, such as H_2O and CO_2.

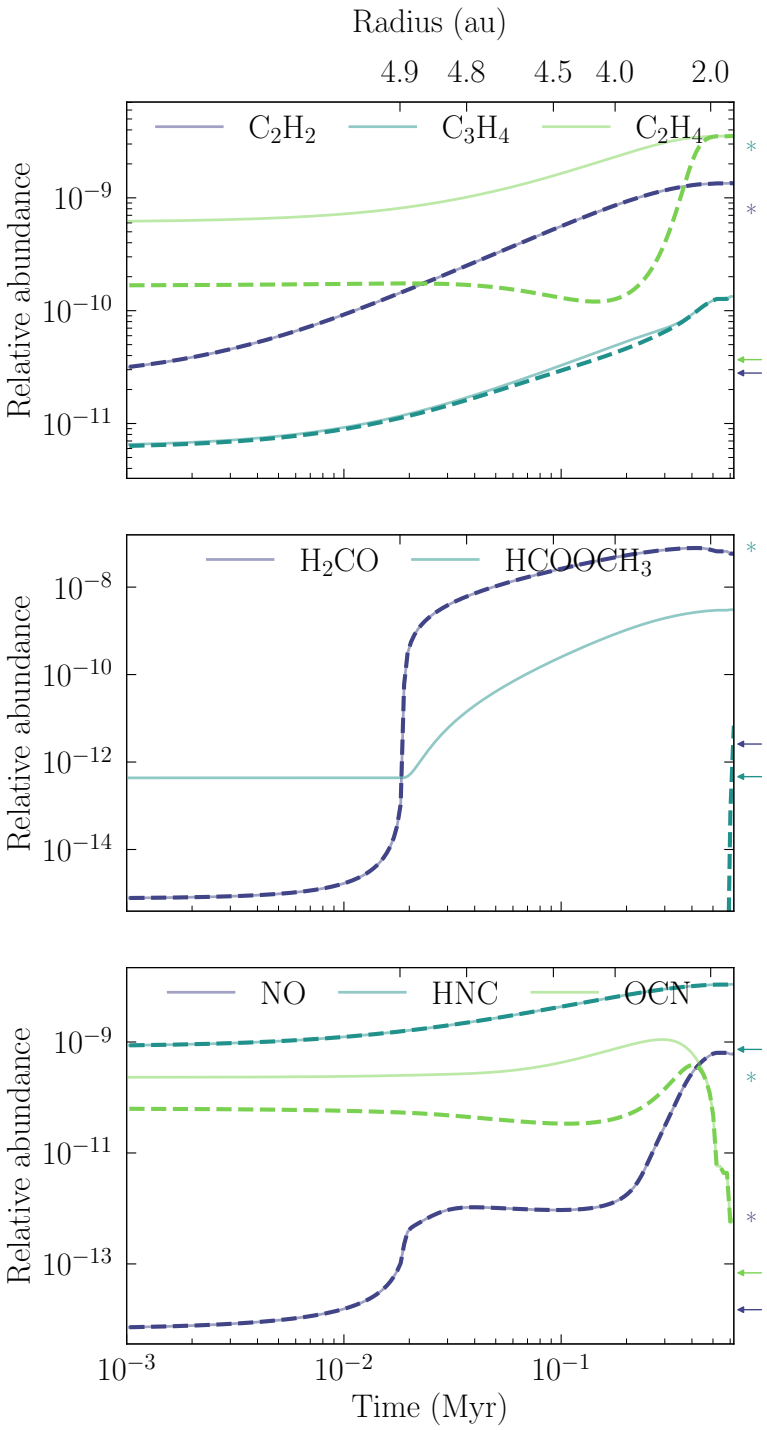

Figure 2.8: Time-dependent behavior of several species called out in the text, all along the 5 au dynamic track and its static counterparts. Solid lines show the time-dependent behavior of the total abundance in our fiducial model, while dashed lines show the gas phase evolution in the fiducial model. At the far right, we show the final values corresponding to the initial point (stars) and final point (arrows) models.

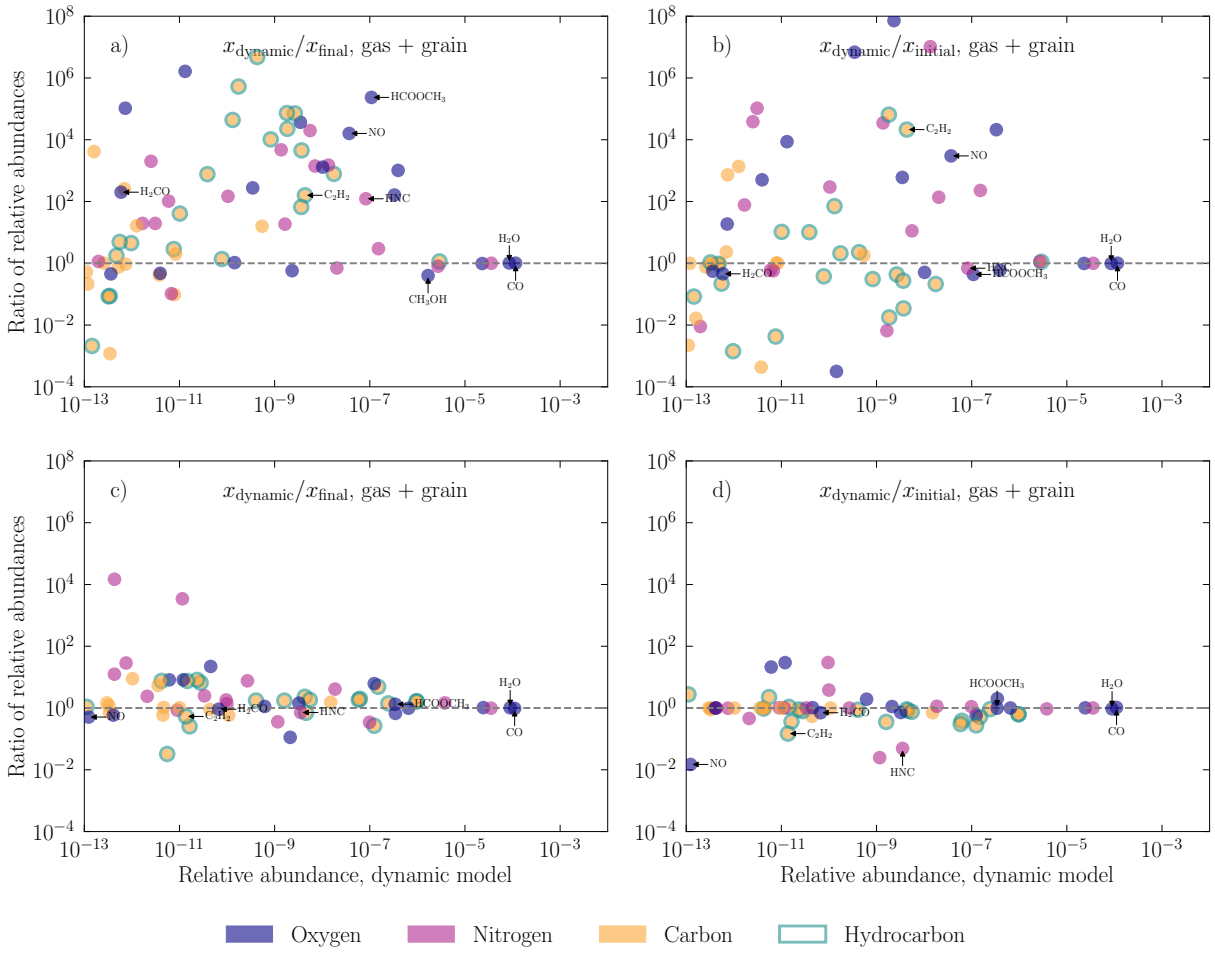

Figure 2.9: Analogue of Figure 2.5 using the higher cosmic ray ionization rate consistent with Heinzeller et al. (2011), $\zeta_{\rm CR} = 10^{-17}$ s^{-1}.

Chapter 3

Ice-Coated Pebble Drift as a Possible Explanation for Peculiar Cometary CO/H_2O Ratios

This chapter has been accepted for publication in The Astrophysical Journal,

but an identifier has not been assigned at this time.

©AAS. Reproduced with permission.

3.1 Abstract

To date, at least three comets — 2I/Borisov, C/2016 R2 (PanSTARRS), and C/2009 P1 (Garradd) — have been observed to have unusually high CO concentrations compared to water. We attempt to explain these observations by modeling the effect of drifting solid (ice and dust) material on the ice compositions in protoplanetary disks. We find that, independent of the exact disk model parameters, we always obtain a region of enhanced ice-phase CO/H_2O that spreads out in radius over time. The inner edge of this feature coincides with the CO snowline. Almost every model achieves at least CO/H_2O of unity, and one model reaches a CO/H_2O ratio > 10. After running our simulations for 1 Myr, an average of 40% of the disk ice mass contains more CO than H_2O ice. In light of this, a population of CO-ice enhanced planetesimals are likely to generally form in the outer

regions of disks, and we speculate that the aforementioned CO-rich comets may be more common, both in our own Solar System and in extrasolar systems, than previously expected.

3.2 Introduction

Comets provide a unique window onto the ice-phase chemistry of a protoplanetary disk. These frozen remnants are generally considered to be the most pristine record available for understanding disk midplanes' compositions. The chemical species present in solar system comets and their relative abundances provide unique and detailed insights into the protoplanetary disk that formed our planetary system (Mumma & Charnley, 2011; Altwegg & Bockelée-Morvan, 2003), and, more recently with the discoveries of passing extrasolar comets (Strøm et al., 2020), other planetary systems.

Water is typically the most abundant volatile species in cometary nuclei, with carbon monoxide comprising between about 0.2% to 23% relative to water, with a typical value around 4% (Bockelée-Morvan & Biver, 2017). However, at least three notable exceptions have been observed. Specifically, the interstellar comet 2I/Borisov was measured to have CO/H_2O between 35% and 173% (Cordiner et al., 2020; Bodewits et al., 2020), significantly higher than the average cometary values for the Solar System. Bodewits et al. (2020) suggest 2I/Borisov's composition could be explained by an unusual formation environment beyond the CO snowline, and, statistically, it is more likely that 2I/Borisov is a typical comet for its system. However, given the ubiquity of water in interstellar clouds (Boogert et al., 2015), it would be challenging to have a scenario with CO ice freezing out without abundant water ice, which has a higher binding energy than CO. At least two additional comets, C/2009 P1 (Garradd) and C/2016 R2 (PanSTARRS), which originate in our own solar system, have high CO abundances as well: C/2009 P1 (Garradd) has a CO production rate of 63% that of water (Feaga et al., 2014), and C/2016 R2 (PanSTARRS) has an even higher CO production rate than 2I/Borisov (Biver et al., 2018; McKay et al., 2019). Although these comets represent a very small fraction of the comets for which CO/H_2O has been measured, they are more difficult to explain. Therefore we need a mechanism that can both create enhanced CO to H_2O ratios compared to interstellar or

disk-averaged CO/H_2O abundance ratios *and* create a spread of CO to H_2O within a disk like our solar nebula.

What kinds of mechanisms could explain these unusual compositions both interior and exterior to our solar system? Biver et al. (2018) suggest that C/2016 R2 could be a piece of a differentiated comet; Cordiner et al. (2020) suggest the same for 2I/Borisov. De Sanctis et al. (2001) found that CO and other volatiles could almost be completely absent in the upper layers of a hypothetical differentiated comet; in this scenario, 2I/Borisov and C/2016 R2 could be pieces of the cores of such differentiated comets. Alternatively, the chemistry of the planet-forming disk could evolve over time to create exotic compositions at different disk locations. For example, Eistrup et al. (2019) consider several comets and attempt to reproduce their molecular abundances with a model protoplanetary disk. Their disk model produces a maximum CO/H_2O ratio of about 1% over a range of disk radii from 15 au to 30 au from the central star. However, to reproduce a comet like 2I/Borisov, we would require a ratio that could be as high as 100%.

In recent years, dust transport, especially radial drift, has been found to be an important factor in shaping the solid mass distribution in disks (Testi et al., 2014; Piso et al., 2015; Öberg & Bergin, 2016; Cridland et al., 2017b). If the timing of volatile freeze out and dust transport due to, e.g., drift, are not synced, it could become possible to create a variety of ice compositions purely due to dust dynamics.

In this paper, we explore whether a comet such as 2I/Borisov or C/2016 R2 (PanSTARRS) could form in a pocket of CO-rich material in an otherwise H_2O-rich disk as a result of dust transport, and under what conditions such pockets could form. The paper is structured as follows. In Section 3.3, we explain the equations and software used to define our disk model. Section 3.4 presents our calculated CO/H_2O ice ratios across a generic protoplanetary disk. We discuss the implications of these results in light of the recent findings of comets and an exo-comet with high CO abundance in Section 3.5 and conclude in Section 3.6.

The authors note that a similar paper (Mousis et al., 2021) appeared independently during the review process for this paper.

3.3 Methods

Our goal is to globally simulate the surface densities of solids and gas in a protoplanetary disk, incorporating simple adsorption and desorption processes for the chemical species we consider, H_2O and CO. We build on the physical models of disk gas and dust following Lynden-Bell & Pringle (1974) and Birnstiel et al. (2010). In addition, we take into account the time evolving disk temperature due to the pre-main sequence stellar evolution over the time scales of our model simulation. The following sections detail these model components.

Gas dynamics

To model the dynamics of the gas bulk (defined as the bulk hydrogen gas, which experiences no source terms), we follow Lynden-Bell & Pringle (1974), which is based on the α-disk model of Shakura & Sunyaev (1973). Thus, we have the partial differential equation

$$\frac{\partial \Sigma_{\rm gas}}{\partial t} - \frac{3}{R}\frac{\partial}{\partial R}\left[R^{1/2}\frac{\partial}{\partial R}\left(\nu \Sigma_{\rm gas} R^{1/2}\right)\right] = 0 \tag{3.1}$$

in the absence of sources and sinks, where $\Sigma_{\rm gas} \equiv \int \rho_{\rm gas}\, {\rm d}z$ is the surface density of gas, ν is the viscosity, R is the distance from the star in the x-y plane, and t is time. Viscosity is, in turn, given by

$$\nu = \alpha c_s^2 / \Omega \tag{3.2}$$

where α is a small parameter of our choosing, typically set to 10^{-4} to 10^{-2}; c_s is the local sound speed, given by

$$c_s = \sqrt{\frac{k_B T}{\mu m_p}}, \tag{3.3}$$

where k_B is Boltzmann's constant, T is the local temperature, μ is the mean molecular weight, and m_p is the proton mass; and Ω is the Keplerian angular frequency,

$$\Omega = \sqrt{\frac{G M_\star}{R^3}}, \tag{3.4}$$

with G the gravitational constant and $M_\star$ the central stellar mass. Equations 3.1, 3.2, 3.3, and 3.4 completely define the model of the gas bulk given parameters μ, $M_\star$, and α; the local temperature field $T = T(R, t)$ (see Section 3.3; and the initial condition $\Sigma_{\rm gas}(R, t = 0)$.

For the initial condition, we first define the self-similar solution,

$$\Sigma_{\rm ss}(R) = \Sigma_c \left(\frac{R}{R_c}\right)^{-\gamma} \exp\left[-\left(\frac{R}{R_c}\right)^{2-\gamma}\right], \tag{3.5}$$

with $\Sigma_c = 20$ g cm^{-2}, $R_c = 20$ au, and $\gamma = 0.5$; for reference, Andrews et al. (2012) uses $-1 \leq \gamma \leq 1$. Here, Σ_c is the surface density at radius R_c, and γ determines the slope of the power law part of the solution. Unfortunately, when $R \ll R_c$, this solution begins to blow up, which makes it computationally difficult to handle. We use a smooth interpolation between the self-similar solution and a flat, constant surface density profile, given by

$$\Sigma_{\rm gas}(R, t = 0) = \left(\Sigma_{\rm ss}(R)^{-p} + \Sigma_{\rm ss}(R_{\rm trans})^{-p}\right)^{-1/p} \tag{3.6}$$

as our initial condition. We take $p = 5$ and $R_{\rm trans} = 1$ au so that the transition occurs close to the interior of the domain and the transition from the self-similar to the flat profile is not too sharp.

Though we have chosen to work in one dimension, some quantities depend on the local density ρ rather than the surface density Σ. In these cases, we assume a vertical Gaussian distribution of material,

$$\rho(R, z) = \frac{\Sigma(R)}{\sqrt{2\pi} h_{\rm gas}} \exp\left[-\frac{1}{2}\left(\frac{z}{h_{\rm gas}}\right)^2\right] \tag{3.7}$$

where the scale height $h_{\rm gas} = c_s/\Omega$.

Dust dynamics

We consider two solid populations in our model: a small "dust" population with radius 0.1 µm and a "pebble" population with radius 1 mm, with mass ratios 90% and 10%, respectively. Following Birnstiel et al. (2010), we define the surface density evolution for each population by the partial differential equation

$$\frac{\partial \Sigma_{\rm solid}}{\partial t} + \frac{1}{R}\frac{\partial}{\partial R}\left(R F_{\rm tot}\right) = 0 \tag{3.8}$$

in the absence of sources and sinks, where $\Sigma_{\rm solid}$ is the solid surface density for a single population and $F_{\rm tot} \equiv F_{\rm adv} + F_{\rm diff}$ is the total flux, with contributions from an advective and diffusive part. The

fluxes are given by

$$F_{\rm adv} = \Sigma_{\rm solid} u_{\rm solid} \tag{3.9}$$

and

$$F_{\rm diff} = -\frac{\nu}{{\rm St}^2 + 1} \frac{\partial}{\partial R} \left(\frac{\Sigma_{\rm solid}}{\Sigma_{\rm gas}} \right) \Sigma_{\rm gas}. \tag{3.10}$$

In the above equations, the Stokes number is given by

$${\rm St} = \frac{\pi}{2} \frac{a_{\rm gr} \rho_{\rm gr}}{\Sigma_{\rm gas}} \tag{3.11}$$

in the Epstein regime, with $a_{\rm gr}$ the radius of a single (pebble or dust) grain and $\rho_{\rm gr}$ the density of the solid material (i.e., silicate). The radial velocity of the solids is given by

$$u_{\rm solid} = \frac{u_{\rm gas}}{{\rm St}^2 + 1} - \frac{2 u_{\rm grad}}{{\rm St} + {\rm St}^{-1}} \tag{3.12}$$

where

$$u_{\rm gas} = -\frac{3}{R^{1/2} \Sigma_{\rm gas}} \frac{\partial}{\partial R} \left(R^{1/2} \nu \Sigma_{\rm gas} \right) \tag{3.13}$$

is the gas velocity and

$$u_{\rm grad} = -\frac{E_d}{2 \rho_{\rm gas} \Omega} \frac{\partial p_{\rm gas}}{\partial R} \tag{3.14}$$

is the velocity due to the gas pressure gradient. E_d is a drift efficiency parameter and $p_{\rm gas} = \rho_{\rm gas} c_s^2$ is the gas pressure. Birnstiel et al. (2010) gives more detail on these equations.

Again, we must make some assumption about the vertical distribution of solids to determine $\rho_{\rm solid}$. We make the same vertical Gaussian assumption as for the gas, but, to simulate settling, we allow the scale height of the pebbles to be a fraction $\xi_{\rm pebbles}$ of the gas scale height, so $h_{\rm pebbles} = \xi_{\rm pebbles} h_{\rm gas}$. We use $\xi_{\rm dust} = 1$ such that the dust is not settled. For the pebbles, we take $\xi_{\rm pebbles} = 0.1$.

Adsorption and desorption

Finally, adsorption, the process by which atoms and molecules stick to a solid surface, and desorption, in which the atoms and molecules leave the surface, must be included as source terms. Hollen-

bach et al. (2009) gives the adsorption timescale as

$$\tau_{\rm ads} = \left(n_{\rm solid}\sigma_{\rm gr}v_{\rm therm}\right)^{-1} \tag{3.15}$$

where $n_{\rm solid}$ is the local number density of solids, $\sigma_{\rm gr} = \pi a_{\rm gr}^2$ is the cross-sectional area of a single grain, and $v_{\rm therm} = \sqrt{8k_BT/\pi m}$ is the thermal velocity of the atom or molecule of interest. Inverting the timescale, we find the adsorption rate

$$R_{\rm ads} = n_{\rm solid}\sigma_{\rm gr}v_{\rm therm} \tag{3.16}$$

per atom or molecule.

For desorption, Hollenbach et al. (2009) gives the rate per molecule of ice

$$R_{\rm des} = \nu_{\rm att}\exp\left(-\frac{T_{\rm bind}}{T}\right), \tag{3.17}$$

where $\nu_{\rm att}$ is the attempt frequency — the vibrational frequency of the atoms and molecules on the surface — of order 10^{12} s^{-1}, and $T_{\rm bind}$ is the binding energy of the species of interest (4800 K for H_2O and 960 K for CO, Aikawa et al. 1996).

Combining Equations 3.16 and 3.17, we find the volumetric source terms

$$s_{\rm gas} = R_{\rm des}n_{\rm solid} - R_{\rm ads}n_{\rm gas}. \tag{3.18}$$

To find the appropriate source term for the surface density equations above, we must integrate $s_{\rm gas}$ vertically and multiply by the species' mass m. We find

$$S_{\rm ads} = \frac{\sigma_{\rm gr}v_{\rm therm}\Sigma_{\rm gas}\Sigma_{\rm solid}}{\sqrt{2\pi}m_{\rm gr}h_{\rm gas}\sqrt{1+\xi_{\rm solid}^2}}. \tag{3.19}$$

and

$$S_{\rm des} = m\int_{-\infty}^{\infty} R_{\rm des}n_{\rm solid}\,{\rm d}z = R_{\rm des}\Sigma_{\rm solid}. \tag{3.20}$$

(Equation 3.19 is derived in Appendix 3.7.) These source terms both have units of g cm^{-2} s^{-1} and represent the rates at which the surface density changes due to adsorption and desorption processes, respectively.

Thus, the source terms for surface density equations are given by

$$S_{\rm gas} = S_{\rm des} - S_{\rm ads} \tag{3.21}$$

and

$$S_{\rm solid} = S_{\rm ads} - S_{\rm des}. \tag{3.22}$$

These source terms encode the rate at which the surface densities of gas and solid species are changing due to the adsorption and desorption chemistry in our model.

Temperature structure

The temperature field presents a challenge by itself. Temperature appears in Equation 3.1 through the viscosity term, and so it contributes to the gas dynamics. Yet the gas dynamics play a role in determining the dust dynamics, which, through radiative transfer from the central star, determine the temperature. In addition, the intrinsic luminosity of the star is expected to change significantly over the timescales presented here (Siess et al., 2000). One way to solve this circular problem is through iteration, as in Price et al. (2020). However, that procedure would be more computationally costly when coupled to the code we have described here.

Instead of seeking a self-consistent solution, as in Price et al. (2020), we follow a simpler procedure to capture the approximate temperature structure. Noting that the bulk surface density, and therefore dust grain surface density, does not change significantly over time, we use RADMC-3D version 0.41 (Dullemond et al., 2012) to compute a temperature structure with a self-similar dust initial condition (i.e., same form as Equation 3.5), assuming a dust-to-gas ratio of 0.01 and using the interpolated DSHARP opacities (Birnstiel et al., 2018). We note that this procedure is an approximation, since we are not taking into account the evolving dust and pebble surface density, but it provides sufficient accuracy for our proof-of-concept purposes.

Next, we fit a power law $T \propto R^{-\beta}$ to the output from RADMC-3D, limited to the region between 2 au and 20 au to avoid edge effects and unphysical behavior far from the star. Though we run RADMC-3D with two dust populations, the temperatures are virtually equal, so we assume

a power law slope of -0.41 and appropriate intercept parameter, which reasonably captures the behavior of both populations, and use that same power law for both when solving the differential equations.

To take into account a changing stellar luminosity over time, we use the Siess et al. (2000) web server to compute stellar radii $R_\star$ and effective temperatures $T_{\rm eff}$ over the lifetime of the disk. Then, inspired by Chiang & Goldreich (1997), Equation 12, we see that the disk temperature scales by a factor $f \propto R_\star^{1/2} T_\star$. We compute this factor from the isochrons and scale it by the initial value such that $f \leq 1$ at all times, i.e., the disk temperature is decreasing over time, primarily due to radial contraction decreasing the bolometric luminosity of the central star.

Finally, we perform a fit to the two regimes we observe in f — a flat, early-time regime and a sloped, late-time regime — and join the two regimes by smooth interpolation. This interpolation takes the same form as Equation 3.6, but with a parameter $p = 100$ that is more appropriate for this data. See Figure 3.1 for the parameters in each regime and the final interpolation. Figure 3.2 shows the resulting temperature that is used in the fiducial model alongside two fixed-temperature models representing the beginning and end state.

Solution procedure

To solve Equations 3.1 and 3.8 with source terms given by Equations 3.21 and 3.22, we require approximations of first and second derivatives in radius. We use a logarithmically-spaced mesh in R and second-order accurate finite difference derivatives estimated with Equations 3.26 and 3.27. Where appropriate, we switch to first-order accurate upwind finite difference derivatives.

To advance the solution in time, we use the backward differentiation formula (BDF) implementation in the Portable, Extensible Toolkit for Scientific Computation (PETSc) (Balay et al., 1997, 2019, 2018) time stepping (TS) (Abhyankar et al., 2018) module. We use the PETSc internal colored finite difference Jacobian and solve the resulting linear system with the MUltifrontal Massively Parallel sparse direct Solver (MUMPS) (Amestoy et al., 2001b, 2019).

The system of partial differential equations we finally solve is in nine quantities. The bulk gas,

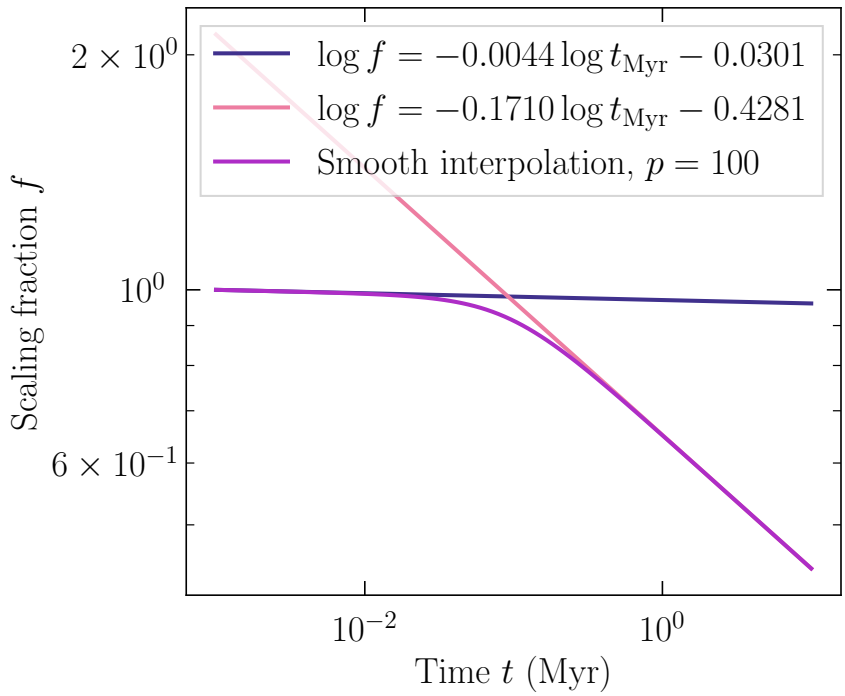

Figure 3.1: Temperature scaling fraction as determined by fitting Siess et al. (2000) isochrons with two power laws and then interpolating smoothly between them. The complete procedure is described in Section 3.3. The parameters of the lines are given in the legend, and the interpolation "power" p is chosen to give a smooth curve to the intersection of the lines.

pebble, and dust densities are treated according to Equations 3.1 and 3.8 with no source terms. Then, we consider H_2O and CO in gas, as ice on pebbles, and as ice on dust grains by adding the appropriate source term to the right-hand sides of Equations 3.1 and 3.8. We evolve the equations to 1 Myr on the spatial domain [0.5 au, 500 au].

3.4 Results

Fiducial model

In Figure 3.3 (first column), we show the behavior of the bulk gas, pebbles, and dust over time and radius in the fiducial model. While the gas behavior shows simple viscous spreading, the pebbles and dust show more interesting behavior. The 1 mm pebbles form a shallow gap-like structure at

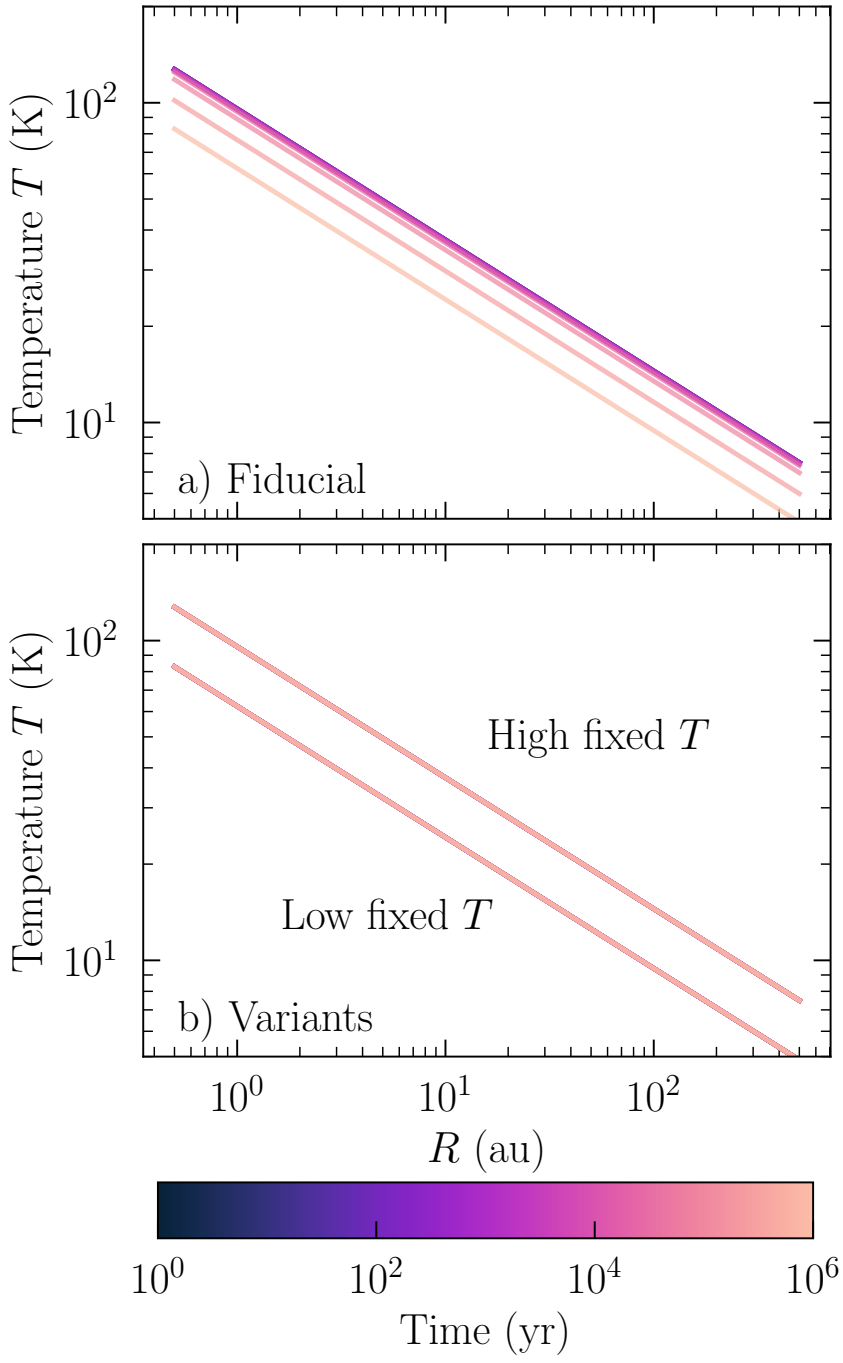

Figure 3.2: In panel (a), we show the temporal and spatial evolution of the disk temperature (assumed vertically invariant for the purposes of the model) for the fiducial case. In panel (b), we show the two variants explored: a high temperature case (upper) and low temperature case (lower), both of which are held fixed in time. The line color in all panels indicates logarithmically-increasing time.

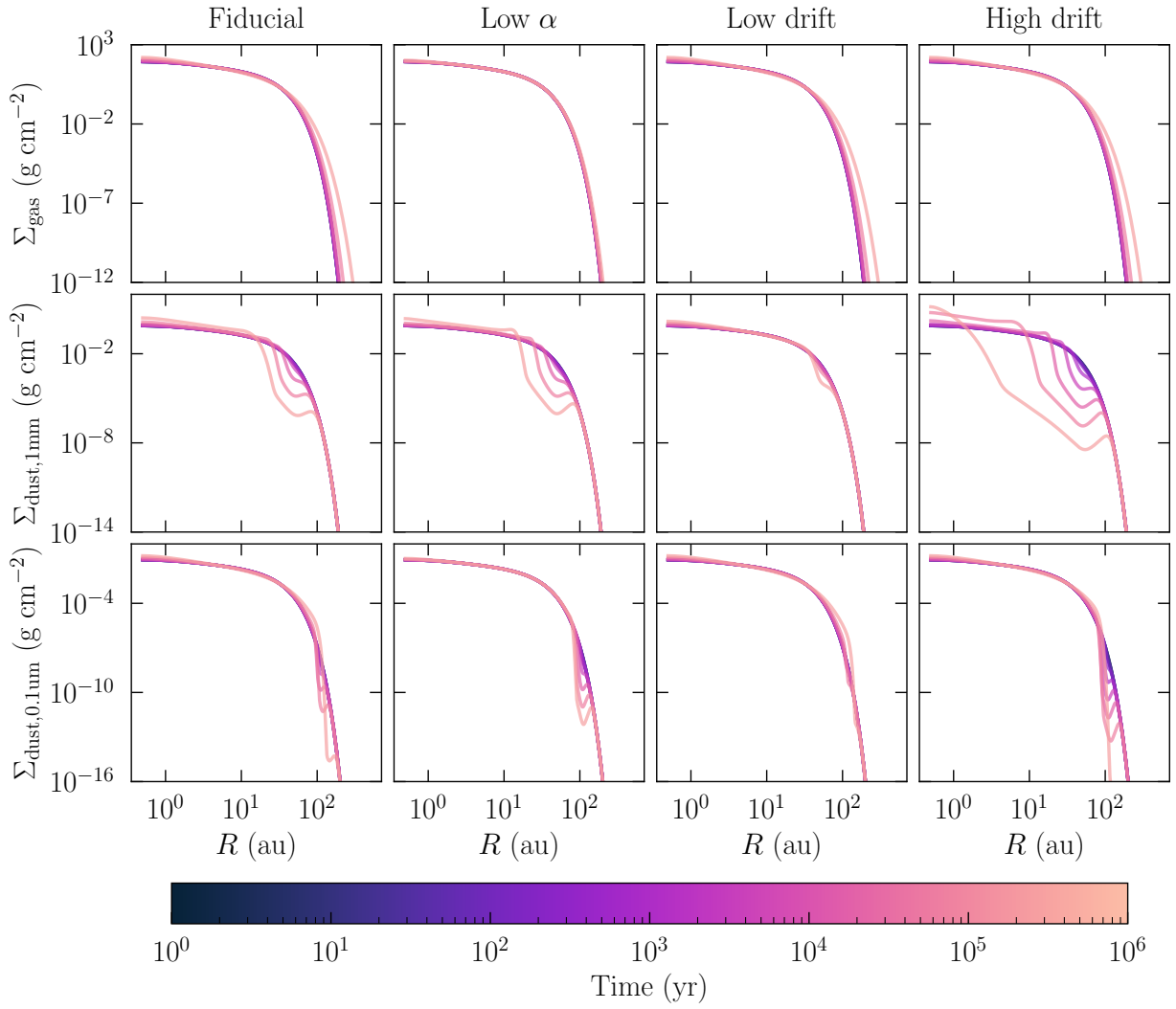

Figure 3.3: Temporal and spatial evolution of the three bulk surface densities for four selected model cases. The rows represent the surface densities of each type (gas, 1 mm pebbles, and 1 µm dust, from top to bottom, respectively) while the columns represent the different models. Temporal evolution is shown by the color gradient, which extends through time on a logarithmic scale from darker to lighter colors. The most notable feature is the development of a density deficit in the solids around 100 au caused by drift; this is observed in both pebbles and dust, but the pebbles exhibit a stronger effect because they drift more efficiently than the dust, which is well-coupled to the gas.

Identifier	Viscosity parameter α	Drift efficiency E_d	Initial CO/H_2O	Temperature model
Fiducial	10^{-3}	0.1	20%	time-evolving
Low α	10^{-4}	0.1	20%	time-evolving
Low drift	10^{-3}	0.01	20%	time-evolving
High drift	10^{-3}	0.9	20%	time-evolving
Low CO	10^{-3}	0.1	1%	time-evolving
High CO	10^{-3}	0.1	100%	time-evolving
Low fixed T	10^{-3}	0.1	20%	static, $t = 1$ Myr
High fixed T	10^{-3}	0.1	20%	static, $t = 0$ Myr

Table 3.1: Various model cases and parameter values.

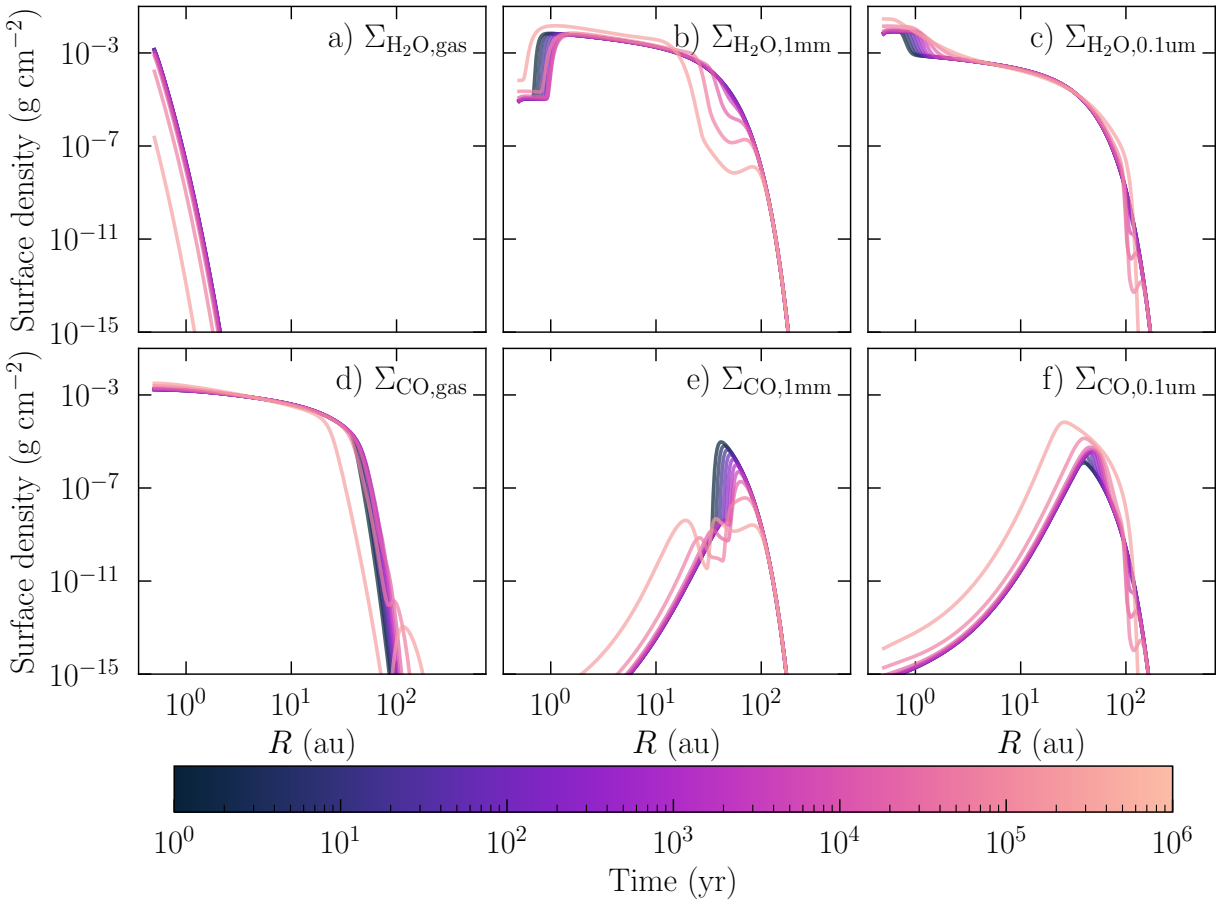

Figure 3.4: Fiducial model evolution of the surface densities of H_2O (top row) and CO (bottom row) in the gas phase (left column) and solid phases (middle and right column). The pebble deficit from Figure 3.3 is echoed in the water ice, but the CO experiences a very different behavior than the bulk solids.

about 30–100 au. This position coincides with the radius where the Stokes number goes to unity, and thus where the pebbles move fastest. As a result, at smaller radii, the pebbles move inward, and, at larger radii, the pebbles move outward, resulting in a pebble deficit at about 100 au. The 0.1 µm dust forms a similar structure at larger radii.

Figure 3.4 shows that the ice-coated solids do not universally follow the same trends as the bulk. While H_2O on pebbles and dust forms the gap-like structure near 100 au, there is a second pebble and dust deficit at 1 au, the H_2O snowline, where there is also a rapid increase in H_2O vapor surface density. The behavior of CO is significantly different from that of H_2O. The gap at 30–100 au is much shallower, and only clearly visible at late times. Analogous to H_2O, there is a rapid drop in CO dust and pebble surface density at the CO snowline. Figure 3.4 already shows a clear change in the CO/H_2O surface density ratio in the outer disk.

In Figure 3.5, we present the main results of this paper both for the fiducial model and for a small parameter study (see next section). Each panel in the figure shows the evolution of the CO/H_2O ratio in two ways: On the left, we show the variation over time and space on the vertical and horizontal axes, respectively. On the right, in a smaller panel, we integrate over radius in the region shown and show the evolution of the ice mass — total and where $CO/H_2O \geq 1$ — over time. In Figure 3.5a, we show the predicted ratio of CO/H_2O for our fiducial model, and we find that a maximum ratio near unity is achieved by 1 Myr in the region between about 20 and 200 au, and that this feature takes the shape of a funnel when observed in the space-time plane. This enhanced material accounts for an average of 40% of the disk mass. See Table 3.2 for similar measurements of each model case that follows.

Parameter study

While our fiducial model results are encouraging in explaining anomalous, CO-enhanced comets, we also seek to understand the robustness of this result to changes in disk parameters, relatively unconstrained by observations or detailed simulations. The first parameters of interest are the viscosity parameter and drift efficiency. The viscosity parameter α ultimately sets the diffusion

coefficient, which directly controls the gas's diffusion and the diffusive flux of the solids. Figure 3.3 (second column) shows that reducing this parameter only has some minor effects on the dust and pebble evolution. The drift efficiency E_d influences the coupling of solids to gas but only appears in the dust velocity, and therefore leaves gas motion unchanged. Figure 3.3 (third and fourth columns) show that increasing and decreasing this parameter dramatically changes the drift and therefore depletion of solids in the outer disk regions.

Figure 3.5b shows the enhancement of the CO/H_2O ratio in ice for a model with α reduced by a factor of ten compared to the fiducial model. Reducing α makes the viscosity smaller everywhere, which, in turn, amounts to making the diffusion coefficient smaller. Thus, we would expect that disk material would experience less viscous spreading in this case, and, indeed, we see that the characteristic "funnel" shape of the CO-enhanced region in time and space is truncated and does not reach 100 au, while drift still carries material inward towards the star. The amount of CO-enhanced ice is modest, but it is certainly present.

In Figures 3.5c and 3.5d, we show the enhancement of the CO/H_2O ratio in ice for the low and high drift models, respectively; for these test cases, we fixed E_d at 0.01 and 0.9, changing the efficiency of the coupling to the gas pressure derivative. The models achieve about the same maximum CO/H_2O ratio, but with very different fractions of CO-enhanced ice; i.e., the low-drift enhancement feature is visibly smaller in the space-time plane. We immediately see, then, that the efficiency of the radial drift of pebbles and dust is very important for predicting the amount of mass available for making comets like 2I/Borisov and C/2016 R2 (PanSTARRS). We return to this in the discussion section.

The third parameter of interest is the initial CO/H_2O ratio. We test two possibilities in addition to the fiducial model: A high CO/H_2O value of 100% and a low CO/H_2O value of 1%. We choose these end-member cases because, while typical comets have CO/H_2O of about 4% (Bockelée-Morvan & Biver, 2017), they may have 1% or less (Mumma & Charnley, 2011), while the interstellar medium has up to 100% with a large errorbar (Öberg, 2016). Note that the amount of CO has no effect on the bulk dynamics; it only affects the chemical evolution of the disk. In Figures 3.5e and

3.5f, we show the chemical evolution of the disk in these two cases. We find that the low CO model is not able to reach a CO/H_2O ratio of unity; see Figure 3.5e. On the other hand, the high CO model easily reaches values of $CO/H_2O \gtrsim 10$ by about 1 Myr, as shown in Figure 3.5f, and this material accounts for a large fraction of the total disk mass.

The effect of a static, low temperature profile and a static, high temperature profile on our disk model is shown in Figures 3.5g and 3.5h, respectively. For these cases, we artificially fixed the temperature at its final or initial value, as appropriate (recall that the temperature strictly decreases with time, and see Figure 3.2 for the radially-dependent structures we adopted). These models reach roughly the same level of CO/H_2O ice enhancement, but the radii where the enhancement occurs are shifted. In the low temperature model, the onset of the enhancement is delayed in time. The high temperature model's enhanced region is shifted to larger radii because the disk is warmer everywhere, and so ice will desorb off the grains in this model farther out than in the fiducial model. Most importantly, the details of the temperature structure and evolution are not critical for the formation of a substantial amount of CO ice; both static temperature models achieve at least 30% CO-enhanced ice (see Table 3.2).

Finally, we summarize our results numerically in Table 3.2 in terms of maximum CO/H_2O ratio, total number of CO-enhanced Halley-mass comets, and the mass fraction of the ice in the disk that is CO-enhanced by the end of the simulation. Most models achieve a CO/H_2O ratio above unity (only the low CO model achieves a lower maximum ratio). The lowest ratio (low initial CO model) is just over 0.1, and the largest ratio (high initial CO model) is greater than 10, revealing a monotonic dependence on CO initial abundances. The low drift model produces the next-least amount of CO-enhanced ice. The fraction of ice in the region [5 au, 200 au] that is CO-enhanced is, on average, about 40%, but in the high-drift model it is all of 87%, indicating that most water ice has been lost from the system due to pebble drift. The maximum number of CO-enhanced Halley-like comets that could be formed in the disks is between 10^8 and 10^{10}, though this assumes a formation efficiency of 100% from the dust and pebbles and no additional mixing, trapping, or drift. While a large range of values are possible, we emphasize that there is almost always a region where there is

Identifier	Highest CO/H_2O ratio	Total CO-enhanced Halley-mass comets	Fraction of CO-enhanced ice
Fiducial	2.39	6×10^9	48%
Low α	2.43	6×10^9	36%
Low drift	2.21	2×10^8	6%
High drift	2.56	6×10^9	87%
Low CO	0.12	–	0%
High CO	11.93	2×10^9	78%
Low fixed T	3.47	6×10^9	35%
High fixed T	2.96	2×10^8	30%

Table 3.2: Model outcomes. Masses are measured over the same region shown in Figure 3.5. We define CO-enhanced as ice with $\Sigma_{CO} \geq \Sigma_{H_2O}$.

some CO ice enhancement relative to H_2O ice.

3.5 Discussion

We have explored the role of dust drift in changing the local ice composition in a protoplanetary disk midplane. Using models that assume simple ices composed of CO and H_2O and allowing for adsorption and desorption, we find that parameters controlling the dynamics, such as the drift efficiency and viscosity, as well as the temperature (which affects dynamics indirectly), all play an important role in determining the specific amount of CO enhancement relative to H_2O as well as the distribution of ices by 1 Myr. Yet, across our models, there is consistently a region of our disk that displays CO/H_2O ice enhancement compared to the initial CO/H_2O abundance ratio, independent of the choice of parameters, in all cases we have explored.

Why does this enhancement occur? Most of the water in our model is in the form of ice. Drift carries the water ice-laden pebbles and dust inward, creating an ice deficit. We can see from Figure 3.4 that the water ice deficit forms around 100 au and spreads out in time. Meanwhile, even though we start with CO as ice, interior to its snowline, it initially sublimates quickly. The gas-phase CO crosses the snowline as it viscously spreads out. This "new" CO enters the water ice deficit region and then freezes out onto whatever solids remain. In Figure 3.4c and 3.4f, we see that, while the amount of CO on pebbles decreases over time, the amount of CO on dust increases. The radial

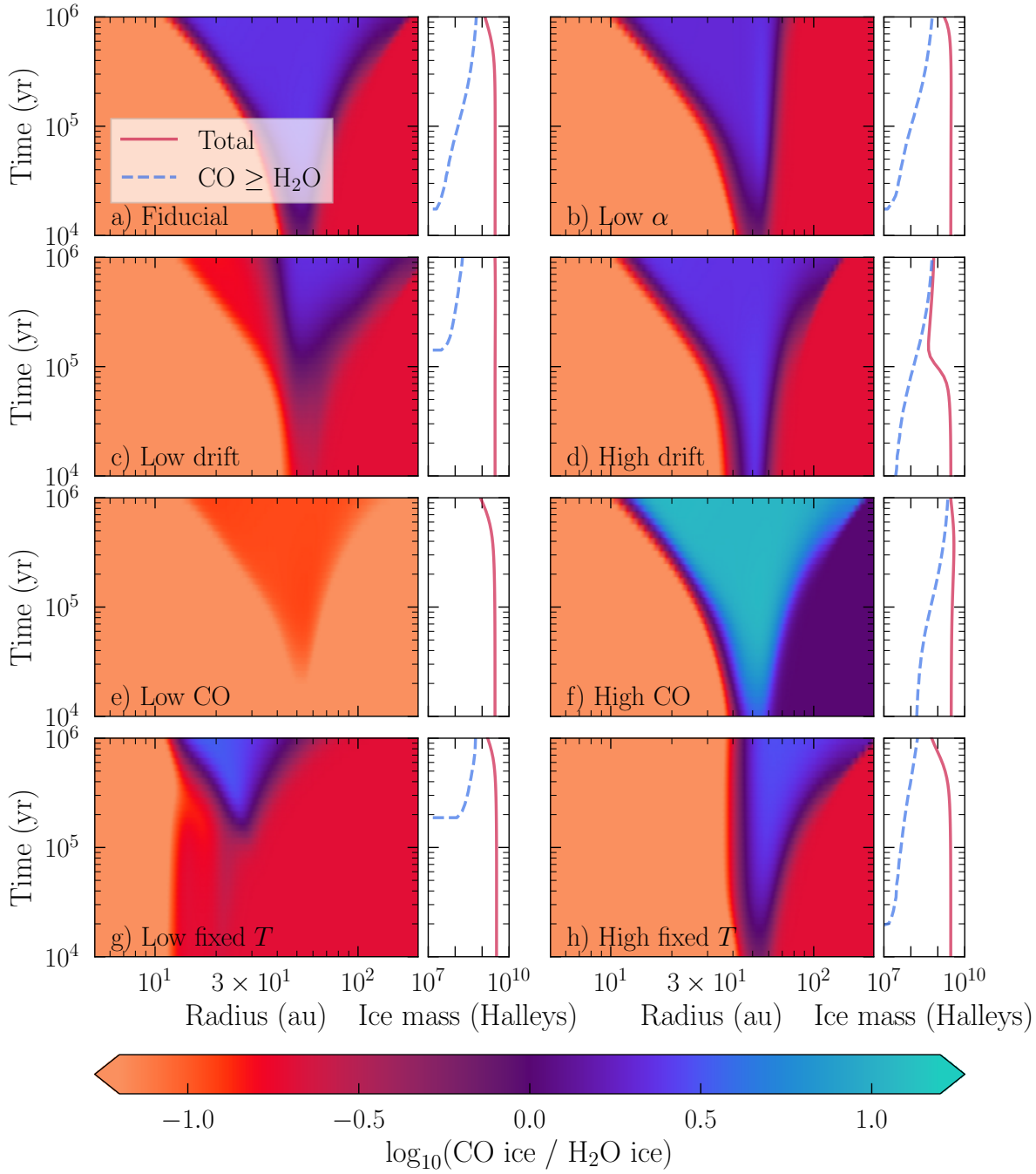

Figure 3.5: Evolution of the CO/H_2O ice ratio as a function of time and space in the disk model. Each large panel represents a different set of conditions or parameters used, which can be found listed in Table 3.1. In each large panel, the two smaller panels show the evolution of the ice ratio (left, two-dimensional color plot) and the total mass in enhanced ice over time (right, line plot). In the line plot, the ice mass is measured in units of Halley's comet's mass, to give the reader an idea of how many comets could be formed from the material if formation was 100% efficient.

process we have described is similar to the "vertical cold finger effect" described by Meijerink et al. (2009), where water is depleted in the upper disk layers because of diffusive transport and settling. In addition, this work is consistent with the results of Ros & Johansen (2013), which found significant solid enhancement caused by transport across the radial snowline. This work demonstrates that there is likely to be a complex interplay with the evolution of solids and the chemical composition of the ice mantles they harbor. Future work should explore these connections with more advanced chemistry along with ice chemistry and/or isotopic chemistry, to fully understand the relationship between grain drift, viscous spreading across snowlines, and the resulting chemistry.

While we have limited ourselves in this paper to only two grain sizes, a more realistic simulation would use a continuous distribution of grain sizes. We expect that the largest grain size is the driving factor of the location of the inner edge of the enhancement feature. When the largest size is reduced from 1 mm, the largest size we considered here, drift becomes less efficient; when it is increased, drift becomes more efficient. Drift greatly influences the location of the inner edge of the "funnel" we observe in the models we present here. Since the mechanism proposed above only needs some small grain population to be entrained with the gas and some large population that drifts efficiently, we theorize that the exact distribution of grain sizes does not strongly influence our results.

3.6 Conclusions

We present models of the surface density evolution of a viscously-evolving protoplanetary disk, including the effect of grain drift, with the goal of explaining the observations of CO-enriched comets. To explore how midplane CO and H_2O abundances in gas and ice evolve within this dynamic framework, we include simple adsorption and desorption chemistry to capture the interplay of dust transport and snowlines. We find that most of our disk models readily produce a region where CO ice is more abundant than H_2O ice. These results indicate that forming CO-enriched comets may not be so unusual.

On the other hand, the fact remains that we have not observed very many CO-enriched comets

to date. Assuming our Solar System originated with a nominal amount of CO, there may be some selection bias that causes CO-poor comets to be observed more frequently.

Fitzsimmons et al. (2019) and Xing et al. (2020) conclude that the extrasolar comet 2I/Borisov is in most ways — excluding its high CO/H_2O ratio — similar to Solar System comets. Our results support the conclusion that the CO/H_2O ice enhancement commonly occurs in the outer disk for solar-type stars, between 20 and 100 au. Perhaps comets that form so far out are more easily ejected due to being weakly gravitationally bound to their host star. 2I/Borisov may be an example of this mechanism at work. While dynamical simulations are beyond the scope of the present work, it would be interesting to compare the expected distribution of formation locations of extrasolar comets pre-ejection with the chemical patterns found here, to further test this hypothesis.

E.M.P. gratefully acknowledges support from National Science Foundation Graduate Research Fellowship Program (GRFP) grants DGE1144152 and DGE1745303 and helpful conversations with Prof. Zhaohuan Zhu and Prof. Paul C. Duffell. This work was supported by an award from the Simons Foundation (SCOL # 321183, KO). L.I.C. gratefully acknowledges support from the David and Lucille Packard Foundation, the VSGC New Investigators Award, the Johnson & Johnson WiSTEM2D Award, and NSF AST-1910106.

This work was inspired by conversations at the May 2019 "ExoComets: Understanding the Composition of Planetary Building Blocks" workshop, and we are grateful for the Lorentz Center's support of this event.

3.7 Supplementary equations

Vertically-integrated source term

Since the evolution equations given in this paper are in terms of surface density, which is a vertically-integrated quantity, it is important to additionally vertically integrate the usual adsorption source

term, as

$$S_{\rm ads} = m \int_{-\infty}^{\infty} R_{\rm ads} n_{\rm gas}\, {\rm d}z \tag{3.23}$$

$$= \sigma_{\rm gr} v_{\rm therm} \int_{-\infty}^{\infty} \frac{\Sigma_{\rm dust}}{\sqrt{2\pi} h_{\rm dust} m_{\rm gr}} \exp\left[-\frac{1}{2}\left(\frac{z}{h_{\rm dust}}\right)^2\right] \frac{\Sigma_{\rm gas}}{\sqrt{2\pi} h_{\rm gas}} \exp\left[-\frac{1}{2}\left(\frac{z}{h_{\rm gas}}\right)^2\right] {\rm d}z \tag{3.24}$$

$$= \frac{\sigma_{\rm gr} v_{\rm therm} \Sigma_{\rm gas} \Sigma_{\rm dust}}{\sqrt{2\pi} m_{\rm gr} h_{\rm gas} \sqrt{1+\xi_{\rm dust}^2}}. \tag{3.25}$$

Note that we would have missed an important correction factor had we naïvely multiplied $n_{\rm gas}$ and $n_{\rm dust}$ without taking into account the vertical integration.

Finite difference approximations

On a finite grid in x with points $\{x_i\}$, we use the modified finite difference formulae

$$\frac{\partial f}{\partial x} \approx \left(\frac{-h_{i+1}}{h_{i-1}\left(h_{i-1}+h_{i+1}\right)}\right) f_{i-1} + \left(\frac{1}{h_{i-1}} - \frac{1}{h_{i+1}}\right) f_i + \left(\frac{h_{i-1}}{h_{i+1}\left(h_{i-1}+h_{i+1}\right)}\right) f_{i+1} \tag{3.26}$$

and

$$\frac{\partial^2 f}{\partial x^2} \approx \left(\frac{2}{h_{i-1}\left(h_{i-1}+h_{i+1}\right)}\right) f_{i-1} + \left(\frac{-2}{h_{i-1}h_{i+1}}\right) f_i + \left(\frac{2}{h_{i+1}\left(h_{i-1}+h_{i+1}\right)}\right) f_{i+1}, \tag{3.27}$$

where $h_{i-1} = x_i - x_{i-1}$ and $h_{i+1} = x_{i+1} - x_i$, and $\{f_i\}$ are samples of a smooth function $f(x)$. These formulae are general and second-order accurate, and they apply to any irregularly-spaced grid.

Chapter 4

Tidally-Distorted, Iron-Enhanced Exoplanets Closely Orbiting Their Stars

This chapter originally appeared in the literature as:

Price, E. M., & Rogers, L. A. 2020, ApJ, 894, 8, doi: 10.3847/1538-4357/ab7c67

©AAS. Reproduced with permission.

4.1 Abstract

The transiting planet candidate KOI 1843.03 (0.6 $R_\oplus$ radius, 4.245 hour orbital period, 0.46 $M_\odot$ host star) has the shortest orbital period of any planet yet discovered. Here we show, using the first three-dimensional interior structure simulations of ultra-short-period tidally distorted rocky exoplanets, that KOI 1843.03 may be shaped like an American football, elongated along the planet-star axis with an aspect ratio of up to 1.79. Furthermore, for KOI 1843.03 to have avoided tidal disruption (wherein the planet is pulled apart by the tidal gravity of its host star) on such a close-in orbit, KOI 1843.03 must be as iron-rich as Mercury (about 66% by mass iron compared to Mercury's 70% by mass iron, Hauck et al. 2013). Of the ultra-short-period ($P_{\rm orb} \lesssim 1$ day) planets with physically-meaningful constraints on their densities characterized to date, just under half (4 out

of 9) are iron-enhanced. As more are discovered, we will better understand the diversity of rocky planet compositions and the variety of processes that lead to planetary iron enhancement.

4.2 Introduction

The compositions of rocky planets reflect a combination of the compositions of their host star, the condensation sequence that concentrates elements heavier than hydrogen and helium into solids, and processing during planet formation and subsequent evolution. To leading order, the Earth is comprised of an iron-dominated core (32% by mass) and silicate mantle (68% by mass), with roughly the same relative elemental abundances as in the solar photosphere (Lineweaver & Robles, 2009). Most rocky exoplanets with measured masses and radii also follow this trend and are consistent with Earth's composition with some scatter (Dressing et al., 2015). In contrast, Mercury, at 70% by mass iron (Hauck et al., 2013), is significantly enhanced in iron relative to solar abundances.

For planets on very short orbital periods ($\lesssim$ 1 day), tides can be used to constrain the planets' bulk densities and compositions. Planets in orbit around a star will experience a tidal force, as the day side of the planet feels a stronger attractive gravitational force than the night side. Planets, by the IAU definition[1] (Boss et al., 2007), are sufficiently massive for their self-gravity to overcome their rigid body forces and to achieve hydrostatic equilibrium shapes. As a result, a tidal field causes an orbiting planet to become elongated in the direction of the planet-star axis (e.g., de Pater & Lissauer, 2010). If the tidal forces are too strong (the planet is too close to its star), the planet may be tidally disrupted and pulled apart, thus becoming a ring around the host. The minimum distance at which a fluid planet can avoid tidal disruption is called the Roche limit. For an incompressible fluid, this limiting distance is given by

$$a \simeq 2.44 R_\star \left(\frac{\rho_\star}{\rho_p}\right)^{1/3} \tag{4.1}$$

(Roche, 1849), where a is the orbital semi-major axis, $R_\star$ is the stellar radius, $\rho_\star$ is the stellar density, and ρ_p is the planet density. Following Rappaport et al. (2013), we can rewrite Equation 4.1

[1] https://www.iau.org/static/resolutions/Resolution_GA26-5-6.pdf

using Kepler's third law to express a in terms of the orbital period $P_{\rm orb}$; then, the expression has no dependence on the stellar density, and we find

$$P_{\rm orb} \simeq 12.6 \text{ hr} \left(\frac{\rho_p}{1 \text{ g cm}^{-3}} \right)^{-1/2}. \tag{4.2}$$

The Roche limit is a familiar concept in the context of the rings and satellites of Saturn as well as interacting binary stars. The discovery of exoplanets that are very close (orbital period, $P_{\rm orb} < 1$ day) to their host stars — found around 0.5% of Sun-like stars (Sanchis-Ojeda et al., 2014) — open the opportunity to apply the Roche limit to Earth-mass-scale planets.

The transiting exoplanet candidate KOI 1843.03 has the shortest orbital period known to date. For KOI 1843.03 to have avoided tidal disruption on such a close-in orbit, previous estimates suggest that it must have a mean density of at least 7 g cm^{-3} (Rappaport et al., 2013). This density lower limit, however, relies upon interpolating the Roche limits of single-component polytrope models, wherein the pressure P and density ρ within the planet are related by a power-law $P \propto \rho^{\gamma}$ with constant γ. These do not accurately capture the density profiles of differentiated rocky bodies with sizes > 1000 km. A more accurate calculation of the Roche limit is needed to constrain the composition of KOI 1843.03.

In this work, we develop the first self-consistent three-dimensional models for the interior structures of tidally-distorted rocky planets on ultra-short period (USP) orbits ($P_{\rm orb} < 1$ day). We apply these models to refine calculations of the Roche limit for USP rocky planets and to explore the diversity of USP planet compositions. The paper is structured as follows: In Section 4.3 we describe the methods used. We outline the primary results in Section 4.4 and discuss in Section 4.5.

4.3 Methods

Modeling technique

Calculation of the Roche limit for generic equations of state (EOS) must rely on a numerical solution. Treating the planet as an extended body necessitates computing three forces: the gravitational

force from the star, the gravitational force that the planet exerts on itself, and the centrifugal force in the planet's rotating rest frame. The sum of all these forces influence the shape of the planet, which changes the mass distribution and, by extension, the forces on all points inside the planet. There is no simple, analytic way to capture the circular nature of this problem.

We use a relaxation method developed by Hachisu (1986a,b) to model the three-dimensional structure of USP rocky planets. Starting from an initial guess for the planet density distribution, the method iteratively adjusts the enthalpy and density distribution until a self-consistent solution is reached, within a tolerance of 1×10^{-5}. We expand the Hachisu method to include the gravitational potential of a point source star at a fixed distance from the planet. We also modify the equation of state (which describes how the density of a material varies with pressure) to more accurately capture the behavior of silicate rocks and iron, which have nonzero density at zero pressure.

We model two-layer planets consisting of a silicate mantle (enstatite upper mantle and perovskite lower mantle) surrounding an iron core. We simulated more than 280000 planet configurations over a grid of central pressures $P_{\rm max}$, core-mantle boundary pressures $P_{\rm cmb}$, and scaled star-planet orbital separations a/R_p. At each grid point, we begin by simulating a nearly spherical planet, self-consistently solving for the host star mass. We then simulate planets that are successively more distorted (elongated along the star-planet axis). Once material begins to fly off the planet, the Roche limit has been surpassed.

Coordinate system

To model a planet with an unknown shape, we define a three-dimensional coordinate system as shown in Figure 4.1, where any point may be specified by a radial coordinate $\hat{r}$, polar coordinate θ measured from the z-axis, and azimuthal coordinate ϕ in the x-y plane.

Following Hachisu (1986a,b), we establish two points, A and B, along the x- and y-axes, respectively, that lie on the surface of the planet. The simulation is conducted in scaled, dimensionless coordinates such that the distance from the origin to A is $\hat{r}_A \equiv 1$, and, similarly, the scaled distance from the origin to B is $\hat{r}_B$; we denote the corresponding dimensionful quantities as r_A and r_B.

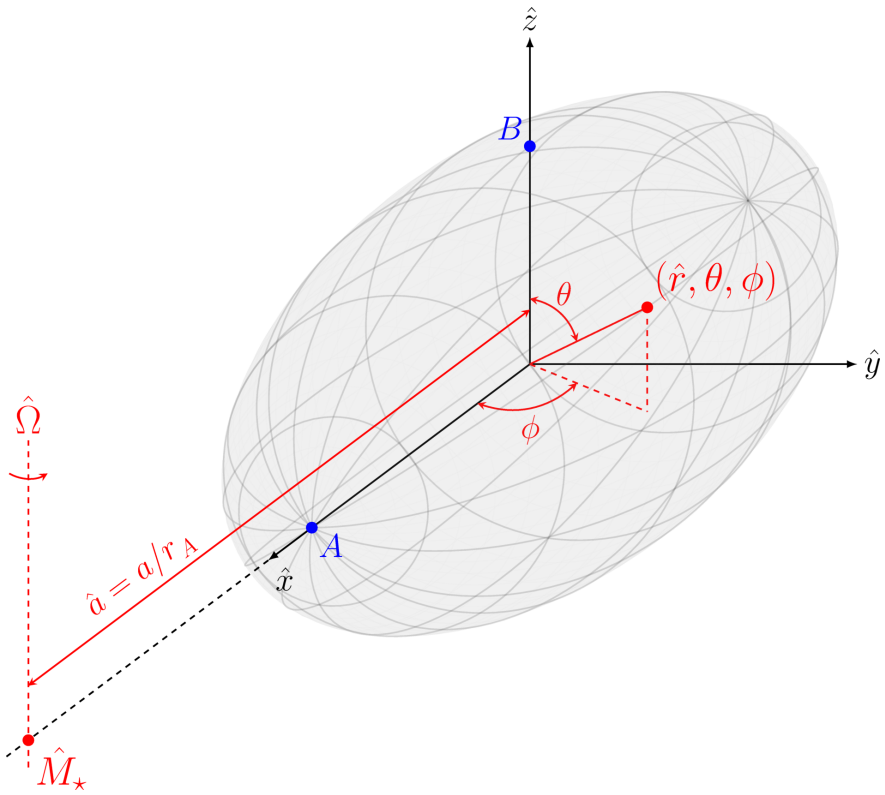

Figure 4.1: Coordinate system and geometry of the simulation space. The planet center of mass (not necessarily at the origin of the coordinate system) is positioned a distance $\hat{a}$ along the x-axis from a point-like star of mass $\hat{M}_\star$. The entire system rotates about the stellar axis with angular frequency Ω. Two points, A and B, are defined on the surface of the planet such that A lies on the x-axis at distance unity from the origin and B lies on the z-axis, quantifying the magnitude of the planet's distortion. We use the typical spherical coordinate system with polar angle θ and azimuthal angle ϕ, measured from the origin.

To approximate physical quantities that are continuous over all space, we define a grid of values of $\hat{r}$, $\mu \equiv \cos\theta$, and ϕ, sampling each quantity at every grid point; for our simulations, we use $N, P, Q = (129, 17, 33)$ divisions in $\hat{r}$, μ, and ϕ, respectively. The symmetries inherent in this system allow us to limit the simulation space to $\mu \in [0, 1]$ and $\phi \in [0, \pi]$; following Hachisu (1986a), we use $\hat{r} \in [0, 16/15]$ to ensure that the planet does not exceed the simulation volume. For a dimensionless physical quantity $\hat{X}$, we use a notation such that $\hat{X}_{i,j,k} = \hat{X}(\hat{r}_i, \mu_j, \phi_k)$.

The star is treated as a point mass on the x-axis with mass $M_\star$ at a dimensionless distance $\hat{a} = a/r_A$, where a is the radius of the planet's circular orbit, measured from the planet's center of mass to the location of the star. We do *not* make any assumptions about the coordinate of the planet's

center of mass, so it does not necessarily coincide with the origin.

The planet rotates about this axis with Keplerian angular velocity given by $\Omega^2 = G\left(M_\star + M_p\right)/a^3$. Assuming that the planet is tidally locked to the star, we may work in the rest frame of the planet, in which the star is stationary.

Relaxation method

A single iteration of the relaxation method begins with a proposal dimensionless density distribution $\hat{\rho}$. We convert the density distribution to a dimensionless enthalpy $\hat{H}$ (see Equation 4.24). Enthalpy in this context is defined as

$$H = \int \rho^{-1}\,\mathrm{d}P, \tag{4.3}$$

with ρ the density and P the pressure. Enthalpy must meet all of the boundary conditions — zero enthalpy at A and B and a dimensionless rotation rate $\hat{\Omega}$ consistent with Kepler's third law — according to

$$\hat{H}_{i,j,k} = \hat{C} - \hat{\Phi}_{i,j,k} - \hat{\Omega}^2\hat{\Psi}_{i,j,k}, \tag{4.4}$$

where $\hat{C}$ is a scalar constant. $\hat{\Phi}$ is the total dimensionless gravitational potential, including influence from both the star and the planet, and $\hat{\Omega}^2\hat{\Psi}$ is the dimensionless centrifugal potential. We then convert the new dimensionless enthalpy to a new dimensionless density distribution. Iterations of this procedure continue until a relative tolerance condition between consecutive iterations is reached. We use a relative tolerance value of $\delta = 1 \times 10^{-5}$ that must be satisfied for $\hat{H}$, $\hat{C}$, and $\hat{\Omega}^2$, such that, between iterations n and $n+1$,

$$\left|\max\left(\hat{H}_{n+1} - \hat{H}_n\right)/\max\left(\hat{H}_{n+1}\right)\right| \leq \delta, \tag{4.5}$$

$$\left|\left(\hat{\Omega}^2_{n+1} - \hat{\Omega}^2_n\right)/\hat{\Omega}^2_{n+1}\right| \leq \delta, \tag{4.6}$$

and

$$\left|\left(\hat{C}_{n+1} - \hat{C}_n\right)/\hat{C}_{n+1}\right| \leq \delta. \tag{4.7}$$

These are the same metrics employed by Hachisu (1986a).

A two-layer planet may be uniquely specified by setting the values of $P_{\rm cmb}$, $P_{\rm max}/P_{\rm cmb}$, $\hat{a}$, and $\hat{r}_{_B}$. For any set of values $\{P_{\rm cmb}, P_{\rm max}/P_{\rm cmb}, \hat{a}\}$, we begin with the largest value of $\hat{r}_{_B}$ less than 1 and an ansatz dimensionless density distribution $\hat{\rho}$ that is a uniform density ellipsoid with radii $(\hat{r}_{_A}, \hat{r}_{_B}, \hat{r}_{_B})$ in the x, y, and z directions, respectively, ensuring that the ansatz satisfies the boundary conditions. After the system converges, we reduce the value of $\hat{r}_{_B}$ to the next grid point, effectively increasing the distortion each time, and use the previous converged result as the input ansatz to the next relaxation procedure.

Potential solver

By far, the most computationally difficult and expensive component of this method is finding the gravitational potential due to the extended planet itself at every point in space,

$$\Phi_p(\mathbf{r}) = -G \int_V \frac{\rho(\mathbf{r}')}{|\mathbf{r} - \mathbf{r}'|} \, \mathrm{d}V'. \tag{4.8}$$

Since the system is symmetric in y and z, we may expand and simplify Equation 4.8 as

$$\Phi_p(r, \mu, \phi) = -4G \sum_{\ell=0}^{\infty} \sum_{\substack{m=0 \\ \ell+m \text{ even}}}^{\ell} \epsilon_m \frac{(\ell - m)!}{(\ell + m)!} P_\ell^m(\mu) \cos m\phi \times \int_0^{\infty} \mathrm{d}r' \, f_\ell(r, r') \int_0^1 \mathrm{d}\mu' \, P_\ell^m(\mu') \int_0^{\pi} \mathrm{d}\phi' \, \rho(r', \mu', \phi') \cos m\phi' \tag{4.9}$$

where P_ℓ^m are the associated Legendre polynomials,

$$f_\ell\,(r, r') = \begin{cases} r'^{\ell+2}/r^{\ell+1}, & \text{if } r' < r \\ r^\ell / r'^{\ell-1}, & \text{if } r < r' \end{cases}, \tag{4.10}$$

and

$$\epsilon_m = \begin{cases} 1, & \text{if } m = 0 \\ 2, & \text{if } m \neq 0 \end{cases}. \tag{4.11}$$

We employ Simpson's rule, following Hachisu (1986b), in the $\hat{r}$ dimension but use Gauss-Legendre

quadrature in the μ and ϕ dimensions. We develop the discrete, dimensionless equivalent of Equation 4.9,

$$\hat{\Phi}_{p;i,j,k} = -4 \sum_{\ell=0}^{\ell_{\max}} \sum_{\substack{m=0 \\ \ell+m \text{ even}}}^{\ell} \epsilon_m \left(\frac{4\pi}{2\ell+1} \right) \widetilde{P}_\ell^m(\mu_j) \cos m\phi_k \times \Lambda^{\hat{r}}_{i,\ell,m}, \tag{4.12}$$

where

$$\Lambda^{\hat{r}}_{i,\ell,m} = h_{\hat{r}} \sum_{s=0}^{N-1} S_s^N \, f_\ell(\hat{r}_i, \hat{r}_s) \, \Lambda^{\mu}_{s,\ell,m}, \tag{4.13}$$

$$\Lambda^{\mu}_{s,\ell,m} = \sum_{t=0}^{P-1} G_t^P \, \widetilde{P}_\ell^m(\mu_t) \, \Lambda^{\phi}_{s,t,m}, \tag{4.14}$$

and

$$\Lambda^{\phi}_{s,t,m} = \sum_{u=0}^{Q-1} G_u^Q \, \hat{\rho}_{s,t,u} \cos m\phi_u. \tag{4.15}$$

Here,

$$\widetilde{P}_\ell^m(\mu) = \sqrt{\frac{2\ell+1}{4\pi} \frac{(\ell-m)!}{(\ell+m)!}} P_\ell^m(\mu) \tag{4.16}$$

is the normalized associated Legendre polynomial[2]. $h_{\hat{r}}$ is the interval in the $\hat{r}$ coordinate between successive grid points. The coefficients S_i^n are the alternative composite Simpson's rule coefficients (Press et al., 1988), and the coefficients G_i^n are the fixed-order Gauss-Legendre quadrature weights[3], which depend on the integration interval. Since Gauss-Legendre quadrature is an "open" integration scheme, the endpoints of the integration interval in μ and ϕ are excluded; as a matter of computational convenience, we simply inject the endpoints with zero integration weight since they are needed to define the locations A and B. We employ the same integration scheme to compute the dimensionless mass of the planet $\hat{M}_p$ and the coordinate of its center of mass $\hat{x}_p$.

Once the planet's center of mass is computed, the coordinate of the star is easily determined by $\hat{x}_\star = \hat{x}_p + \hat{a}$. $\hat{\Psi}$ is given by

$$\hat{\Psi}_{i,j,k} = -\frac{1}{2} \varpi^2_{i,j,k} \tag{4.17}$$

[2]As computed by the function `gsl_sf_legendre_sphPlm` from the GNU Scientific Library (GSL) (Galassi et al., 2009)

[3]As computed by the function `gsl_integration_glfixed_point` from the GSL (Galassi et al., 2009)

where $\varpi_{i,j,k}$ is the distance from the point to the rotation axis; in our case,

$$\hat{\Psi}_{i,j,k} = -\frac{1}{2}\left((\hat{x}_{i,j,k} - \hat{x}_{\rm cm})^2 + \hat{y}_{i,j,k}^2\right) \tag{4.18}$$

where

$$\hat{x}_{\rm cm} = \frac{\hat{M}_p \hat{x}_p + \hat{M}_\star \hat{x}_\star}{\hat{M}_p + \hat{M}_\star} \tag{4.19}$$

is the coordinate of the center of mass of the *entire* system. The total gravitational potential $\hat{\Phi}$ is given by

$$\hat{\Phi}_{i,j,k} = \hat{\Phi}_{p;i,j,k} + \hat{\Phi}_{\star;i,j,k} \tag{4.20}$$

where

$$\hat{\Phi}_{\star;i,j,k} = \frac{-\hat{M}_\star}{\sqrt{(\hat{x}_{i,j,k} - \hat{x}_\star)^2 + \hat{y}_{i,j,k}^2 + \hat{z}_{i,j,k}^2}}. \tag{4.21}$$

However, at this point, the mass of the star is an unknown. We solve the system of equations that gives the mass consistent with the boundary conditions on the enthalpy and the dimensionless form of Kepler's third law, $\hat{\Omega}^2 = \left(\hat{M}_\star + \hat{M}_p\right)/\hat{a}^3$. Then,

$$\hat{\Omega}^2 = -\left(\hat{\Phi}|_A - \hat{\Phi}|_B\right) / \left(\hat{\Psi}|_A - \hat{\Psi}|_B\right) \tag{4.22}$$

and

$$\hat{C} = \hat{\Phi}|_A + \hat{\Omega}^2 \hat{\Psi}|_A. \tag{4.23}$$

Equation 4.4 then gives the enthalpy at every point.

We follow (Hachisu, 1986a) by defining a dimensionless enthalpy $\hat{H}$ and its maximum $\hat{H}_{\rm max}$, where

$$\hat{H} \equiv H/Gr_A^2\rho_{\rm max}. \tag{4.24}$$

$\rho_{\rm max}$ is fixed in the simulation because it can be determined directly from $P_{\rm max}$ and the equation of state. To generate the non-analytic function that maps dimensionless enthalpy to dimensionless density, we finely sample the pressure P from 0 to $P_{\rm max}$ and calculate the density at each pressure with our equation of state. Equation 4.3 gives the enthalpy H at each pressure, and $H_{\rm max}$ is just the maximum of these values. Letting $\hat{\rho} \equiv \rho/\rho_{\rm max}$, we linearly interpolate $\hat{\rho}$ as a function of $H/H_{\rm max}$ and obtain a function which maps scaled, dimensionless enthalpy $\hat{H}/\hat{H}_{\rm max}$ to dimensionless density $\hat{\rho}$.

Equation of state

Previous work modelling distorted stars by Hachisu (1986a) assumes a polytropic equation of state,

$$\rho(P) = cP^n, \tag{4.25}$$

where ρ is density and P is pressure. This equation of state is not appropriate for a rocky planet because it does not allow for nonzero density at zero pressure. In this work, we consider only planets with two layers: an iron core and a silicate mantle; our method may be extended to planets with different compositions and any number of layers, however.

At low pressures ($P \leq P_{\rm trans} = 23 \times 10^9$ Pa), we apply the Birch-Murnagham equation of state (BME) for enstatite (Seager et al., 2007). For $\eta \equiv \rho/\rho_{0,\rm en}$, we have (Seager et al., 2007),

$$P_{\rm en}(\eta) = \frac{3}{2} K_{0,\rm en} \left(\eta^{7/3} - \eta^{5/3}\right) \times \left[1 + \frac{3}{4}\left(K'_{0,\rm en} - 4\right)\left(\eta^{2/3} - 1\right)\right]. \tag{4.26}$$

Above $P_{\rm trans}$, we use a tabulated equation of state for perovskite and iron or FeS (depending on the core composition assumed) (Seager et al., 2007). The transition between perovskite and the iron-dominated core is defined to occur at a core-mantle boundary pressure $P_{\rm cmb}$. We have adopted room temperature (300 K) EOSs. Including thermal expansion, which we do not do in this work, will make the lower limits derived on the iron mass fraction of KOI 1843.03 even more severe. Figure 4.2 shows the full equation of state that we have adopted.

The relaxation method (described above) requires the conversion of enthalpy to density, which depends solely on the equation of state. Formally, enthalpy H is given by Equation 4.3. The *indefinite* integral that corresponds to substituting Equation 4.26 in Equation 4.3 is

$$\widetilde{H}_{\rm en}(\rho) = \frac{3K_0\rho^{2/3}\left(9(K'_0 - 4)\rho^{4/3} + 7\left(14 - 3K'_0\right)\left(\rho\rho_0\right)^{2/3} + 5(3K'_0 - 16)\rho_0^{4/3}\right)}{16\rho_0^3}. \tag{4.27}$$

The enthalpy as a function of density ρ is then given by

$$H_{\rm en}(\rho) = \widetilde{H}_{\rm en}(\rho) - \widetilde{H}_{\rm en}(\rho_{0,\rm en})\,. \tag{4.28}$$

The enthalpy as a function of density for the tabulated equations of state is computed by interpolating a cumulative trapezoidal integration approximating Equation 4.3, which we denote $\widetilde{H}_{\rm pv}$

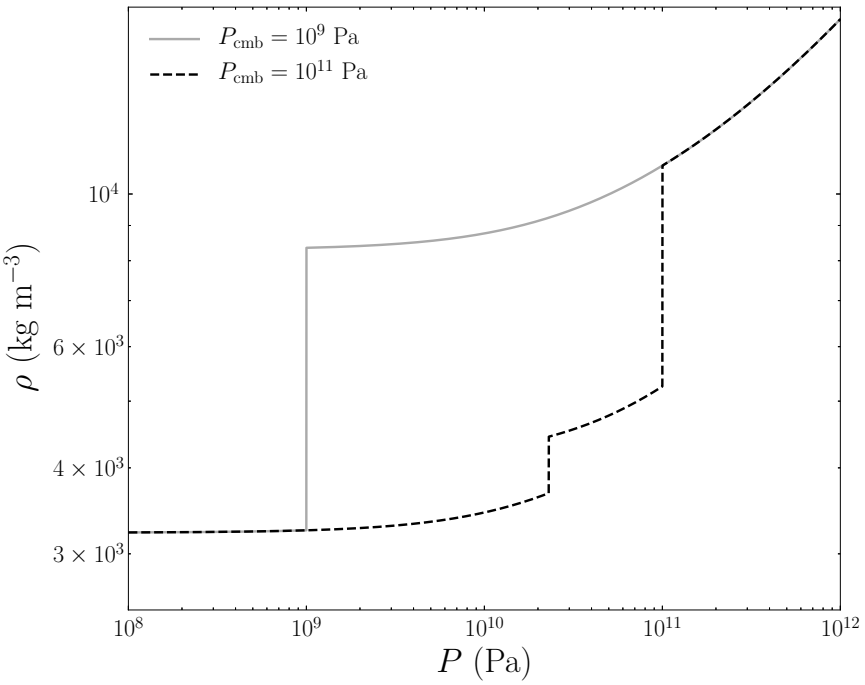

Figure 4.2: Examples of the piecewise equation of state for two values of the core-mantle boundary pressure, P_{cmb}. For the lower value of P_{cmb}, the composition jumps directly from enstatite to iron, whereas, for the higher value, the composition transitions from enstatite to perovskite and then iron.

and $\widetilde{H}_{\mathrm{fe}}$ for perovskite and iron, respectively. This gives us, for $P_{\mathrm{en}}(\rho_{\mathrm{trans}}) = P_{\mathrm{trans}}$,

$$H_{\mathrm{pv}}(P) = H_{\mathrm{en}}(\rho_{\mathrm{trans}}) + \left(\widetilde{H}_{\mathrm{pv}}(P) - \widetilde{H}_{\mathrm{pv}}(P_{\mathrm{trans}})\right) \tag{4.29}$$

and

$$H_{\mathrm{fe}}(P) = H_{\mathrm{pv}}(P_{\mathrm{cmb}}) + \left(\widetilde{H}_{\mathrm{fe}}(P) - \widetilde{H}_{\mathrm{fe}}(P_{\mathrm{cmb}})\right). \tag{4.30}$$

Model validation

To validate our method, we reproduce the classical Roche limit for an incompressible fluid body. For this test case, we achieve $|\Delta P_{\mathrm{orb}}| / P_{\mathrm{orb}} \approx 0.5\%$, where P_{orb} is the analytic Roche limiting orbital period (Equation 4.2), and $|\Delta P_{\mathrm{orb}}|$ is the absolute difference between the analytic expectation and the Roche limit we numerically derive following the method described above. In our validation experiements, the relative error in P_{orb} is observed to be independent of the density of the fluid, as is expected because the simulation is run with a dimensionless, normalized density.

Model interpolation procedure

After all models have been computed, we distill meaningful results by smoothly interpolating within the model grid. When interpolating our model grids, we use the Gaussian process code `george` (Ambikasaran et al., 2014). Our chosen kernel is a constant kernel multiplied by a squared exponential kernel. We allow for "white noise," which in this case is not observational but rather computational noise. We also use a convex hull algorithm as a safeguard against extrapolation. This reduces the extent to which our interpolation code can extrapolate outside our models' bounds.

4.4 Results

KOI 1843.03

Our self-consistent 3D models show that KOI 1843.03 must be very iron-rich to avoid tidal disruption on an orbital period of 4.245 hours. Assuming the planet is composed a pure iron core surrounded by a magnesium-silicate mantle, we find that the $R_p = 0.61^{+0.12}_{-0.08}\ R_\oplus$ radius constraints (Rappaport et al., 2013) imply that KOI 1843.03 must be at least $60^{+7}_{-8}\%$ iron by mass (Figure 4.3). Since rocky planets become compressed to higher densities with increasing size, larger values of the planet radius within the 1σ range translate into more relaxed lower bounds on the iron mass fraction of the planet. Based on our planet interior models, we expect KOI 1843.03's mass to fall in the range 0.32 – $1.06\ M_\oplus$ (Figure 4.4).

Figure 4.4 displays interpolated planet masses for a range of orbital periods and core mass fractions in systems consistent with KOI 1843.03's host star mass and transit radius. The boundary of the colored contours in the lower left-hand corner corresponds to the Roche limit; as orbital period decreases, the core mass fraction is more tightly constrained. As anticipated, considering a fixed orbital period in Figure 4.4, increasing the planet's iron mass fraction increases the planet's mass. Less intuitively, at fixed core mass fraction, decreasing the planet's orbital period also leads to an increase in the inferred planet mass. This is due to the tidal distortion of the planet; at shorter orbital

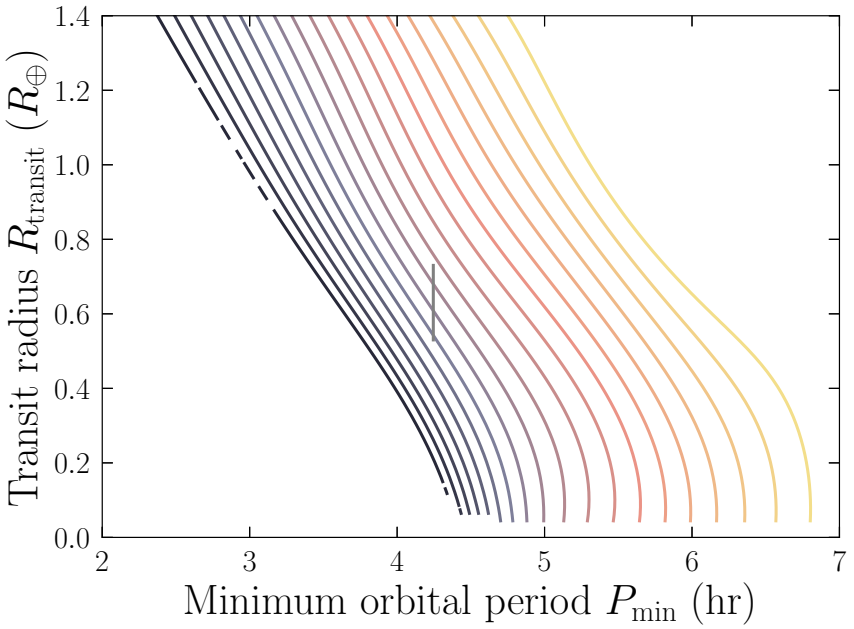

Figure 4.3: Contours of constant core mass fraction as a function of transit radius and minimum orbital period. The vertical gray line indicates the 1σ bounds on the transit radius for KOI 1843.03. Contours are spaced in 5% intervals in core mass fraction, with darker colors corresponding to high core mass fraction and lighter colors corresponding to low core mass fraction. As expected, denser planets with higher core mass fractions survive to shorter orbital periods. The limiting orbital period of a pure iron planet is approximately 3.8 hours at 0.5 $M_\oplus$, 3.6 hours for 1 $M_\oplus$, and 3.5 hours for 2 $M_\oplus$. We note that this figure marginalizes over stellar mass, because stellar mass only weakly affects the Roche-limiting minimum orbital period (Rappaport et al., 2013). The stellar density does, however, affect whether the planet can reach its Roche limit before colliding with the star (i.e., $a = R_\star$) and thereby the minimum survivable orbital period for the planet.

periods, the volume of the planet exceeds $4/3\pi R^3_{\rm transit}$ by larger and larger factors.

As it orbits less than one stellar radius from the host star's photosphere ($a/R_\star = 1.9$), KOI 1843.03 will be significantly elongated in the direction of the star due to tidal distortion. Based on the parameters of KOI 1843.03, our models predict that it must be *at least* 31% longer along the star-planet line than along the perpendicular axes (aspect ratio of about 1.3), and our models support a value up to nearly twice as long along the star-planet line (aspect ratio of almost 1.8); various possibilities are illustrated in Figure 4.5. For comparison, Saturn has an aspect ratio of about 1.1.

The Earth's core is not pure iron; it contains an unknown mixture of light elements. To determine what effect these light elements might have, we generated a second grid of models with an EOS

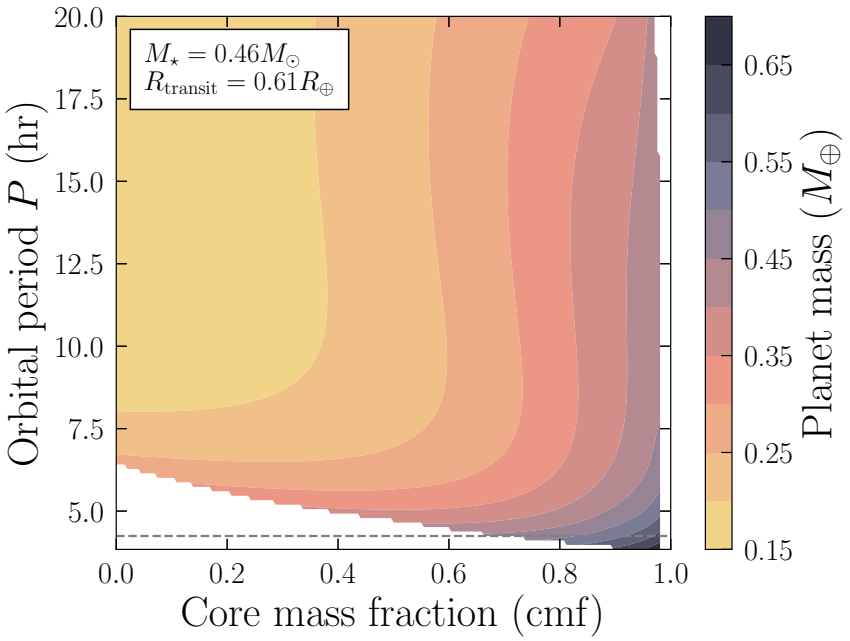

Figure 4.4: Composition and mass constraints on planets with KOI 1843.03's measured transit radius and host star mass. Colored contours show the values of the planet mass, which increases with decreasing orbital period and increasing core mass fraction. The boundary of the colored contours in the lower left-hand corner corresponds to the Roche limit. The dashed gray line indicates the measured orbital period of KOI 1843.03.

appropriate to an FeS core (see Figure 4.6). KOI 1843.03 would need a core mass fraction of at least 80% if it has a core comprised of FeS, but this measurement is only valid for a transit radius of 2σ greater than the mean. Both pure Fe and pure FeS are end-member core compositions; the true core density of KOI 1843.03 likely lies somewhere in between.

Iron-enhanced USP planets

KOI 1843.03 is one of a growing class of iron-enhanced, closely-orbiting planets discovered.

K2 137b is remarkably similar to KOI 1843.03 but has a slightly longer orbital period (by 4 minutes), a larger transit radius (0.89 $R_\oplus$), and a more massive host star (0.463 $M_\odot$) (Smith et al., 2018). Our 3D models show that K2 137b must be at least $42 \pm 5\%$ iron by mass to have avoided tidal disruption. Its mass lies somewhere between 1.01 and 2.80 $M_\oplus$ (Figure 4.7), which is consistent with the radial velocity upper limit of 3 $M_{\rm Jup}$. We find that K2 137b's aspect ratio is bounded between

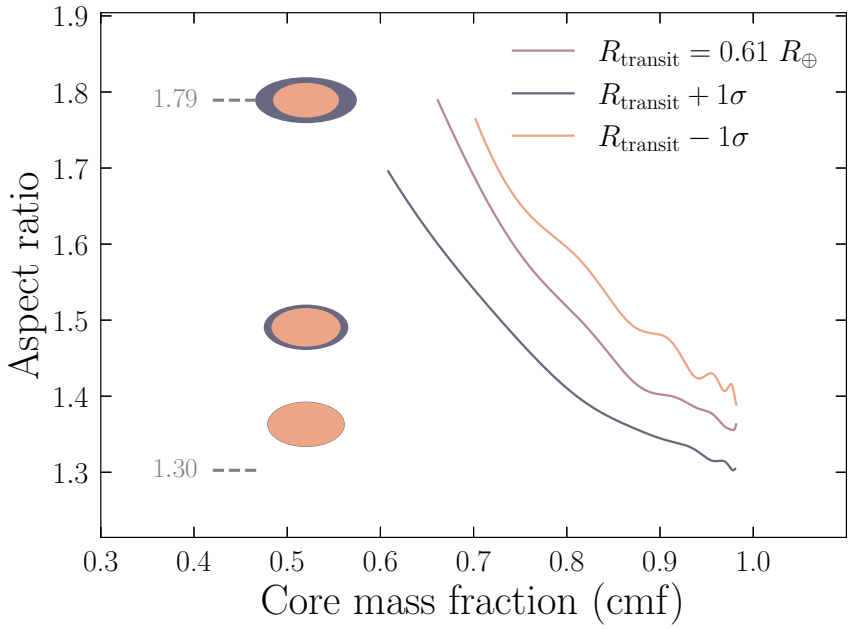

Figure 4.5: Aspect ratio constraints on KOI 1843.03, as a function of core mass fraction. To the left of the plot, we indicate the maximum and minimum values of aspect ratio supported by the model grid and show three representative planet cross-sections (assuming ellipsoidal shapes) wherein peach and navy represent the iron-dominated core and silicate mantle, respectively. Results are shown both at the measured transit radius 0.61 $R_\oplus$and the 1σ limits (0.53 $R_\oplus$and 0.73 $R_\oplus$).

1.21 and 1.66 (provided the true transit radius is within the 1σ measurement, see Figure 4.8). The constraint on K2 137b's aspect ratio is not as extreme as the constraint on KOI 1843.03's.

Two additional transiting exoplanets — K2 229b ($M_p = 2.59\ M_\oplus$, $R_{\rm transit} = 1.164\ R_\oplus$, $P_{\rm orb} =$ 14.0 hr, Santerne et al. 2018) and K2 106b ($M_p = 8.36\ M_\oplus$, $R_{\rm transit} = 1.52\ R_\oplus$, $P_{\rm orb} = 13.7$ hr, Guenther et al. 2017) — have been inferred to have iron-rich compositions based on their radial velocity measured masses. Based on our models, we infer iron mass fractions of $0.605^{+0.204}_{-0.181}$ and $0.691^{+0.206}_{-0.169}$, and aspect ratios of $1.02^{+0.002}_{-0.003}$ and $1.01^{+0.003}_{-0.003}$, for K2 229b and K2 106b respectively. (Note that the errorbars reported here are not one standard deviation, as the distributions tend to be non-Gaussian, but rather the 25% and 75% percentiles; the full distributions are shown in Figures 4.9 and 4.10.)

Of the roughly 7 rocky ultra-short period exoplanets ($R_p \leq 1.7\ R_\oplus$, $P_{\rm orb} \leq 1$ day) with masses and radii measured to within 20% precision to date (CoRoT-7b, Kepler-10b, Kepler-78b, K2 106b,

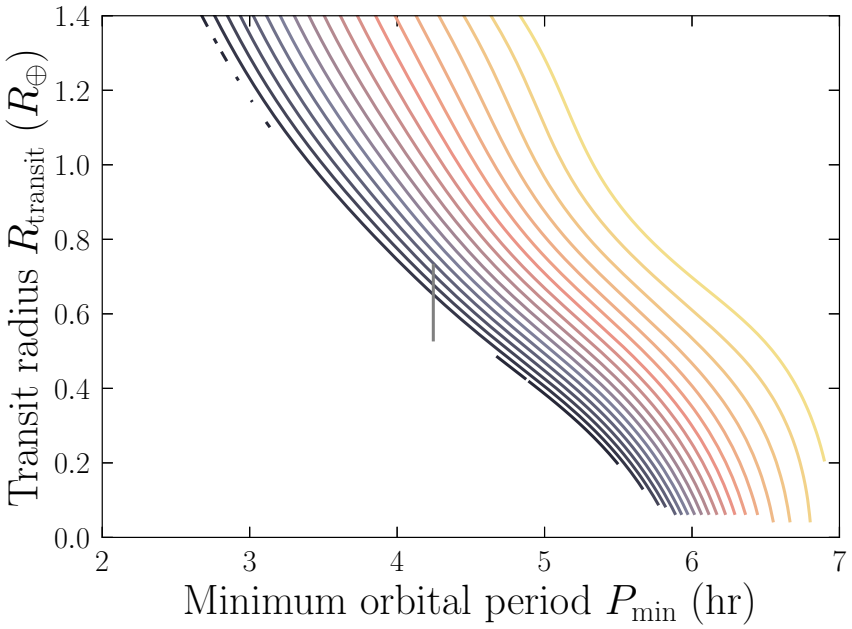

Figure 4.6: Minimum orbital period as a function of transit radius and composition for planets with cores comprised of pure FeS. The solid gray line indicates the range of possible radii (within 1σ limits) for KOI 1843.03, showing that it is, for smaller radii, most likely incompatible with a pure FeS core, as it would be inside the Roche limit. In general, planets with higher density iron cores can survive closer to their host stars than planets with cores polluted by FeS. While the limiting orbital period of a pure FeS planet is approximately 4.5 hours at 0.5 $M_\oplus$, 4.3 hours for 1 $M_\oplus$, and 4.0 hours for 2 $M_\oplus$. This figure is analogous to Figure 4.3, but assumes an FeS core composition instead of Fe.

K2 141b, K2 229b, HD-3167b), 2 are iron-enhanced. Including the planets with density upper limits from the Roche limit (KOI 1843.03 and K2 137b), we find that just under half (4 out of 9) of the ultra-short period exoplanets with physically-meaningful constraints on their densities characterized to date are iron-enhanced.

Analytic approximation to the Roche limit

Our numerical Roche limits can be approximated by modifying the power-law parameters of the well-known expression for the classical Roche limit, re-expressed in terms of orbital period using Kepler's third law (Rappaport et al., 2013); this is given by Equation 4.2. Including additional terms up to quadratic order that encapsulate a dependence on the degree of central concentration of the

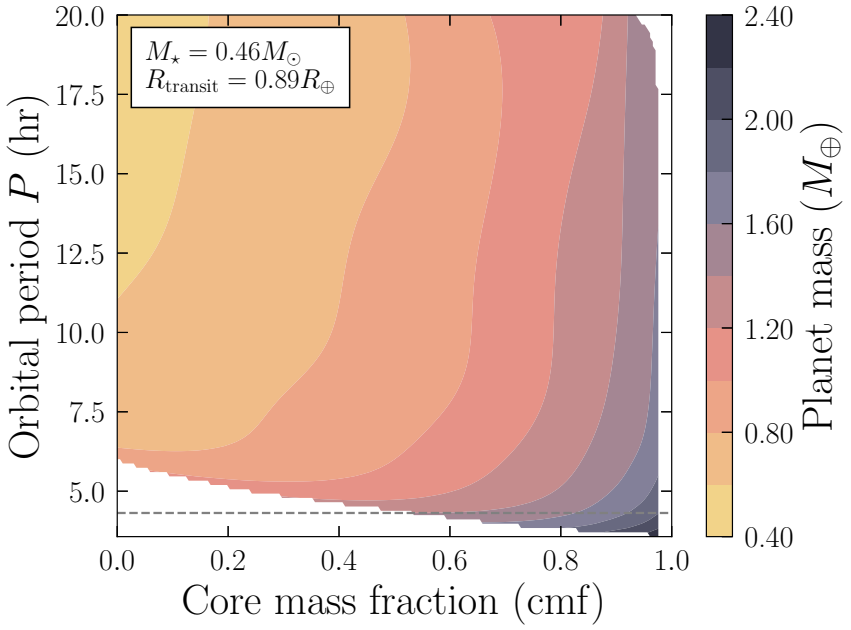

Figure 4.7: Contours of constant planet mass as a function of core mass fraction and orbital period for K2 137b. The orbital period of K2 137b is indicated by the dashed gray line. This figure is analogous to Figure 4.4, but for the planet K2 137b instead of KOI 1843.03.

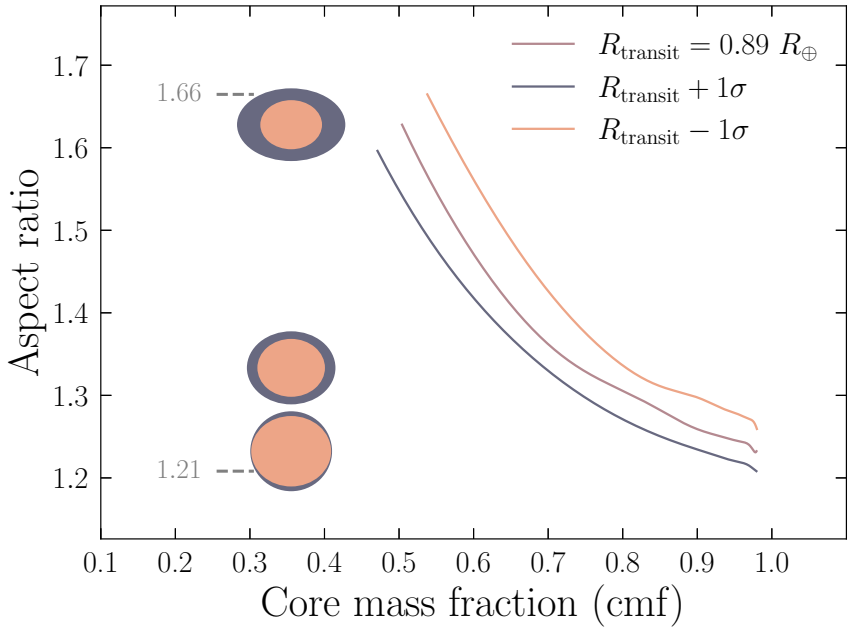

Figure 4.8: Aspect ratio constraints on K2 137b, as a function of core mass fraction at three different values for the transit radius: the measured value 0.89 $R_\oplus$and the 1σ limits (0.80 $R_\oplus$and 0.98 $R_\oplus$). This figure is analogous to Figure 4.5, but for the planet K2 137b instead of KOI 1843.03.

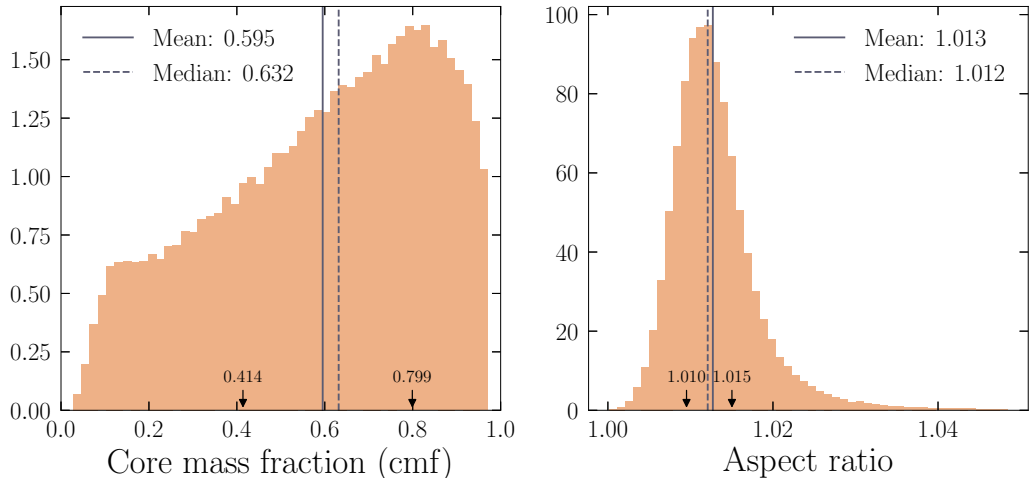

Figure 4.9: Histograms of core mass fraction and aspect ratio for K2 229b. The mean and median of each distribution are indicated by vertical lines, and black arrows show the 25% and 75% percentiles; we use these values instead of the standard deviation for errorbars in the text. We are not able to place a very tight constraint on the core mass fraction of this planet, but our models indicate that it is very unlikely to be significantly distorted. To compute these histograms, it is necessary to choose a mass and radius distribution; we select an uncorrelated bivariate Gaussian distribution based on the planet's measured mass and transit radius ($M_p = 2.59 \pm 0.43\ M_\oplus$ $R_p = 1.164^{+0.066}_{-0.048}\ R_\oplus$, Santerne et al. 2018) for this purpose.

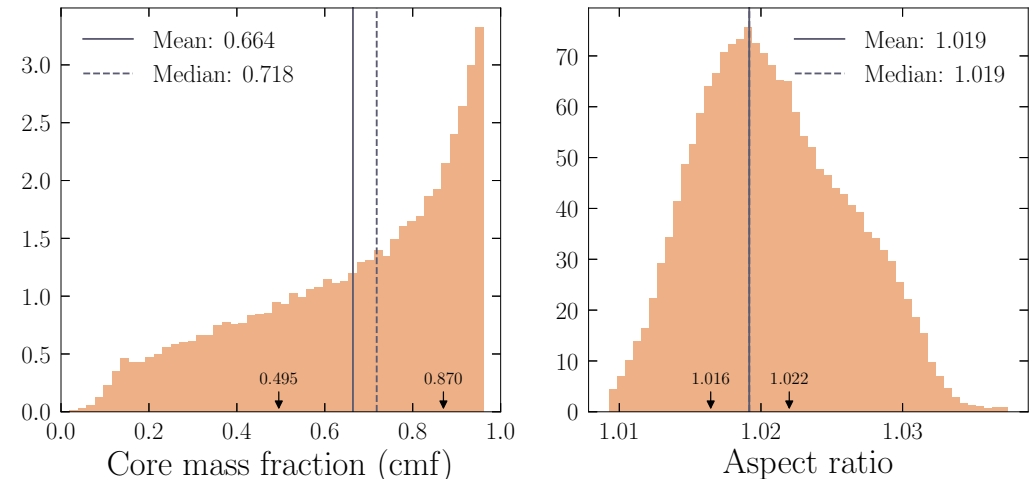

Figure 4.10: Histograms of core mass fraction and aspect ratio for K2 106b ($M_p = 8.36^{+0.96}_{-0.94}\ M_\oplus$ $R_p = 1.52 \pm 0.16\ R_\oplus$, Guenther et al. 2017), analogous to Figure 4.9. We again find that, though the core mass fraction is not constrained very tightly, the aspect ratio is likely to be very close to unity.

planet (i.e., the ratio of the planet's maximum/central density to its mean density), we obtain,

$$\begin{aligned}\log_{10}\left(\frac{P_{\rm orb,min}}{1\ {\rm hr}}\right) = &\log_{10} C + \alpha \log_{10} x + \beta \log_{10} y \\ &+ \gamma \left(\log_{10} x\right)^2 + \delta \left(\log_{10} y\right)^2 \\ &+ \epsilon \left(\log_{10} x \log_{10} y\right)\end{aligned} \tag{4.31}$$

where $x \equiv \rho_p / \left(1\ {\rm g\ cm^{-3}}\right)$, $y \equiv \rho_{\rm max}/\rho_p$. Using sequential least squares programming[4], we find the following best fit parameters to the 2D surface defining the Roche limit: $C = 12.013$, $\alpha = -0.571$, $\beta = 0.047$, $\gamma = 0.108$, $\delta = 0.562$, and $\epsilon = -0.527$.

Rappaport et al. (2013) report an interpolation formula without the quadratic terms, where $C = 12.6$, $\alpha = -0.5$, and $\beta = -0.16$. If we set the quadratic terms to zero, our best-fitting revised Roche limit has $C = 11.86$, $\alpha = -0.52$, and $\beta = 0.086$.

While this approximation is a useful tool, interpolation within the model grid is our suggested approach for using the models.

4.5 Discussion

Formation scenarios

How did KOI 1843.03, K2 137b, K2 229b and K2 106b form and/or evolve to such short orbital periods and iron-rich compositions?

Several theories for the origin of Mercury's high iron content involve impacts that remove the outer silicate layers of a differentiated planet. Scenarios involving a single giant impact (e.g., Benz et al., 2008), a hit-and-run collision (e.g., Asphaug & Reufer, 2014), or the cumulative effect of multiple collisions can all feasibly lead to a Mercury-like outcome, though a single-giant impact or hit-and-run impact require highly tuned collision geometries to reproduce Mercury's mass and iron mass fraction (Chau et al., 2018). In the context of exoplanets, Marcus et al. (2010) used smoothed

[4] SLSQP, implemented in SciPy, (Jones et al., 2001–), using an algorithm originally developed by Dieter Kraft

Planet	Orbital velocity (km s^{-1})	Flux (erg cm^{-2} s^{-1})
KOI 1843.03	320	3×10^9
K2 137b	270	1×10^9
K2 106b	270	2×10^{10}
K2 229b	240	3×10^9
Mercury	48	9×10^6

Table 4.1: Approximate values for the orbital velocities and fluxes at the orbital surface for the four planets we consider in this paper. We compare these values to the corresponding values for Mercury, the planet with the shortest orbital period in our own Solar System.

particle hydrodynamics (SPH) simulations of giant impacts to infer that iron mass fractions of up to than 80% can be achieved with a single impact for planets less than 2 $M_\oplus$. Marcus et al. (2010) neglected to track the dynamical evolution of the impact ejecta, however, and reaccretion of the ejected mantle is likely to dilute the iron-enhancement of a giant impact (Gladman & Coffey, 2009). USP planets would be susceptible to high-velocity erosive collisions due to the extreme orbital velocities along their orbits (for example, about 320 km s^{-1} for KOI 1843.03 compared to about 48 km s^{-1} for Mercury, Table 4.1). Their proximity to their stars, with shorter orbital timescales and stronger stellar irradiation environments (Table 4.1), would also affect the reaccretion of ejected silicates. Further work is needed to evaluate the effect of collisions on the compositions of USP planets.

Alternatively, these closely-orbiting iron-enhanced planets could have initially formed from iron-rich material. Both the condensation sequence (wherein iron condenses at a higher temperature than magnesium silicates) (Lewis, 1972) and photophoresis (which separates high-thermal-conductivity iron dust grains from lower-thermal-conductivity silicate grains) (Wurm et al., 2013) can lead to an enhancement of iron in the solid phase at the inner edge of the protoplanetary disk. These fractionation processes that operate primarily at the disk inner edge could imprint themselves as a statistical iron enhancement of the ultra-short-period planet population.

A third possibility is that KOI 1843.03 and K2 137b are right at their Roche limits and have been gradually losing their outer silicate layers to Roche lobe overflow as their orbits tidally decay (Jia & Spruit, 2017). If KOI 1843.03 started with a chondritic or Earth-like iron-to-silicate ratio and

mass of about 0.7 $M_\oplus$ (an intermediate value between our estimated limits), the planet's initial mass would have been about 1.4 $M_\oplus$. The orbital period precision achieved over the 4-year baseline of the *Kepler* mission is insufficient to resolve expected decay in KOI 1843.03's orbit. This scenario does not explain the compositions of the longer-orbital-period K2 229b and K2 106b, however, since they are outside their Roche limits.

Thermal effects

We have not modeled the interior temperature profiles of these planets. Indeed, we have adopted room temperature (300 K) equations of state. The surface temperature of KOI 1843.03 and other USP planets can exceed 2000 K, with temperature increasing further toward the center. Thermal expansion would cause the planet of specified mass and composition to have a larger volume and lower mean density compared to the models presented here. Temperature may also affect the pressure of the phase transition between enstatite and perovskite, which we have fixed to 23 GPa, following Sotin et al. (2007). There are two common ways of incorporating temperature into the EOS (Jackson, 1998): One may either regard the typical EOS coefficients as being temperature-dependent, or one may add a "thermal" pressure at every point. The effect of temperature is more severe for lower mass bodies. Including thermal expansion will make the constraints on the iron mass fraction of KOI 1843.03 even more severe, strengthening our conclusions.

Effect of material strength

Our models provide the first self-consistent constraints on the hydrostatic equilibrium shapes and Roche limits of ultra-short period rocky planets. The effect of material strength in the planets' shapes is not taken into account in these calculations.

Looking to the Solar System bodies for inspiration, we see that once bodies are roughly 200 km (for icy materials) to 300 km (for rocky materials) in radius their self gravity is sufficient to overcome their material strength and they achieve a rounded shape. Iapetus (mean radius 734.5 ± 2.8 km, Roatsch et al. 2009) is the largest Solar System body measured to have significant deviations from

a hydrostatic equilibrium shape (Thomas, 2010). Since KOI 1843.03 is about 4000 km in radius, it is safely in the regime where self-gravity dominates the material forces and hydrostatic equilibrium determines its leading-order shape, satisfying the minimum mass criterion in the IAU definition of a planet.

To leading order, Earth-mass scale planets (such as KOI 1843.03, K2 137b, K2 229b, and K2 106b) are in hydrostatic equilibrium, with rigidity representing a minor correction. In our models, the central pressure of KOI 1843.03 are on the order of 10^{11} – 10^{12} Pa which is orders of magnitude larger than the shear strength of iron (Clatterbuck et al., 2003) and peridotite (Handy et al., 1999).

The high instellations of USP planets can lead to molten surfaces (e.g., Léger et al., 2011; Kite et al., 2016), which further limit deviations from hydrostatic equilibrium shapes. In the extreme of no heat redistribution, the substellar point of KOI 1843.03 could exceed 2000 K, computed from $T_{ss} = T_\star \left(1-\alpha\right)^{1/4} \sqrt{R_\star/a} \approx 2500$ K assuming a basalt-like planet surface albedo $\alpha = 0.1$ (e.g., Kite et al., 2016). This temperature is sufficiently hot to melt metallic iron (melting point 1811 K) and is hotter than the liquidus of peridotite (Takahashi, 1986), the dominant rock in Earth's upper mantle. Thus, the planet's surface would have too little strength to sustain topography that could significantly influence the transit depth.

In using the Roche limit to constrain the bulk compositions of KOI 1843.03 and K2 137b, we have followed Rappaport et al. (2013) and Jia & Spruit (2017) and neglected the effect of material strength. It is unclear whether material strength or friction would help the planet to survive intact inside its Roche limit for gigayear timescales (e.g., Davidsson, 1999; Holsapple & Michel, 2006). As highlighted by Winn et al. (2018), further work is needed to model the destruction of USP planets that exceed their Roche limits.

Planet mass loss

The surface of KOI 1843.03 could be actively sublimating. Kite et al. (2016) models the exchange between atmospheric silicate, surface magma pools, and interior material for a hot, rocky exoplanet. If a rock vapor atmosphere is contributing to the transit depth in the *Kepler* bandpass, that only

makes our constraints on the the iron fraction in KOI 1843.03 even more severe.

Though they do not themselves show evidence of evaporation in *Kepler* photometry, KOI 1843.03, K2 137b, K2 229b and K2 106b could be more massive cousins to the catastrophically evaporating rocky planet discovered orbiting KIC12557548. KIC12557548 shows asymmetric and variable transit shapes that have been interpreted as evidence of a dusty outflow of vaporized material driven by a thermal wind (Rappaport et al., 2012). Even for KOI 1843.03, the smallest among these close-orbiting iron-enhanced planets, with a mass in excess of $0.3\ M_\oplus$, the escape velocity from the surface is too high to drive a substantial hydrodynamic wind of sublimated silicates (Perez-Becker & Chiang, 2013). Detailed models of radiative hydrodynamic winds from evaporating rocky USP planets (Perez-Becker & Chiang, 2013) show that a $0.1\ M_\oplus$ rocky planet could survive at a surface temperature of ~ 2200 K with negligible mass loss for tens of gigayears.

Potential for follow-up observations

Due to the red colors of the early M host-star, the near infrared (NIR) and infrared (IR) offer the best opportunities for further observational characterization of KOI 1843.03. Given our constraints on its mass and bulk composition, the possible range for KOI 1843's radial velocity semi-amplitude ($K_1 = 0.60$ – 1.98 m s^{-1}) spans the current state of the art precision of 1 m s^{-1}. The host star is too faint for precision radial velocity follow-up in the visible with any existing telescope or instrument but may be a feasible candidate for radial velocity follow-up in the NIR. Photometric follow-up in the infrared, for instance with the *Spitzer* Space Telescope or the James Webb Space Telescope could confirm the planetary nature of KOI 1843.03 (Désert et al., 2015).

Photometric follow-up could also provide a longer time baseline to reveal evidence of tidal evolution of the orbit. In principle, given sufficient time sampling, the detailed shape of the transit lightcurve (as the projected cross-section of the planet changes viewing angle during transit) may further constrain KOI 1843.03's aspect ratio and bulk composition. Such an effect has been studied for distorted giant planets (Leconte et al., 2011).

To predict the IR transit signal-to-noise ratio (SNR), we use the `isochrones` software (Mor-

ton, 2015) modified for *Spitzer* bandpasses using data from Hora et al. (2008) and Indebetouw et al. (2005) to compute predicted apparent magnitudes for KOI 1843 in each of the four *Spitzer* bandpasses. In the 3.6 µm, 4.5 µm, 5.8 µm, and 8.0 µmbands, respectively, we predict magnitudes of 11.0 ± 0.05, 11.0 ± 0.08, 10.9 ± 0.08, and 10.9 ± 0.07. Scaling from the SNRs obtained by Désert et al. (2015) on stars with similar *Spitzer* magnitudes as KOI 1843, a signal-to-noise ratio for a single KOI 1843.03 transit could range from about 0.36 to 0.93. Observing multiple transits could improve the SNR.

KOI 1843.03 may not hold the records for the shortest orbital period and most distorted known exoplanet for long. The Transiting Exoplanet Survey Satellite (TESS, launched in 2018) should find several ultra-short-period transiting planets as it surveys the brightest stars over the entire sky; recent simulations by Barclay et al. (2018) predict detection for 52 planets with orbital periods of $P_{\rm orb} < 1$ day. Our models, which provide the first self-consistent constraints on the Roche limits of Earth-mass-scale rocky planets (Figure 4.3), will enable composition constraints on these future ultra-short period planet discoveries.

E.M.P. and L.A.R. thank Dr. Benjamin T. Montet for his analysis of the KOI 1843.03 *Kepler* light curve and and constraint on the rate of change in the planet's orbital period. We also thank Drs. Andrew Vanderburg, Saul Rappaport, Josh Winn, and Darin Ragozzine for helpful discussion, and reviewer Dr. Erik Asphaug for valuable suggestions.

This material is based upon work supported by a National Science Foundation Graduate Research Fellowship under Grant Nos. DGE1144152 and DGE1745303. L.A.R. acknowledges NSF grant AST-1615315. The computations in this work were carried out with resources provided by the University of Chicago Research Computing Center.

Chapter 5

Transit Shapes of Tidally-Distorted Rocky Exoplanets

This chapter has not been submitted for publication at this time.

5.1 Introduction

In Price & Rogers (2020) and Chapter 4, we explored the possibility of non-spherical planets and modeled their interior structures. This is an important first step, yet our observations of exoplanets are currently limited to indirect measurements like transit light curves. If a planet assumes a non-spherical shape, its light curve should similarly be distorted from the known transit shape for a planet with a constant, circular cross-sectional area. Below, we use raytracing and the three-dimensional, self-consistent models from Price & Rogers (2020) to synthesize light curves for non-spherical, exoplanets.

Previous works have modeled transit shapes for non-spherical exoplanets, taking both analytic (Leconte et al., 2011; Saxena et al., 2015) and Monte Carlo (Carado & Knuth, 2020) approaches for planets of various sizes. Leconte et al. (2011) considered the effect of tidal forces and rotation on gas giant planets, but the analytic approach proposed does not take into account the nonzero density

at zero pressure of rocky planets. Saxena et al. (2015) consider triaxial ellipsoidal rocky planets with a single layer, finding that the transit shape variations might be significant for close-in planets orbiting M stars. Finally, Carado & Knuth (2020) uses random sampling to explore the effects of inclination and precession on the transit light curves of ellipsoidal planets. The differences, then, between this study and previous works are that we have access to a library of self-consistent, two-layer, rocky planet shapes and do not need to make an ellipsoidal assumption in our modeling; and that this library of planet shapes enables us to explore the possibility of constraining the core mass fraction of ultra-short period (USP) planets using high-cadence transit light curve observations.

The work in this chapter is ongoing. In Section 5.2, we present the method for computing planet shapes and raytracing their transit light curves. Sections 5.3 and 5.4 present our preliminary results and a short discussion, respectively.

5.2 Methods

We seek to model the transit shapes of USP planets based on self-consistent three-dimensional models which we explored in Price & Rogers (2020). For this work, we utilize a fully parallel version of the `PySquish` code developed in Price & Rogers (2020), `SQUISHv2`. In the following sections, we review the important concepts for modeling the planets' structures and transits.

Self-consistent modeling

The original `PySquish` code, fully described in Chapter 4, was implemented in a mixture of Python, Cython, and C++. It was ultimately a serial code that used the "embarrassingly parallel" model to divide tasks between CPUs. One task, in this context, is computing a single sequence of interior simulations for fixed core-mantle boundary pressure, $P_{\rm cmb}$; scaled central pressure, $\hat{P}_{\rm max} = P_{\rm max}/P_{\rm cmb}$; and scaled semimajor axis, $\hat{a} = a/r_A$, with r_A the planet radius along the $\hat{x}$ axis (see Figure 4.1). In the embarrassingly parallel model, independent tasks are divided between available CPUs at the beginning of the simulation, and each CPU is only able to work on its predefined set of tasks. Since

`PySquish` explored a grid of $P_{\rm cmb}$, $\hat{P}_{\rm max}$, and $\hat{a}$ values, we chose to divide tasks based on one or more of these grid dimensions. One disadvantage of this approach is that there is no way *a priori* to know how many iterations (and, therefore, how much time) a particular sequence of interior simulations will take, meaning that one thread may spend time idling while another is busy.

Ideally, the work could be split more evenly between all available threads, and that is exactly the design goal of `SQUISHv2`: It is developed entirely in C and uses MPI (Message Passing Interface) commands to communicate between threads and PETSc (Balay et al., 1997, 2018) for parallel data storage. We selected a configuration where pairs of processes work together on individual tasks, and several process pairs are available to complete the next incoming task. At the beginning of the simulation, each available process pair receives one task to complete; when it reports to a master thread that it has finished its task, it is assigned the next task in the queue, and this process continues until all tasks are complete.

Besides these design differences, the basic flow of a particular task is the same in both codes. We begin with a guess for the planet's density, which we take to be a constant-density ellipsoid; the guess is quickly revised by the iterative method, so it is unnecessary to have an accurate initial guess. From the density, the self-gravitational potential of the planet is computed using a spherical harmonic expansion. The planet's gravitational potential, the star's gravitational potential, and the centrifugal potential together are used to compute the enthalpy, which is then converted back to a density. The iterations repeat until a convergence criterion is reached; at that point, the radius of the planet on the $\hat{z}$ axis $\hat{r}_B$ is reduced by one step, such that it resides on the next lowest grid point, and we start over, using the last converged interior structure as the next input guess. The curious reader is referred to the relevant methods papers (Hachisu, 1986a,b; Price & Rogers, 2020).

`SQUISHv2` has the additional advantage over `PySquish` that it saves the full planet interior structure to disk once that sturcture has converged, so we are able to extract the bounding surface of a planet and feed it into the raytracing step.

Raytracing

The analytic form of a spherical planet's transit across a uniform or limb-darkened stellar disk is known (e.g., Mandel & Agol, 2002). However, our planet models are numerically determined, so their surfaces will not have a simple, analytic forms that can be used to find transit shapes. Raytracing is a direct way of simulating a transit, where virtual "photons" are emitted from the stellar disk and may intersect the planet surface. Raytracing mimics the physical process of a planet blocking photons from reaching an observer, so it is appropriate for any planet shape.

For performing the raytracing operation, we use the NVIDIA OptiX (Parker et al., 2010) software on an NVIDIA Quadro RTX 5000 graphics card. OptiX uses an acceleration structure that encodes the graphics primitives in the scene to be raytraced. The acceleration structure is built once and then used for all subsequent raytracing operations. To maximize performance, we build the acceleration structure (containing the planet surface) once and work in a rotated frame, shown in Figure 5.1. In the rotated frame, the star, of radius $\hat{r}_\star$, moves around the planet at a distance $\hat{a}$. We additionally place a bounding sphere of radius $\hat{r}_{\rm bnd} = 16/15$ around the planet surface and then only trace photons that will intersect the bounding surface. $\hat{r}_{\rm bnd}$ is determined by the underlying simulation, where the radius grid extends to $\hat{r} = 16/15$ in dimensionless simulation units.

Raytracing remains an expensive operation, however. To limit the number of planets for which we raytrace transits, we predict which planets are most likely to be similar to a planet of interest, such as KOI 1843.03. We accomplish this by placing tight constraints (1% relative error) on orbital period and looser constraints (10–20% relative error) on the transit radius and stellar density.

5.3 Results

In Figure 5.2, we present the preliminary results of the raytracing on a grid of KOI 1843.03-like planet models. The most clear signature of the transit of a distorted planet, as compared to the transit of a spherical planet, is its characteristic "W" shape. Furthermore, planets with a lower core mass fraction (more iron-poor) have more distorted transits compared to the ideal transit shape of

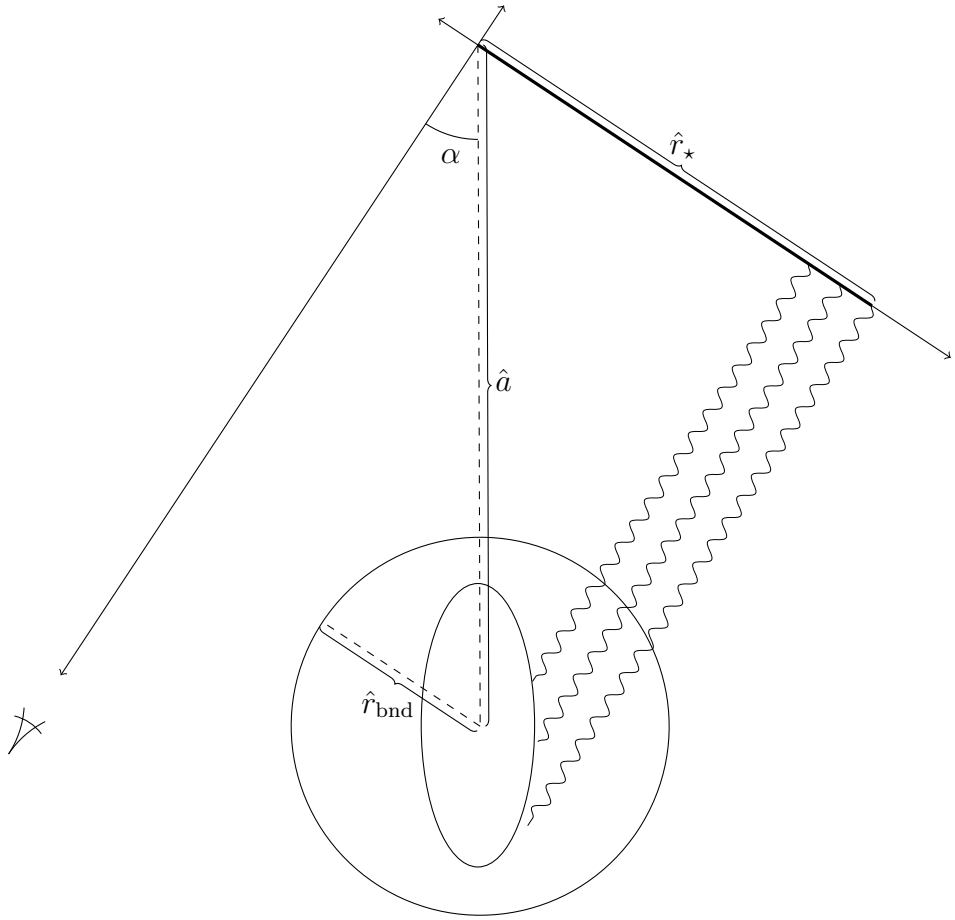

Figure 5.1: Geometry of the raytracing problem (not drawn to scale). The ellipse represents the non-spherical surface of the planet, while the sphere of radius $\hat{r}_{\mathrm{bnd}}$ is a bounding surface to accelerate raytracing. The star, of radius $\hat{r}_\star$ and at a distance $\hat{a}$, is rotated around the planet's axis so that the geometry acceleration structure only has to be computed once. The wavy lines in the figure indicate virtual photons, and the "eye" symbol indicates the direction to the observer.

a sphere, while those with higher core mass fraction (more iron-rich) have less distorted transits. This logically follows from the fact that iron-rich planets are more spherical than their iron-poor counterparts.

We immediately see that there is a discrepancy between the measured transit depth of KOI 1843.03 and that of the model planets. We hypothesize that this is due to the fact that the models are stored on a discrete radial grid. The radius points on that grid are equidistant with spacing $\Delta\hat{r}$. Then, if we take the transit depth $\delta = (\hat{r}/\hat{r}_\star)^2$, we find an error on the transit depth proportional to $2\hat{r}\Delta\hat{r}$ by simple error propagation. We overplot the maximum value we expect for this error on

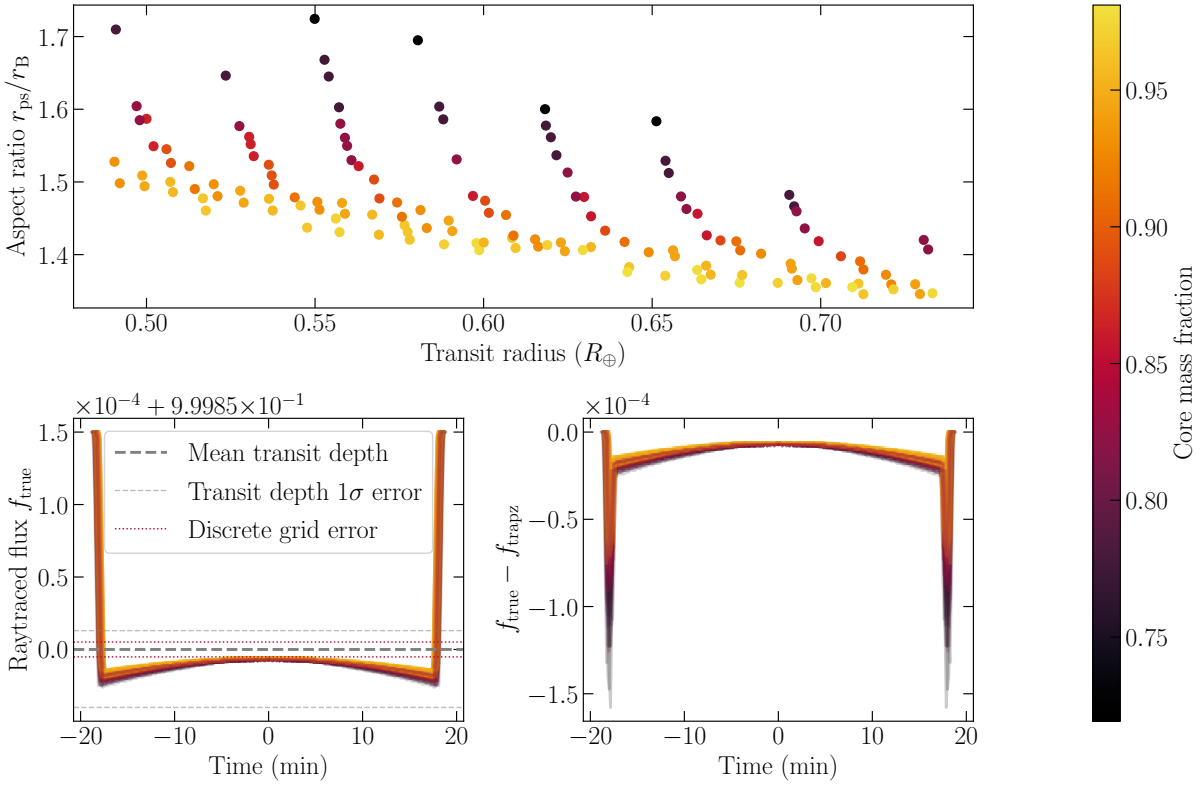

Figure 5.2: Preliminary results for a grid of KOI 1843.03-like planets. In the top panel, we show a plot of aspect ratio as a function of transit radius, colored by core mass fraction (cmf), to give the reader an idea of the ranges of parameters involved. In the lower two plots, we show the full raytraced transits (left) and the difference between the raytraced transits and the corresponding trapezoidal model, defined in Carter et al. (2008), for each one (right). In the bottom left plot, we additionally show the mean transit depth of KOI 1843.03 (thick, gray, dashed line) and the 1σ error above and below (thin, gray, dashed line). The offset between the raytraced transit depth and that of KOI 1843.03 may be explained by the error associated with using a discrete radius grid, estimated by the red, dotted line.

Figure 5.2, and, indeed, it is of about the same order of magnitude as the discrepancy.

5.4 Discussion

This chapter remains a work in progress. One of the most important questions that remains is the effects of limb darkening on the shape of the distorted transit and whether limb darkening "washes out" the characteristic shape of the transit entirely. In the particular case of KOI 1843.03, since there

are two other planets in the same system (one confirmed and one candidate), it may be possible to constrain the limb darkening coefficients and then constrain the shape of KOI 1843.03. Another option is using multi-wavelength observations of KOI 1843.03's transit, since the effects of limb darkening are wavelength-dependent.

E.M.P. gratefully acknowledges support from National Science Foundation Graduate Research Fellowship Program (GRFP) grants DGE1144152 and DGE1745303. The specialized hardware used for raytracing was purchased using the Harvard University astronomy department's Loomis Fund.

Chapter 6

Concluding Remarks and Outlook

In this dissertation, I have described my work of the last six years to better understand protoplanetary disks and extreme exoplanets. Chapters 2 and 3 showcased my work on protoplanetary disk modeling, using relatively simple but robust numerical techniques. We found that the effects of accretion and grain drift are both important for understanding disk evolution and, ultimately, exoplanet outcomes. Chapters 4 and 5 presented published and ongoing work to understand the interior structures of USP planets and how the interior structures might be constrained using light curve measurements.

There are many questions that remain to be answered. For example, all of the disk modeling undertaken for this dissertation focuses on the disk midplane. While this is convenient for planet formation, which is largely concentrated in the midplane due to settling, turbulence can loft material into the disk atmosphere, where it may take part in chemical reactions there before settling back to the midplane. Furthermore, though we have learned more about extreme exoplanets, like USP planets, in the past few years, the topic of their formation is still a matter of debate. Much progress has been made, but there is still much to be done to better understand planet formation in disks. The following sections describe work I will be following through as a postdoctoral researcher.

6.1 Grain growth and evolution

In Chapter 3, I introduced a disk model with two non-reacting chemical species and two static dust populations. A more realistic model would allow the dust populations to grow and fragment according to some mathematical prescription, such as the Smoluchowski equation (Smoluchowski, 1916) for particle coagulation. While we theorize in the aforementioned chapter that the exact distribution of solids is less important than the presence of one large and one small population, it will be interesting to determine the effects of grain growth and fragmentation quantitatively. This is an open problem, particularly because effects such as porosity and ice coatings can affect sticking probabilities (Testi et al., 2014).

The model of Chapter 3 included CO and H_2O as chemical species; they were allowed to adsorb onto and desorb from grain surfaces, but chemical interactions were not implemented. More chemical species could be added first, chosen to better understand the C/O and C/N/O ratios evolving in space and time. Then, a small reaction network could be added. The model is computationally expensive to run, so careful consideration will be needed when deciding which species and reactions to include. The end result of these additions will be a simple disk model with growth, fragmentation, and chemistry. These effects are not independent: Ice coatings, for example, can determine which regions of the outer disk have effective grain sticking and thus can grow planetesimals to small sizes more easily; yet, as frozen-out molecules react on grain surfaces, they may desorb, reducing the amount of ice available.

6.2 Microchemical simulations

Many important reactions in protoplanetary disks, such as the formation of water and some organic molecules, occur on grain surfaces. The rate equations that are typically applied — even within this dissertation — assume large occupation numbers of atoms and molecules that are well-mixed, but this is often not a good description of reality for grain surfaces, since occupation can be low and atoms or molecules need to "hop" from site to site to find reaction partners. This is a significant

problem when trying to simulate the composition of a disk, and, by extension, planets. A better modeling approach is needed to accurately predict the abundances of important molecules like water, formaldehyde, methanol, and larger organics.

To address this problem, kinetic Monte Carlo (kMC) was introduced into astrochemistry (Chang et al., 2005; Cuppen et al., 2013; Garrod, 2013; Lamberts et al., 2013). This technique takes a random walk approach, simulating one event, such as a hop or reaction, at a time. The simulation must be done many times to infer an average overall behavior for the system. Probabilistic approaches, in contrast, simulate all possible events in a continuous way, such that every event that can occur over the system lifetime *will occur with some probability*. The end result is deterministic and reliable statistics.

Probabilistic microchemical simulations are extremely computationally challenging, however. Consider the following example: Suppose a chemical network contains nine chemical species existing on a square lattice of nine sites. Each site can be occupied by one atom or molecule from this network, or it can be empty. Thus, there are a total of ten possibilities for each lattice site. From probability theory, then, there are a total of 10^9 states for this lattice. The matrix that describes transitions between these possible states is therefore $10^9 \times 10^9$ in size. Assuming double-precision floating point numbers, storing this matrix would take approximately 1600 times more memory than is available on the current top supercomputer, Supercomputer Fugaku[1,2]. Thus, this small system is simply impossible to simulate naïvely on even the best current hardware.

Probabilistic techniques are used in quantum mechanics to simulate spin chains and in some chemical applications (e.g., Gelß et al., 2016). For a one-diemensional system, the "tensor train" approach can be faster than kMC, and many existing open-source tools, such as `scikit-tt`, can manipulate them. Tensor trains, however, are inherently one-dimensional, and extending them to two dimensions introduces a new set of problems: The two-dimensional analog of a tensor train, PEPS (projected entangled pair state), is known to be computationally inefficient. On the other

[1] `https://www.top500.org/lists/top500/2020/11/`

[2] `https://www.top500.org/system/179807/`

hand, newer techniques like MERA (multiscale entanglement renormalization ansatz, Vidal, 2008) were developed specifically for quantum mechanics and may or may not generalize to chemical systems easily.

By developing a framework for chemical modeling that uses probabilistic approaches rather than Monte Carlo, we may find better ways to capture the chemical dynamics of surface reactions without using random walk methods.

Bibliography

Abhyankar, S., Brown, J., Constantinescu, E., Ghosh, D., & Smith, B. F. 2014, PETSc/TS: A Modern Scalable DAE/ODE Solver Library, Preprint ANL/MCS-P5061-0114, Argonne National Laboratory

Abhyankar, S., Brown, J., Constantinescu, E. M., et al. 2018, arXiv e-prints, arXiv:1806.01437. https://arxiv.org/abs/1806.01437

Aikawa, Y., & Herbst, E. 1999, ApJ, 526, 314, doi: 10.1086/307973

Aikawa, Y., Miyama, S. M., Nakano, T., & Umebayashi, T. 1996, ApJ, 467, 684, doi: 10.1086/177644

Aikawa, Y., Umebayashi, T., Nakano, T., & Miyama, S. 1998, Faraday Discussions, 109, 281, doi: 10.1039/a800258d

Aikawa, Y., Umebayashi, T., Nakano, T., & Miyama, S. M. 1997, ApJ, 486, L51, doi: 10.1086/310837

—. 1999, ApJ, 519, 705, doi: 10.1086/307400

Altwegg, K., & Bockelée-Morvan, D. 2003, Space Sci. Rev., 106, 139, doi: 10.1023/A:1024685620462

Ambikasaran, S., Foreman-Mackey, D., Greengard, L., Hogg, D. W., & O'Neil, M. 2014, ArXiv e-prints. https://arxiv.org/abs/1403.6015

Amestoy, P. R., Buttari, A., L'Excellent, J.-Y., & Mary, T. 2019, ACM Trans. Math. Softw., 45, doi: 10.1145/3242094

Amestoy, P. R., Duff, I. S., Koster, J., & L'Excellent, J.-Y. 2001a, SIAM Journal on Matrix Analysis and Applications, 23, 15

Amestoy, P. R., Duff, I. S., L'Excellent, J.-Y., & Koster, J. 2001b, SIAM Journal on Matrix Analysis and Applications, 23, 15, doi: 10.1137/S0895479899358194

Amestoy, P. R., Guermouche, A., L'Excellent, J.-Y., & Pralet, S. 2006, Parallel Computing, 32, 136

Andrews, S. M. 2020, ARA&A, 58, 483, doi: 10.1146/annurev-astro-031220-010302

Andrews, S. M., Wilner, D. J., Hughes, A. M., et al. 2012, ApJ, 744, 162, doi: 10.1088/0004-637X/744/2/162

Armitage, P. J. 2010, Astrophysics of Planet Formation, 294

Asphaug, E., & Reufer, A. 2014, Nature Geoscience, 7, 564, doi: 10.1038/ngeo2189

Bacciotti, F., Girart, J. M., Padovani, M., et al. 2018, ApJ, 865, L12, doi: 10.3847/2041-8213/aadf87

Bai, X.-N., & Stone, J. M. 2010, ApJ, 722, 1437, doi: 10.1088/0004-637X/722/2/1437

Balay, S., Gropp, W. D., McInnes, L. C., & Smith, B. F. 1997, in Modern Software Tools in Scientific Computing, ed. E. Arge, A. M. Bruaset, & H. P. Langtangen (Birkhäuser Press), 163–202

Balay, S., Abhyankar, S., Adams, M. F., et al. 2018, PETSc Users Manual, Tech. Rep. ANL-95/11 - Revision 3.9, Argonne National Laboratory

—. 2019, PETSc Web page. https://www.mcs.anl.gov/petsc

Barclay, T., Pepper, J., & Quintana, E. V. 2018, ApJS, 239, 2, doi: 10.3847/1538-4365/aae3e9

Bauer, I., Finocchi, F., Duschl, W. J., Gail, H.-P., & Schloeder, J. P. 1997, A&A, 317, 273

Benz, W., Anic, A., Horner, J., & Whitby, J. A. 2008, The Origin of Mercury, ed. A. Balogh, L. Ksanfomality, & R. von Steiger (New York, NY: Springer New York), 7–20. https://doi.org/10.1007/978-0-387-77539-5_2

Bergin, E. A., Aikawa, Y., Blake, G. A., & van Dishoeck, E. F. 2007, Protostars and Planets V, 751

Birnstiel, T., Dullemond, C. P., & Brauer, F. 2010, A&A, 513, A79, doi: 10.1051/0004-6361/200913731

Birnstiel, T., Dullemond, C. P., Zhu, Z., et al. 2018, ApJ, 869, L45, doi: 10.3847/2041-8213/aaf743

Biver, N., Bockelée-Morvan, D., Paubert, G., et al. 2018, A&A, 619, A127, doi: 10.1051/0004-6361/201833449

Bockelée-Morvan, D., & Biver, N. 2017, Philosophical Transactions of the Royal Society of London Series A, 375, 20160252, doi: 10.1098/rsta.2016.0252

Bockelée-Morvan, D., Gautier, D., Hersant, F., Huré, J.-M., & Robert, F. 2002, A&A, 384, 1107, doi: 10.1051/0004-6361:20020086

Bodenheimer, P., & Pollack, J. B. 1986, Icarus, 67, 391, doi: 10.1016/0019-1035(86)90122-3

Bodewits, D., Noonan, J. W., Feldman, P. D., et al. 2020, Nature Astronomy, 4, 867, doi: 10.1038/s41550-020-1095-2

Boogert, A. C. A., Gerakines, P. A., & Whittet, D. C. B. 2015, ARA&A, 53, 541, doi: 10.1146/annurev-astro-082214-122348

Boss, A. P., Butler, R. P., Hubbard, W. B., et al. 2007, Transactions of the International Astronomical Union, Series A, 26A, 183, doi: 10.1017/S1743921306004509

Brauer, F., Dullemond, C. P., & Henning, T. 2008, A&A, 480, 859, doi: 10.1051/0004-6361:20077759

Carado, B., & Knuth, K. H. 2020, Astronomy and Computing, 32, 100406, doi: 10.1016/j.ascom.2020.100406

Carter, J. A., Yee, J. C., Eastman, J., Gaudi, B. S., & Winn, J. N. 2008, ApJ, 689, 499, doi: 10.1086/592321

Chambers, J. E. 2009, ApJ, 705, 1206, doi: 10.1088/0004-637X/705/2/1206

Chang, Q., Cuppen, H. M., & Herbst, E. 2005, A&A, 434, 599

Chau, A., Reinhardt, C., Helled, R., & Stadel, J. 2018, The Astrophysical Journal, 865, 35, doi: 10.3847/1538-4357/aad8b0

Chiang, E. I., & Goldreich, P. 1997, ApJ, 490, 368, doi: 10.1086/304869

Ciesla, F. J., & Sandford, S. A. 2012, Science, 336, 452, doi: 10.1126/science.1217291

Clarke, C., & Carswell, B. 2007, Principles of Astrophysical Fluid Dynamics

Clatterbuck, D., Chrzan, D., & Morris, J. 2003, Acta Materialia, 51, 2271 , doi: https://doi.org/10.1016/S1359-6454(03)00033-8

Cleeves, L. I., Bergin, E. A., & Adams, F. C. 2014a, ApJ, 794, 123, doi: 10.1088/0004-637X/794/2/123

Cleeves, L. I., Bergin, E. A., Alexander, C. M. O. ., et al. 2014b, Science, 345, 1590, doi: 10.1126/science.1258055

Cordiner, M. A., Milam, S. N., Biver, N., et al. 2020, Nature Astronomy, doi: 10.1038/s41550-020-1087-2

Cridland, A. J., Pudritz, R. E., & Alessi, M. 2016, MNRAS, 461, 3274, doi: 10.1093/mnras/stw1511

Cridland, A. J., Pudritz, R. E., & Birnstiel, T. 2017a, MNRAS, 465, 3865, doi: 10.1093/mnras/stw2946

Cridland, A. J., Pudritz, R. E., Birnstiel, T., Cleeves, L. I., & Bergin, E. A. 2017b, MNRAS, 469, 3910, doi: 10.1093/mnras/stx1069

Cuppen, H. M., Karssemeijer, L. J., & Lamberts, T. 2013, Chemical Reviews, 113, 8840

D'Alessio, P., Cantö, J., Calvet, N., & Lizano, S. 1998, ApJ, 500, 411, doi: 10.1086/305702

Dartois, E., Dutrey, A., & Guilloteau, S. 2003, A&A, 399, 773, doi: 10.1051/0004-6361:20021638

Davidsson, B. J. R. 1999, Icarus, 142, 525, doi: 10.1006/icar.1999.6214

de Pater, I., & Lissauer, J. J. 2010, Planetary Sciences

De Sanctis, M. C., Capria, M. T., & Coradini, A. 2001, AJ, 121, 2792, doi: 10.1086/320385

Désert, J.-M., Charbonneau, D., Torres, G., et al. 2015, ApJ, 804, 59, doi: 10.1088/0004-637X/804/1/59

Dressing, C. D., Charbonneau, D., Dumusque, X., et al. 2015, ApJ, 800, 135, doi: 10.1088/0004-637X/800/2/135

Dullemond, C. P., & Dominik, C. 2005, A&A, 434, 971, doi: 10.1051/0004-6361:20042080

Dullemond, C. P., Juhasz, A., Pohl, A., et al. 2012, RADMC-3D: A multi-purpose radiative transfer tool. http://ascl.net/1202.015

Eistrup, C., Walsh, C., & van Dishoeck, E. F. 2016, A&A, 595, A83, doi: 10.1051/0004-6361/201628509

—. 2019, A&A, 629, A84, doi: 10.1051/0004-6361/201935812

Feaga, L. M., A'Hearn, M. F., Farnham, T. L., et al. 2014, AJ, 147, 24, doi: 10.1088/0004-6256/147/1/24

Fitzsimmons, A., Hainaut, O., Meech, K. J., et al. 2019, ApJ, 885, L9, doi: 10.3847/2041-8213/ab49fc

Flaherty, K. M., Hughes, A. M., Teague, R., et al. 2018, ApJ, 856, 117, doi: 10.3847/1538-4357/aab615

Fogel, J. K. J., Bethell, T. J., Bergin, E. A., Calvet, N., & Semenov, D. 2011, ApJ, 726, 29, doi: 10.1088/0004-637X/726/1/29

Furlan, E., Watson, D. M., McClure, M. K., et al. 2009, ApJ, 703, 1964, doi: 10.1088/0004-637X/703/2/1964

Furuya, K., Aikawa, Y., Nomura, H., Hersant, F., & Wakelam, V. 2013, ApJ, 779, 11, doi: 10.1088/0004-637X/779/1/11

Galassi, M., Davies, J., Theiler, J., et al. 2009, GNU Scientific Library Reference Manual, 3rd edn.

Garrod, R. T. 2013, ApJ, 778, 158

Gelß, P., Matera, S., & Schütte, C. 2016, Journal of Computational Physics, 314, 489 , doi: https://doi.org/10.1016/j.jcp.2016.03.025

Gladman, B., & Coffey, J. 2009, Meteoritics and Planetary Science, 44, 285, doi: 10.1111/j.1945-5100.2009.tb00734.x

Guenther, E. W., Barragán, O., Dai, F., et al. 2017, A&A, 608, A93, doi: 10.1051/0004-6361/201730885

Gullbring, E., Hartmann, L., Briceño, C., & Calvet, N. 1998, ApJ, 492, 323, doi: 10.1086/305032

Gundlach, B., & Blum, J. 2015, ApJ, 798, 34, doi: 10.1088/0004-637X/798/1/34

Hachisu, I. 1986a, ApJS, 61, 479, doi: 10.1086/191121

—. 1986b, ApJS, 62, 461, doi: 10.1086/191148

Handy, M., Wissing, S., & Streit, L. 1999, Tectonophysics, 303, 175 , doi: https://doi.org/10.1016/S0040-1951(98)00251-0

Hanner, M. S. 1999, Space Sci. Rev., 90, 99, doi: 10.1023/A:1005285711945

Hartmann, L. 2009, Accretion Processes in Star Formation: Second Edition

Hauck, S. A., Margot, J.-L., Solomon, S. C., et al. 2013, Journal of Geophysical Research (Planets), 118, 1204, doi: 10.1002/jgre.20091

Heinzeller, D., Nomura, H., Walsh, C., & Millar, T. J. 2011, ApJ, 731, 115, doi: 10.1088/0004-637X/731/2/115

Henning, T., & Semenov, D. 2013, Chemical Reviews, 113, 9016, doi: 10.1021/cr400128p

Hindmarsh, A. C., Brown, P. N., Grant, K. E., et al. 2005, ACM Transactions on Mathematical Software (TOMS), 31, 363

Hollenbach, D., Kaufman, M. J., Bergin, E. A., & Melnick, G. J. 2009, ApJ, 690, 1497, doi: 10.1088/0004-637X/690/2/1497

Holsapple, K. A., & Michel, P. 2006, Icarus, 183, 331, doi: 10.1016/j.icarus.2006.03.013

Hora, J. L., Carey, S., Surace, J., et al. 2008, PASP, 120, 1233, doi: 10.1086/593217

Huang, J., Andrews, S. M., Pérez, L. M., et al. 2018, ApJ, 869, L43, doi: 10.3847/2041-8213/aaf7a0

Hughes, A. M., Wilner, D. J., Andrews, S. M., Qi, C., & Hogerheijde, M. R. 2011, ApJ, 727, 85, doi: 10.1088/0004-637X/727/2/85

Indebetouw, R., Mathis, J. S., Babler, B. L., et al. 2005, ApJ, 619, 931, doi: 10.1086/426679

Jackson, I. 1998, Geophys. J. Int., 134, 291, doi: 10.1046/j.1365-246x.1998.00560.x

Jia, S., & Spruit, H. C. 2017, MNRAS, 465, 149, doi: 10.1093/mnras/stw1693

Johansen, A., Blum, J., Tanaka, H., et al. 2014, in Protostars and Planets VI, ed. H. Beuther, R. S. Klessen, C. P. Dullemond, & T. Henning, 547

Johansen, A., Klahr, H., & Henning, T. 2006, ApJ, 636, 1121, doi: 10.1086/498078

Jones, E., Oliphant, T., Peterson, P., et al. 2001–, SciPy: Open source scientific tools for Python. http://www.scipy.org/

Kama, M., Bruderer, S., van Dishoeck, E. F., et al. 2016, A&A, 592, A83, doi: 10.1051/0004-6361/201526991

Kite, E. S., Fegley, Jr., B., Schaefer, L., & Gaidos, E. 2016, ApJ, 828, 80, doi: 10.3847/0004-637X/828/2/80

Kokubo, E., & Ida, S. 2012, Progress of Theoretical and Experimental Physics, 2012, 01A308, doi: 10.1093/ptep/pts032

Lamberts, T., Cuppen, H. M., Ioppolo, S., & Linnartz, H. 2013, Physical Chemistry Chemical Physics (Incorporating Faraday Transactions), 15, 8287

Leconte, J., Lai, D., & Chabrier, G. 2011, A&A, 528, A41, doi: 10.1051/0004-6361/201015811

Lee, E. J., & Chiang, E. 2017, ApJ, 842, 40, doi: 10.3847/1538-4357/aa6fb3

Léger, A., Grasset, O., Fegley, B., et al. 2011, Icarus, 213, 1, doi: 10.1016/j.icarus.2011.02.004

Lewis, J. S. 1972, Earth and Planetary Science Letters, 15, 286, doi: 10.1016/0012-821X(72)90174-4

Lineweaver, C. H., & Robles, J. A. 2009, in Astronomical Society of the Pacific Conference Series, Vol. 420, Bioastronomy 2007: Molecules, Microbes and Extraterrestrial Life, ed. K. J. Meech, J. V. Keane, M. J. Mumma, J. L. Siefert, & D. J. Werthimer, 83

Lynden-Bell, D., & Pringle, J. E. 1974, MNRAS, 168, 603, doi: 10.1093/mnras/168.3.603

Mamajek, E. E. 2009, in American Institute of Physics Conference Series, Vol. 1158, American Institute of Physics Conference Series, ed. T. Usuda, M. Tamura, & M. Ishii, 3–10

Mandel, K., & Agol, E. 2002, ApJ, 580, L171, doi: 10.1086/345520

Marcus, R. A., Sasselov, D., Hernquist, L., & Stewart, S. T. 2010, ApJ, 712, L73, doi: 10.1088/2041-8205/712/1/L73

McGuire, B. A. 2018, ApJS, 239, 17, doi: 10.3847/1538-4365/aae5d2

McKay, A. J., DiSanti, M. A., Kelley, M. S. P., et al. 2019, AJ, 158, 128, doi: 10.3847/1538-3881/ab32e4

Meijerink, R., Pontoppidan, K. M., Blake, G. A., Poelman, D. R., & Dullemond, C. P. 2009, ApJ, 704, 1471, doi: 10.1088/0004-637X/704/2/1471

Millholland, S. C., & Spalding, C. 2020, ApJ, 905, 71, doi: 10.3847/1538-4357/abc4e5

Mizuno, H. 1980, Progress of Theoretical Physics, 64, 544, doi: 10.1143/PTP.64.544

Morbidelli, A., & Raymond, S. N. 2016, Journal of Geophysical Research (Planets), 121, 1962, doi: 10.1002/2016JE005088

Morfill, G. E. 1983, Icarus, 53, 41, doi: 10.1016/0019-1035(83)90019-2

Morton, T. D. 2015, isochrones: Stellar model grid package, Astrophysics Source Code Library. http://ascl.net/1503.010

Mousis, O., Aguichine, A., Bouquet, A., et al. 2021, arXiv e-prints, arXiv:2103.01793. https://arxiv.org/abs/2103.01793

Mumma, M. J., & Charnley, S. B. 2011, ARA&A, 49, 471, doi: 10.1146/annurev-astro-081309-130811

Noack, L., Godolt, M., von Paris, P., et al. 2014, Planet. Space Sci., 98, 14, doi: 10.1016/j.pss.2014.01.003

Nomura, H., Aikawa, Y., Nakagawa, Y., & Millar, T. J. 2009, A&A, 495, 183, doi: 10.1051/0004-6361:200810206

Nomura, H., Aikawa, Y., Tsujimoto, M., Nakagawa, Y., & Millar, T. J. 2007, ApJ, 661, 334, doi: 10.1086/513419

Öberg, K. I. 2016, Chemical Reviews, 116, 9631, doi: 10.1021/acs.chemrev.5b00694

Öberg, K. I., & Bergin, E. A. 2016, ApJ, 831, L19, doi: 10.3847/2041-8205/831/2/L19

Öberg, K. I., Guzmán, V. V., Furuya, K., et al. 2015, Nature, 520, 198, doi: 10.1038/nature14276

Öberg, K. I., Murray-Clay, R., & Bergin, E. A. 2011, ApJ, 743, L16, doi: 10.1088/2041-8205/743/1/L16

Parker, S. G., Bigler, J., Dietrich, A., et al. 2010, ACM Trans. Graph., 29, doi: 10.1145/1778765.1778803

Perez-Becker, D., & Chiang, E. 2013, MNRAS, 433, 2294, doi: 10.1093/mnras/stt895

Petrovich, C., Deibert, E., & Wu, Y. 2019, AJ, 157, 180, doi: 10.3847/1538-3881/ab0e0a

Piro, A. L., & Vissapragada, S. 2020, AJ, 159, 131, doi: 10.3847/1538-3881/ab7192

Piso, A.-M. A., Öberg, K. I., Birnstiel, T., & Murray-Clay, R. A. 2015, ApJ, 815, 109, doi: 10.1088/0004-637X/815/2/109

Pontoppidan, K. M., Salyk, C., Bergin, E. A., et al. 2014, Protostars and Planets VI, 363, doi: 10.2458/azu_uapress_9780816531240-ch016

Press, W. H., Flannery, B. P., Teukolsky, S. A., & Vetterling, W. T. 1988, Numerical Recipes in C: The Art of Scientific Computing (Cambridge University Press)

Price, E. M., Cleeves, L. I., & Öberg, K. I. 2020, ApJ, 890, 154, doi: 10.3847/1538-4357/ab5fd4

Price, E. M., & Rogers, L. A. 2020, ApJ, 894, 8, doi: 10.3847/1538-4357/ab7c67

Pringle, J. E. 1981, ARA&A, 19, 137, doi: 10.1146/annurev.aa.19.090181.001033

Rab, C., Baldovin-Saavedra, C., Dionatos, O., Vorobyov, E., & Güdel, M. 2016, Space Sci. Rev., 205, 3, doi: 10.1007/s11214-016-0325-5

Rappaport, S., Sanchis-Ojeda, R., Rogers, L. A., Levine, A., & Winn, J. N. 2013, ApJ, 773, L15, doi: 10.1088/2041-8205/773/1/L15

Rappaport, S., Levine, A., Chiang, E., et al. 2012, ApJ, 752, 1, doi: 10.1088/0004-637X/752/1/1

Roatsch, T., Jaumann, R., Stephan, K., & Thomas, P. C. 2009, Cartographic Mapping of the Icy Satellites Using ISS and VIMS Data, ed. M. K. Dougherty, L. W. Esposito, & S. M. Krimigis (Dordrecht: Springer Netherlands), 763–781. https://doi.org/10.1007/978-1-4020-9217-6_24

Roche, É. 1849, in Académie des Sciences Montpellier: Mémoires la Section des Sciences, Vol. 1, 243–262

Ros, K., & Johansen, A. 2013, A&A, 552, A137, doi: 10.1051/0004-6361/201220536

Sanchis-Ojeda, R., Rappaport, S., Winn, J. N., et al. 2014, ApJ, 787, 47, doi: 10.1088/0004-637X/787/1/47

Santerne, A., Brugger, B., Armstrong, D. J., et al. 2018, Nature Astronomy, 2, 393, doi: 10.1038/s41550-018-0420-5

Saxena, P., Panka, P., & Summers, M. 2015, MNRAS, 446, 4271, doi: 10.1093/mnras/stu2111

Seager, S., Kuchner, M., Hier-Majumder, C. A., & Militzer, B. 2007, ApJ, 669, 1279, doi: 10.1086/521346

Semenov, D., & Wiebe, D. 2011, ApJS, 196, 25, doi: 10.1088/0067-0049/196/2/25

Semenov, D., Wiebe, D., & Henning, T. 2006, ApJ, 647, L57, doi: 10.1086/507096

Semenov, D., Hersant, F., Wakelam, V., et al. 2010, A&A, 522, A42, doi: 10.1051/0004-6361/201015149

Shakura, N. I., & Sunyaev, R. A. 1973, A&A, 24, 337

Siess, L., Dufour, E., & Forestini, M. 2000, A&A, 358, 593

Siess, L., Forestini, M., & Dougados, C. 1997, A&A, 324, 556

Simon, J. B., Bai, X.-N., Flaherty, K. M., & Hughes, A. M. 2018, ApJ, 865, 10, doi: 10.3847/1538-4357/aad86d

Smith, A. M. S., Cabrera, J., Csizmadia, S., et al. 2018, MNRAS, 474, 5523, doi: 10.1093/mnras/stx2891

Smoluchowski, M. V. 1916, Zeitschrift fur Physik, 17, 557

Sotin, C., Grasset, O., & Mocquet, A. 2007, Icarus, 191, 337, doi: 10.1016/j.icarus.2007.04.006

Strøm, P. A., Bodewits, D., Knight, M. M., et al. 2020, arXiv e-prints, arXiv:2007.09155. https://arxiv.org/abs/2007.09155

Takahashi, E. 1986, J. Geophys. Res., 91, 9367, doi: 10.1029/JB091iB09p09367

Tanaka, T. 2011, MNRAS, 410, 1007, doi: 10.1111/j.1365-2966.2010.17496.x

Teague, R., Guilloteau, S., Semenov, D., et al. 2016, A&A, 592, A49, doi: 10.1051/0004-6361/201628550

Testi, L., Birnstiel, T., Ricci, L., et al. 2014, in Protostars and Planets VI, ed. H. Beuther, R. S. Klessen, C. P. Dullemond, & T. Henning, 339

Thomas, P. C. 2010, Icarus, 208, 395, doi: 10.1016/j.icarus.2010.01.025

Thomas, P. C., Parker, J. W., McFadden, L. A., et al. 2005, Nature, 437, 224, doi: 10.1038/nature03938

van Dishoeck, E. F., & Blake, G. A. 1998, ARA&A, 36, 317, doi: 10.1146/annurev.astro.36.1.317

Vidal, G. 2008, Phys. Rev. Lett., 101, 110501

Wagner, K., Follete, K. B., Close, L. M., et al. 2018, ApJ, 863, L8, doi: 10.3847/2041-8213/aad695

Wang, L., & Dai, F. 2019, ApJ, 873, L1, doi: 10.3847/2041-8213/ab0653

Weidenschilling, S. J. 1977, MNRAS, 180, 57, doi: 10.1093/mnras/180.1.57

Weidenschilling, S. J., & Cuzzi, J. N. 1993, in Protostars and Planets III, ed. E. H. Levy & J. I. Lunine, 1031–1060

Whipple, F. L. 1973, NASA Special Publication, 319, 355

Willacy, K., Langer, W., Allen, M., & Bryden, G. 2006, ApJ, 644, 1202, doi: 10.1086/503702

Willacy, K., & Langer, W. D. 2000, ApJ, 544, 903, doi: 10.1086/317236

Winn, J. N., Sanchis-Ojeda, R., & Rappaport, S. 2018, New A Rev., 83, 37, doi: 10.1016/j.newar.2019.03.006

Wood, B. J., Walter, M. J., & Wade, J. 2006, Nature, 441, 825, doi: 10.1038/nature04763

Wurm, G., Trieloff, M., & Rauer, H. 2013, ApJ, 769, 78, doi: 10.1088/0004-637X/769/1/78

Xing, Z., Bodewits, D., Noonan, J., & Bannister, M. T. 2020, ApJ, 893, L48, doi: 10.3847/2041-8213/ab86be